Dissertation

submitted to the

Combined Faculties for Natural Sciences and for Mathematics

of the Ruperto-Carola University of Heidelberg, Germany

for the degree of

Doctor of Natural Sciences

presented by

Dipl.–Phys. Martin Krause

born in Mannheim, Germany

Oral examination: 15th of May, 2002

On the Interaction of Jets with the Dense Medium of the Early Universe

Referees: Prof. Dr. Max Camenzind

Prof. Dr. Klaus Meisenheimer

Zusammenfassung

Radiogalaxien wurden in den letzen Jahren bei Rotverschiebungen von über fünf entdeckt. Sie unterscheiden sich durch höhere Radioleistung und Emissionsliniencharakteristik von näheren Quellen. Zum Verständnis dieser gasreichen Zentren von Protogalaxienhaufen wurden hydrodynamische Jets mit Kühlung simuliert. Nachdem der dreidimensionale Code Nirvana hierfür getestet und nach Vergleich mit Referenzsimulationen als geeignet befunden wurde, wurde eine adiabatische 2D Parameterstudie im relevanten Bereich (Dichtekontrast Jet/Medium $\eta = 10^{-2} - 10^{-5}$) durchgeführt. Dabei wurde eine charackteristische Form und Verbreiterung des Cocoons gefunden. Die radiale Bugschockausbreitung kann durch eine sphärische Druckwelle mit konstanter Energiezufuhr analytisch approximiert werden. Die Simulation mit Nichtgleichgewichtskühlung zeigte eine Abkühlung des Bugschocks innerhalb der Propagationszeit auf $\approx 10^4$ K bei äußerer Gasdichte von $\approx 1\,\mathrm{cm}^{-3}$. Der Bugschock bildete nach einer ersten globalen Kühl- und Komprimierungssphase ein großskaliges Absorptionssystem, das dann fragmentiert und Sterne in typischerweise 10^4 Kugelsternhaufen zu je $10^6 M_\odot$ bilden könnte. Filamentierung und Fragmentation wurden bei hoher Auflösung bestätigt. Absorber in fernen Radiogalaxien sowie Kugelsternhaufenexzesse in nahen zentralen Haufengalaxien kann man so erklären. Mit Literaturparametern für Cygnus A wurde eine 3D Simulation, erstmals mit Gegenjet, durchgeführt. Der Bugschock zeigte dabei zwei deutlich getrennte Phasen, die auch in der Beobachtung erkennbar sind. Basisparameter des Jets wurden bestimmt. In der Simulation zeigten sich außerdem charakteristische Röntgenstrukturen (Ringe), die in zwei Quellen (M87) identifiziert und interpretiert wurden.

Abstract

In recent years, radio galaxies have been found at redshifts above five. They differ in higher radio power and emission line characteristics from sources nearby. To understand these centers of proto-galaxy-clusters, hydrodynamic jets with cooling were simulated. After validation of the 3D code NIRVANA by comparison with literature simulations, an adiabatic 2D parameter study in the relevant regime (density contrast jet/medium $\eta = 10^{-2} - 10^{-5}$) was performed. Characteristic cocoon shape and broadenings were found. The radial expansion can be analytically approximated by a spherical blast wave with constant energy injection. In a non-equilibrium simulation the bow shock cooled to 10^4 K during jet propagation time (external density $1\,\mathrm{cm}^{-3}$). After global cooling and compression, the bow shock turned into a big absorber which fragmented, and should form stars in typically 10^4 globular clusters of $10^6 M_\odot$. Filamentation and fragmentation was confirmed at high resolution. Absorbers in far-off radio galaxies and globular cluster excesses in nearby CD galaxies can be explained that way. With literature parameters fo Cygnus A, a 3D simulation, for the first time with counter-jet, was performed. The bow shock shows two clearly separated phases, also evident in observation. Basic jet parameters have been derived. The simulation shows characteristic X-ray features (rings) which were identified and interpreted in two sources (M87).

The heavens are telling of the glory of God;
And their expanse is declaring the work of His hands.
Day to day pours forth speech,
And night to night reveals knowledge.
There is no speech, nor are there words;
Their voice is not heard.

Psalm 19

Contents

Chapter I

Introduction

I.1 Extragalactic Radio Sources

During the last fifty years, radio sources were identified with line emitting objects of ever higher redshift. When Baade and Minkowski (1954) established the redshift of 0.06 for the first time for a radio galaxy (Cygnus A), the main problem for them was optical astrometry. This problem solved, many identifications could be made up to a redshift of about one. In the 1980s it was noticed that the spectral energy distribution of the radio emission steepens with frequency, which gives steeper spectral indices at higher redshift, and that the K-Band infrared luminosity is very well correlated to the redshift. Selecting sources according to these properties caused a considerable jump of the redshift record, with the current record holder TN J0924-2201 at redshift 5.19 (van Breugel et al., 1999) also selected by this method.

I.1.1 Basic properties of radio galaxies

Contemplating the radio image of Cygnus A (Fig. I.1), one notices the basic features of radio galaxies sketched in Fig. I.2:

- central core: Usually, the component with the flattest radio spectrum. Here resides the active galactic nucleus (AGN). A black hole of millions to a few billions of solar masses is fed here by an accretion disk, accelerating and collimating a wind to velocities close to the speed of light and narrow opening angles: the jet.
- jet beams: A thin beam, sometimes invisible, extending from the core to the hotspots.
- hotspots: One (sometimes more) bright spot on each side of the core. Here the jet terminates in a prominent shock, called Mach disk. The velocity drops from supersonic to subsonic.

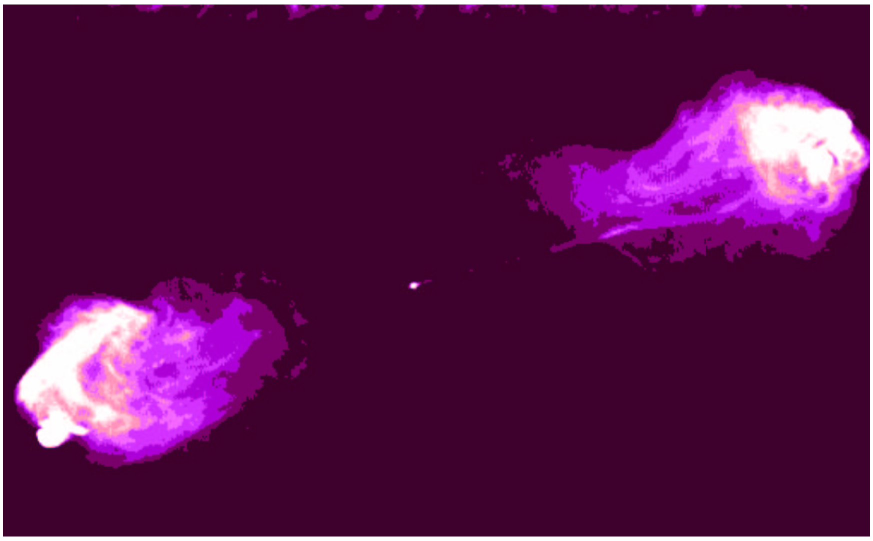

Figure I.1: *Radio image of Cygnus A at 5 GHz with 0.4" resolution. (VLA, credit: NRAO)*

- lobes: Large areas around the hotspot, more pronounced on lower frequency images, where they can be traced down to the core (Carilli et al., 1991). This is material which passed through the Mach disk. It flows backwards at slower pace than the jet speed. Lobes are often filamentary, have polarisations of more than 40 % and magnetic fields parallel to the well–defined edge of the lobe, at which the intensity rapidly goes to zero.

Only recently, with the launching of the Chandra satellite, detailed views in the X-ray band became available (Fig. I.3). On that picture one can see for the

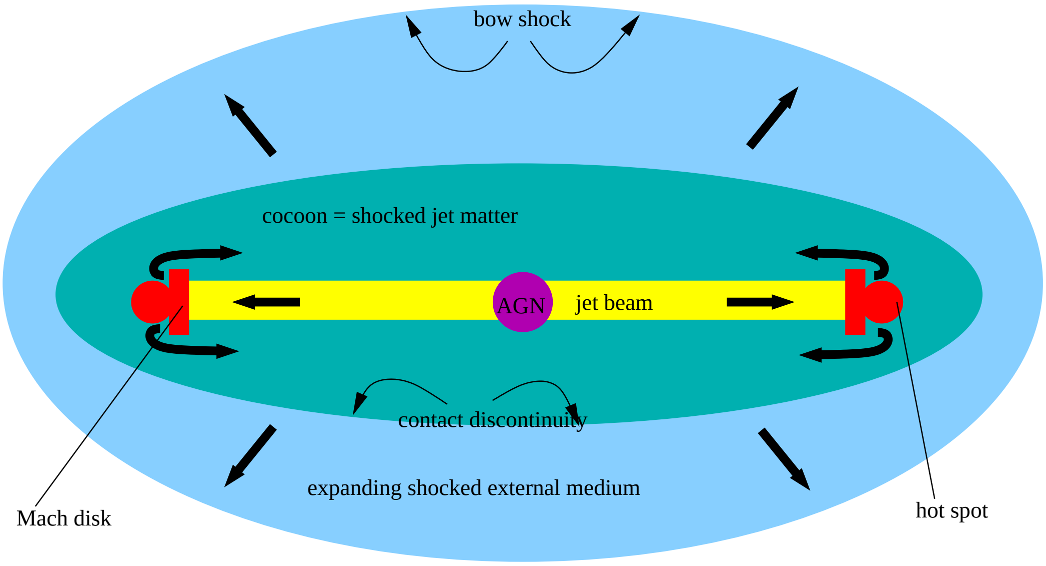

Figure I.2: *Sketch of the basic constituents of radio galaxies.*

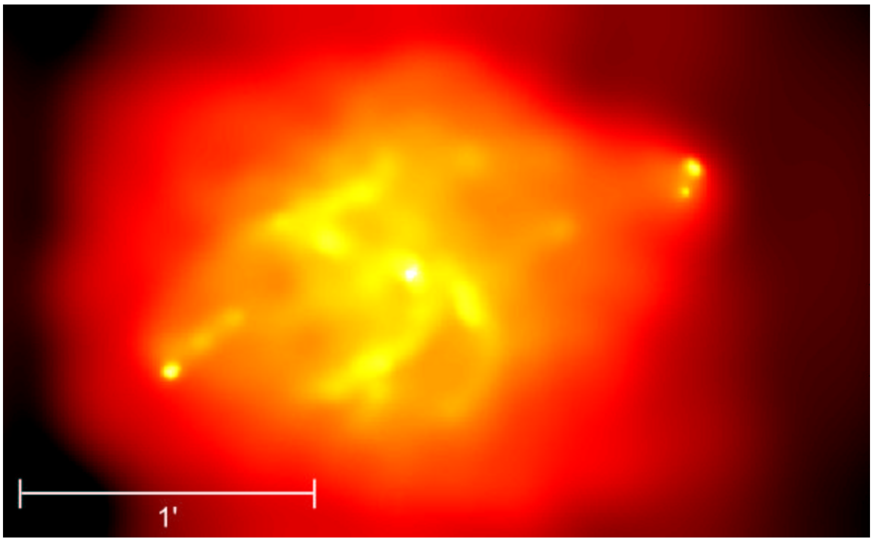

Figure I.3: *X-ray image of Cygnus A (Chandra, credit: Chandra Homepage)*

first time a clear signature of the bow shock. It consists of displaced cluster gas heated to a temperature of 70 mio K (Smith et al., 2002). Eventually, the Mach number of this shock will decrease to one, turning into a sonic disturbance. The bow shock encloses the radio jet.

Objects with one or more of the above properties are classified as Double Radio source Associated with Galactic Nucleus (DRAGN) by Leahy (1993) (see also Leahy, 2000). He also gives more detailed and operational definitions of the phenomenon. However, the definition is not used widely in the astrophysical community. Therefore, the term radio galaxy will be used mainly, in the following. A widely accepted distinction among radio galaxies was introduced by Fanaroff and Riley (1974). They divided radio galaxies with two clearly separated hotspots into two classes:

I The separation between the points of peak intensity in the two lobes is smaller than half the largest size of the source.

II The separation between the points of peak intensity in the two lobes is greater than half the largest size of the source.

Fanaroff and Riley (1974) found that nearly all the FR I sources had a luminosity less then 2×10^{32} erg s^{-1} Hz^{-1} sr^{-1} at 178 MHz and with a Hubble constant of 50 km Mpc^{-1} sec^{-1}, and that the FR II sources were brighter than that. The break may be a function of the optical luminosity of the host galaxy (Owen and White, 1991), which are bright elliptical galaxies. Apart from that, the transition is remarkably sharp. FR I sources are morphologically richer than the FR IIs, and there exist numerous subclassifications (Leahy, 2000). 3C386, 3C84, and 3C338 are representatives of the *relaxed doubles*, which earned their name from the lack of compact features in the haloes. The different jet morphologies

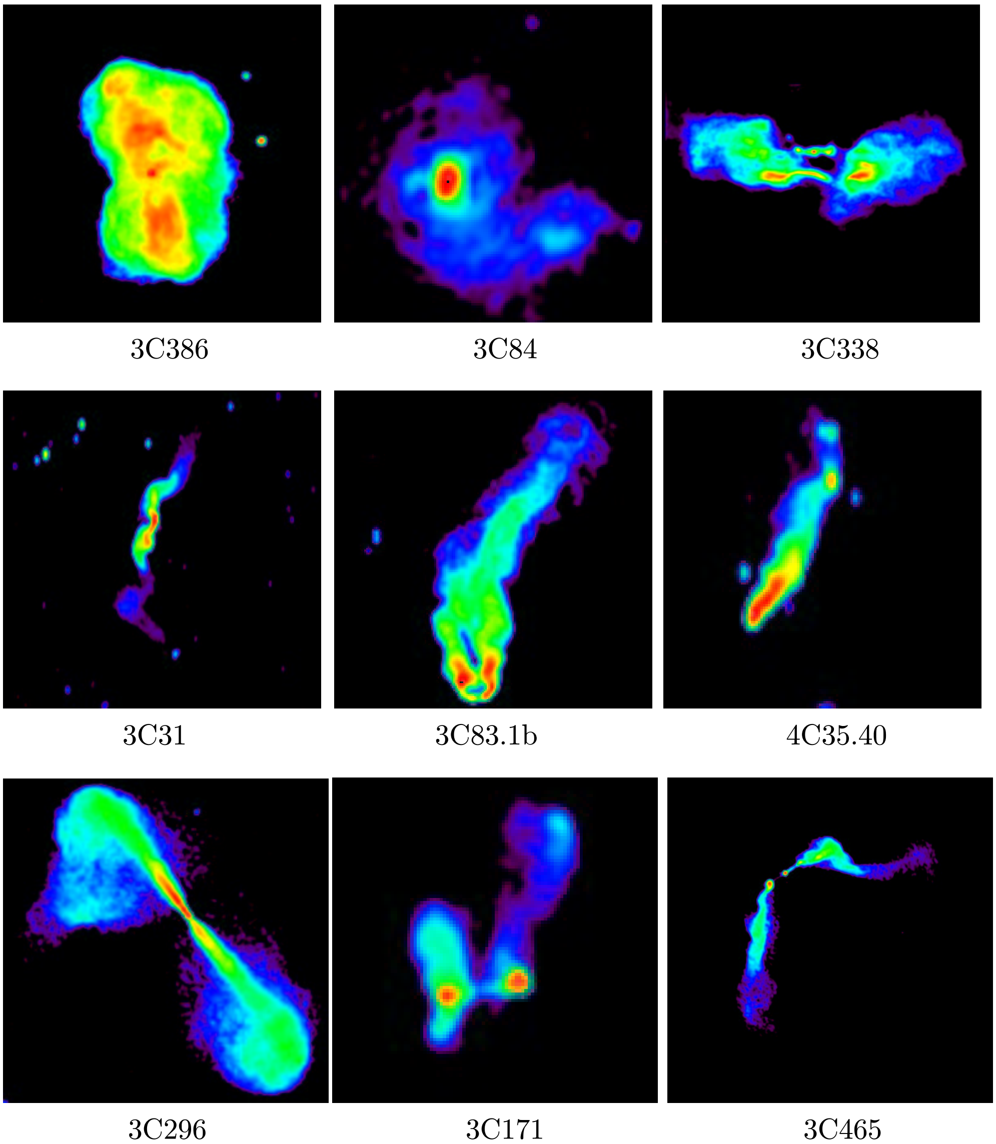

Figure I.4: *Several radio morphologies for FR I sources from Leahy (2000).*

are often believed to arise by interaction with the external medium. 3C84 is the center of the Perseus cluster of galaxies. The *peculiar* relaxed double 3C338 is the first ranked member in the Abell 2199 cluster. 3C31, 3C83.1b, 4C35.40, and 3C465 are *tailed twin jets*. 3C83.1b is a *narrow angle tail* source. It is believed that the morphology arises from movement through a cluster atmosphere perpendicular to the jet direction. The *head tail* jet in 4C35.40 is thought to be produced by a movement in jet direction. As usual for *wide angle tail* sources, 3C465 is the central member of its cluster Abell 2634. The jet bending is in the case of this class thought to arise from winds associated with mergers from clusters of galaxies. The isolated radio galaxy 3C296 represents the *bridged twin jet* class The bridges are the broad features in the place where you would expect narrow beams in a *classical double*, like Cygnus A. 3C171 is called a *plumed double* because of the fuzzy extensions. Such sources are sometimes classified as wide angle tail. Most FR II sources are classical doubles.

I.1.2 Radio galaxies at high redshift

The term *high redshift radio galaxy (HZRG)* was used, historically, for the highest known redshift sources. By now, it mostly refers to sources with redshift in excess of two (Carilli et al., 2001; van Ojik et al., 1997). In the following the same terminology will be used. For clarity, sources with a redshift upto 0.1 will be labeled *low*, and the remaining ones *intermediate* redshift sources. HZRG have been reviewed by McCarthy (1993). But since then, important progress has been made. A more recent comprehensive description can be found in Carilli et al. (2001). More than 150 radio galaxies are now detected at high redshift, half of them within the last three to four years (Carilli et al., 2001). Their redshift corresponds to a cosmological lookback–time of at least 80% the age of the Universe. This observed redshift range also corresponds to the maximum in the redshift distribution of quasars. The spatial density of these objects was at that time about 300 times higher than today.

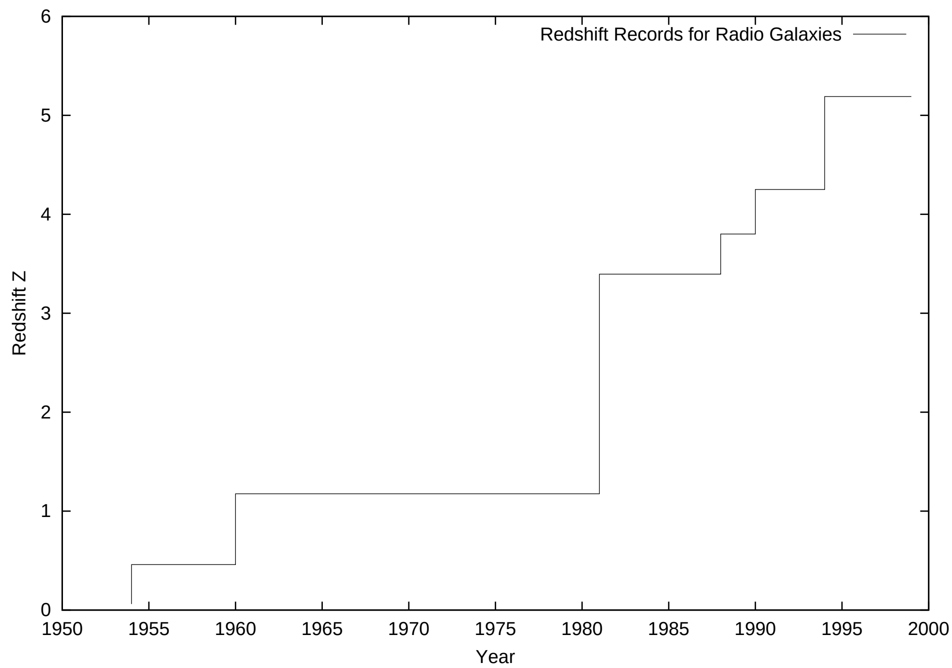

Figure I.5: *Some redshift records during the last fifty years. References: (Baade and Minkowski, 1954; Minkowski, 1960; Spinrad et al., 1981; Lilly, 1988; Chambers et al., 1990; Lacy et al., 1994; van Breugel et al., 1999)*

Spectral Characteristics

Radio galaxies and radio loud quasars, which are thought to be very similar to radio galaxies but seen at smaller viewing angles, with their jets, in general, show four distinct components in their spectrum:

- the infrared–optical–UV continuum of the central source (emission from the accretion disk and its surroundings);
- the radio–optical continuum of the jets (synchrotron emission from relativistic particles in the jet);
- the X–ray and γ continuum (inverse Compton emission from the inner jets);
- narrow and broad emission lines from heated gas.

While these features are shared by all radio galaxies to some extent, certain characteristics show up only at a specific redshift:

Size and power

The radio jets themselves show a characteristic length of 100 kpc only at low redshift. HZRG radio jets are typically much shorter ($\approx$ 10 kpc), and less regularly structured. This could possibly be due to a denser environment, where the jet is slower. Alternatively, the HZRG jets could be in a comparatively young state (Blundell and Rawlings, 1999). High redshift radio galaxies are more powerful than their low redshift counterparts. While the only powerful nearby radio galaxy (redshift $z = 0.0562$, radio power at 178 MHz $P_{178} = 6\ 10^{35}$ erg/sec/Hz) is Cygnus A (Carilli and Barthel, 1996), beyond $z \approx 2$ sources with $P_{178} > 10^{36}$ erg/sec/Hz have been found (Carilli et al., 2001). Assuming a typical spectrum and (unknown) conversion factor of total kinetic jet power to radio power of 10 %, this leads to total kinetic powers of $\approx 10^{46-47}$ erg/s for the most powerful sources. Typical extended radio sources in the local universe are one to two orders of magnitude fainter.

Host galaxies

Radio galaxies are hosted by massive ellipticals. At $z > 1$ they are even two magnitudes brighter in the K band than the brightest non-active galaxies. There is some evidence for a continuous transition, indicating that brighter galaxies host more powerful radio sources (De Breuck et al., 2002). The radio galaxy hosts seem to evolve with redshift (Pentericci et al., 2001): Beyond $z = 2.5$ HZRG show considerable substructure and clumpiness, indicating interactions and mergers. At $z \approx 2$ they appear morphologically relaxed, and down to $z \approx 1$ the galaxies approximately double in size. This could indicate that in this redshift range, a large fraction of the stars is produced, and that HZRG are more gas rich than lower redshift radio galaxies.

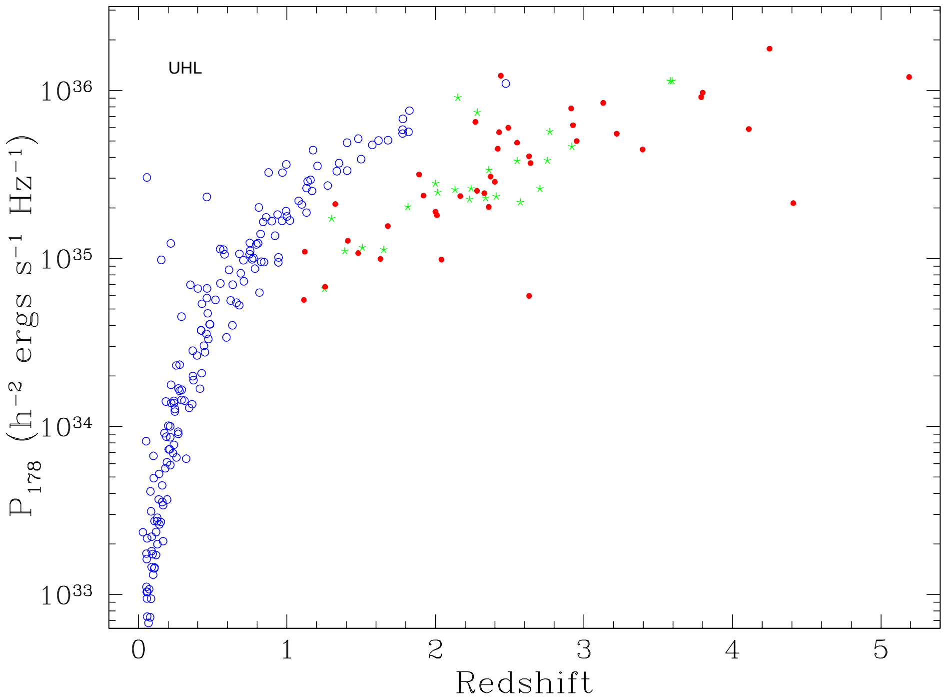

Figure I.6: *Radio power at a rest-frame frequency of 178 MHz versus redshift for the 3C sample (open circles) and fainter samples from the Leiden group (filled circles and stars), adopted from Carilli et al. (2001).*

Emission line lobes

Radio galaxies, in general, show emission line lobes (ELL). The dominant species are usually hydrogen, oxygen, carbon, neon and helium (McCarthy, 1993). High metalicities are observed upto high redshifts (Villar-Martín et al., 2001). Many radio galaxies show line ratios consistent with ionisation by a hidden central AGN. However, there are some peculiar examples, where it is likely, that the lines are excited by the impact of a bow shock on a dense background medium. According to Meisenheimer and Hippelein (1992), in the intermediate redshift radio galaxy 3C368 ($z = 1.13$) the bow shock heats the ambient medium to $\approx 10^7$ K. Subsequently, the gas cools down to ≈ 20000 K, where it can be seen in forbidden OII line emission. These ELLs are nicely placed around the radio jet, one side blue, the other redshifted, and lag behind the leading radio feature by about 11 (20) kpc, interpreted as the cooling length. There are also cases, where both processes significantly contribute (e.g. PKS 2250-41 ($z = 0.308$), Villar-Martín et al., 1999). Where ionisation by a bow shock is important, this indicates high densities ($n \approx 0.1$ cm^{-3}, 3C368).

HZRGs show huge halos of Lyman α emitting gas (van Ojik et al., 1996; Röttgering et al., 1996). These halos are much bigger than their low redshift counterparts, extending usually about the same size, or even further out, as the radio source, with up to $10^9\,M_\odot$. Small radio galaxies (< 50 kpc) show Lyman

α self absorption (van Ojik et al., 1997; De Breuck et al., 2000), preferentially on the blue wing of the emission line. Associated absorption is also present in small (< 50 kpc) radio quasars (Baker, 1999, 2001). Some authors have claimed to see more absorption in high redshift quasars (Ganguly et al., 2001), while others cannot find any redshift dependence (Baker et al., 2001). The discovery of associated absorption means that large amounts of neutral gas have to be present on scales of upto 50 kpc, covering all of the radio source, in almost every small radio loud AGN with a redshift greater than two. Two models have been proposed to explain the observed emission line properties. The first idea was that the the whole region around the radio source is filled with solar system sized clumps (temperature T $\approx 10^4$ K, number density n $\approx$ 100 cm^{-3}), residing in a hot (T $\approx 10^7$ K, n $\approx$ 0.1 cm^{-3}) intra-cluster medium. These clumps would emit lines, when they are illuminated by UV light from a hidden quasar, and produce absorption lines when outside the cone of light. The other model was put forward by Binette et al. (2000). According to their calculations with the photoionisation code MAPPINGS Ic, the absorbing gas is spatially separated and physically distinct from the emission line gas, with very low metalicity (Z $\approx 0.01 Z_\odot$) and density (n $\approx 10^{-3}$cm^{-3}).

Also, the total mass of the emission line gas grows strongly with redshift (Baum and McCarthy, 2000), ranging from $\approx 10^6 M_\odot$ nearby upto $\approx 10^{10} M_\odot$ at $z \approx 2$. If the kinematics of this gas is dominated by gravitational motions in the majority of cases, as claimed by Baum and McCarthy (2000), than the total (dynamical) mass, including dark matter, would correlate with the gas mass reaching $\approx 10^{14}\,M_\odot$ at $z = 2$. However, many authors take up the position that the velocities of $\approx$ 1000 km/s in extended emission line regions are probably not of gravitational origin (Solórzano-Iñarrea et al., 2001), but rather accelerated by interactions with the radio jet (Sutherland et al., 1993; Villar-Martín et al., 1999).

Alignment effect(s)

In HZRG, the optical continuum is often aligned with the radio emission (Chambers et al., 1987; McCarthy, 1993). Polarisation measurements have shown that this emission is highly polarised below $z = 1.5$ (Carilli et al., 2001). At $z > 2$, less polarisation and, in one case, stellar absorption lines have been found (Dey et al., 1997). The implication is that the aligned continuum is produced by scattered light from a hidden quasar at low redshift, with increasing contributions of newly formed stars, possibly triggered by the passage of the jet.

Recently, an alignment was also proposed for the extended X-ray emission (Carilli et al., 2002). While at the time of writing, there was only one HZRG observed with Chandra, and the measurement errors are considerable, the possible implications are interesting: The only extended X-ray emission seen in PKS 1138-262 at $z = 2.2$ is highly aligned with the radio jet, and probably heated by the bow shock. The unshocked density is $n = 0.05\,\mathrm{cm}^{-3}$ at 100 kpc from the nucleus and the total mass of hot gas $2.5 \times 10^{12}\,M_\odot$. The density is similar to inter-galactic medium (IGM) densities infered from emission line studies (van Ojik et al., 1997), and about a factor of five higher than in Cygnus A, which already resides in a comparatively dense environment.

Environment

It has been argued that the cluster environment of powerful radio galaxies changes substantially with redshift, invoking predominantly rich clusters (or proto-clusters) at higher redshift (Hill and Lilly, 1991; Hill et al., 1993; Best, 2000). New results by McLure and Dunlop (2001) suggest that the comoving space density of clusters at low redshift is almost equal to that of powerful AGN at $z \approx 2.5$. Given that in most cases only the dominant, first ranked elliptical develops a powerful AGN, this implies that all the cluster dominant galaxies were active at $z = 2.5$, and that the powerful radio galaxies at high redshift are located in (proto-) cluster environments. Recently, the environment of HZRG has been searched for Lyman α emitters (Kurk et al., 2001b). The results obtained on two HZRG confirm the above prediction: About 20 objects with spectroscopic redshift have been found around each radio source. At the time of writing this project is still going on.

The nearby Virgo cluster of galaxies with its famous AGN Messier 87 should be a typical example (Camenzind, 1999). The current radio jet is weak, but low frequency radio images show extended emission further out (Klein, 1999), which are interpreted as relics from earlier, recent ($\approx$ 100 million rears old) outbursts. This shows at least that the current (low) activity phase was not the only one in the days of M87. A black hole of three billion solar masses was found at the center of M87. Therefore it is quite plausible that M 87 was much more active in the past.

Dust

Interestingly, the amount of dust in radio galaxies increases with redshift to more than $10^8 M_\odot$ at $z = 4$, measured from infrared observations (Carilli et al., 2001, and references therein). Measurements of CO emission even imply more than 10^{10} solar masses of gas in a few HZRG (Papadopoulos et al., 2001). The presence of large amounts of dust is also implied by the favoured explanation of the continuum alignment effect via scattering by dust grains (McCarthy, 1993). This is puzzling, since the passage of the radio jet should have easily destroyed dust grains in a short time compared to the radio source age (Villar-Martín et al., 2001; De Young, 1999). As De Young (1998) has calculated in detail, for dust grains to survive the passage of the radio jet, the bow shock has to be slower than $\approx$ 10,000 km/s or the clouds hosting the dust have to be denser than 1000 cm^{-3}. He also points out that rapid cooling behind the bow shock would favour dust survival. If those conditions do not apply, one has to think of other processes, such as dust production by newly formed stars, triggered by the passage of the jet (De Young, 1989).

I.2 On the History of Jet Simulations

Basic model

Jet simulations have been reviewed by Ferrari (1998) and Norman (1993). Two-dimensional simulations started with Rayburn (1977). Norman et al. (1982) introduced the finite difference approach to jet modelling, which is now widely used, also in this work. These simulations, and follow-up work, established the basic model for extragalactic jets (Fig. I.7): A beam is collimated by magnetic forces or external pressure. Within this beam, oblique, crossing shock waves are present. They have a rarefaction zone upstream, and a compression zone downstream, and can move forward and backward through the beam. Each time they reach the jet head, the head gets accelerated by the high pressure region in front of the oblique shocks. Also the collimated jet plasma constantly catches up to the jet head. There it is shocked in the Mach disk, forms a high pressure, hot spot, and is pushed aside, where it flows backwards in a cylinder around the jet beam. The flow gets turbulent, also interacting with oblique shock waves in the beam, and thereby establishing a complex feedback mechanism. This shocked jet plasma is also called cocoon, and was identified with the radio lobes. Because of the supersonic velocity of the hot spot, a bow shock is created in the ambient material, which is separated from the shocked jet plasma by a contact discontinuity.

2D simulations

Norman et al. (1983) then performed a parameter study, and summarised the basics of adiabatic, Newtonian, hydrodynamic jet simulations. The parameter space consists of three dimensions: The ratio of jet to ambient pressure (κ), the ratio of jet to ambient density (η), and the beam Mach number M (ratio of beam velocity to average beam sound speed). As large scale jet beams are not observed to contract or expand by much, the pressure ratio has to be approximately one. This value is used in most jet simulations, and also by Norman et al. (1983). They restricted the Mach number to greater then one because they anticipated 3D effects to be dominant in low Mach number flows. To the high end there is in principal no limit, but they considered only jets with $M < 10$. The density contrast was restricted to $0.01 < \eta < 10$. Jets that are denser than that are essentially ballistic. They protrude through the ambient matter almost unaffected, like a solid rod. Lowering the jet density produces more extended cocoons of shocked jet plasma around the jet. Because radio galaxies, in general, show extended synchrotron emitting cocoons, they were identified with, light ($\eta < 1$) jets. Jets of young stellar objects do not show such extended cocoons. Therefore, they were identified with heavy ($\eta \geq 1$) jets. These results justify that in the following only light jets are considered. The range $\eta < 0.01$ was not explored, because those jets propagate very slow, in reality and, even more important, in the computer.

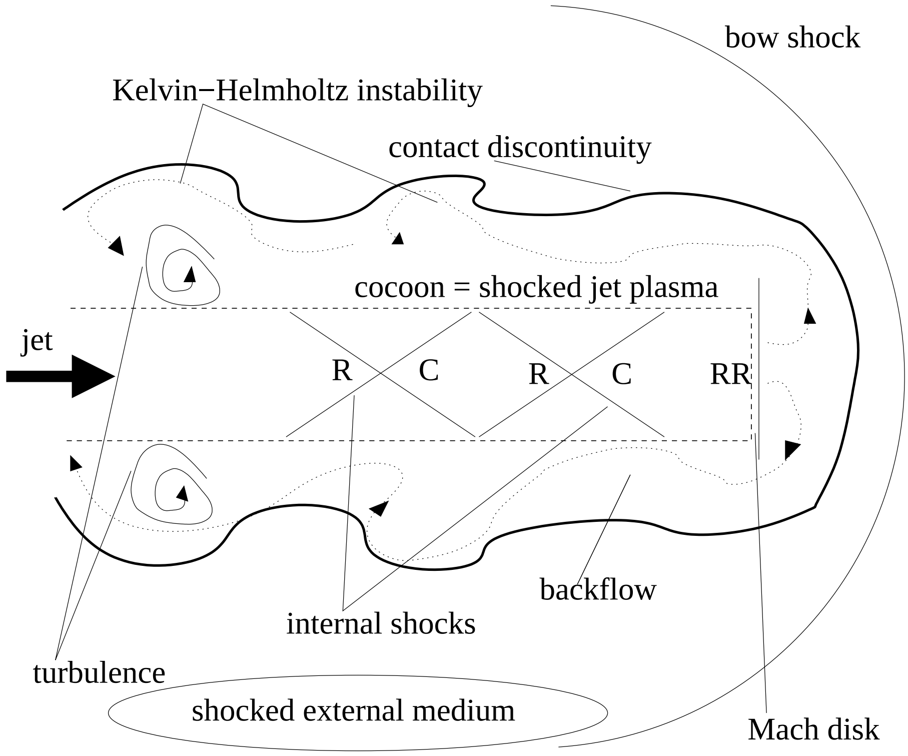

Figure I.7: *Standard jet model. R denotes rarefaction, and C compression zones*

The advance speed of the jet head can be determined from force balance at the contact discontinuity, in the rest frame of the contact discontinuity. The force from the jet is: $[\rho_\mathrm{j}(v_\mathrm{j}-v_\mathrm{cd})^2+p_\mathrm{j}]A_\mathrm{j}$ (see appendix for symbol explanations). The index j refers to jet values, v_cd is the velocity of the contact discontinuity at the jet head in beam flow direction, which can be equated with bow shock and hot spot velocity. The force from the ambient medium is: $[\rho_\mathrm{m}v_\mathrm{cd}^2 + p_\mathrm{m}]A_\mathrm{head}$, where the index m denotes quantities in the ambient medium. A_head is the area of the jet head, across which the contact discontinuity is pushed forward. This head area is usually larger than the beam area. Its exact amount has to be determined from numerical simulations. Expressing the pressure as $p = \rho v^2/\gamma M^2$ (γ: adiabatic exponent), leads to

$$\frac{v_\mathrm{j}}{v_\mathrm{cd}} = \frac{1}{\sqrt{\eta\epsilon}}\sqrt{\frac{1+1/\gamma_\mathrm{m}M_\mathrm{cd}}{1+1/\gamma_\mathrm{j}M_\mathrm{j}}} + 1. \tag{I.1}$$

ϵ is the ratio of beam to head area. For high Mach numbers (I.1) is commonly approximated by

$$v_\mathrm{cd} = v_\mathrm{j}\frac{\sqrt{\eta\epsilon}}{1+\sqrt{\eta\epsilon}}. \tag{I.2}$$

Norman et al. (1983) showed that for heavy jets, ϵ is close to one. The heads of light jets expand more, and ϵ can reach values as low as 0.1. Since the hydrodynamics of the jet head turns out to be quite complex, ϵ was found to be a function of resolution (this thesis, Kössl and Müller, 1988).

The cocoon broadening can also be estimated analytically (Begelman and Cioffi, 1989; Norman, 1993). Idealising the cocoon as a cylinder with volume $V = \pi r_c^2 h$, given also by its energy E and pressure p, $V = (\gamma - 1)E/p$, and assuming the distance from core to jet head h to be $h = v_{\text{head}} t$, with the average head advance speed v_{head}, and the cocoon energy E to be $E = \alpha L t$, where $L \equiv \pi R_j^2 v_j^3 / 2$ is the average kinetic jet luminosity, one can easily calculate the cocoon width (for light supersonic jets, pressure matched with the cocoon):

$$\frac{r_c}{R_j} = \sqrt{\frac{\alpha\gamma(\gamma-1)M_j^2}{2\sqrt{\eta}}}. \tag{I.3}$$

This confirms the simulation results of e.g. Norman et al. (1983) that the cocoon grows with Mach number and gets smaller with growing η.

3D simulations

Three-dimensional (3D) simulations (Williams and Gull, 1985; Arnold and Arnett, 1986; Cox et al., 1991; Clarke, 1993) have shown that the backflow not only decays into vortices with poloidal velocities, which is observed in the 2D case, but also toroidal (perpendicular to the jet direction) velocities are observed. In general, the cocoon is more complex in 3D. This confirmed the earlier suspicion that the cocoon is turbulent. Because of the limited numerical resolution, the nature of the turbulence could not be studied in detail, so far.

One of the first studied 3D-phenomena was the generation of secondary hot spots. Two mechanisms were proposed that work at different density contrast. For low density contrast ($\eta < 0.05$, Norman and Balsara, 1993), the jet beam, jittering around its axis, can be deflected at the contact discontinuity (Williams and Gull, 1985). Because of the high density there, the contact discontinuity moves slowly (I.2), and behaves essentially like a wall. This deflection creates the primary hot spot. Where the contact discontinuity is hit for the second time, a secondary (*splatter*) hot spot is created. The other model invokes a precessing jet (Cox et al., 1991). Here the primary hot spot is the current working surface, whereas the secondary hot spot is a quickly fading earlier working surface. Both mechanisms work in simulations.

3D hydrodynamical simulations have been used to model various environmental conditions. E.g. Norman and Balsara (1993) have calculated a Mach 3.8, $\eta = 0.2$ jet with a Mach 1.2 crosswind, a Mach 2, $\eta = 0.02$ jet, encountering an oblique Mach 2.8 shock wave, a Mach 4, $\eta = 0.2$ jet, encountering an $\eta = 50$ cloud, and a Mach 5, $\eta = 0.03$ jet, hitting a contact discontinuity at different angles. They could reproduce the morphology of narrow angle tailed radio sources, wide angle tailed radio sources, perpendicularly deflected jets, and splatter hot spots, respectively.

Magnetic fields

Because jets are detected by their synchrotron emission, they are required to carry magnetic field. For a self-consistent treatment, calculations with the full set of magnetohydrodynamic (MHD) equations are required. The 2D MHD jet simulations fooled the researchers for some time due to a strong axisymmetric effect (Clarke et al., 1986; Lind et al., 1989; Kössl et al., 1990b): It was found that for fields of strong magnetic pressure, compared to the thermal pressure, the Lorentz force is able to collimate the shocked jet plasma in front of the Mach disk into a *nose cone*. The nose cone was shown to be unstable in 3D simulation (Clarke, 1993). Already 2D simulations revealed that beam and cocoon can be collimated by a toroidal field, and decollimated by a poloidal field (Kössl et al., 1990a). The first result could be confirmed in 3D by Clarke (1993).

He also found that the magnetic field in a jet is, independent of its strength, concentrated in filaments mainly on beam and lobe surface. He attributed this particular arrangement to the velocity shear at those boundaries. These filaments are the ideal locations for reconnection events, producing relativistic particles, which then radiate the synchrotron radiation (Lesch and Birk, 1998). Synchrotron emission in jets is extended. The lifetime of locally generated relativistic particles (see below) is typically too short to be able to travel to the places where they are observed (Meisenheimer, 1996). Particle reacceleration could take place in those filaments.

Non-thermal ingredients

Magnetic fields are not yet enough for the construction of realistic emission maps. Another important part is the abundance of relativistic particles. These particles are accelerated in reconnection events (see above) and at shocks (Ferrari, 1998). The transport, shock acceleration and synchrotron cooling of a relativistic electron population carried by a non-relativistic magnetised jet has been studied in 3D by Tregillis et al. (2001). There results show that the terminal shock, present most of the time in 2D simulations, dissolves into a *shock-web complex*. This complex is still a high pressure region. But the beam material can now pass through shocks of varying strength, with a high chance to turn around without passing a shock. Consequently, the simulated radio maps show an extended area around the jet head, where bright emission is found. They confirm that the magnetic field is concentrated in filaments even in the cocoon, where it is generally about an order of magnitude less than in the beam.

Relativistic jets

Another important aspect of jet physics is their high velocity, close to the speed of light, at least close to the AGN. Due to the sophisticated algorithms and the large computational power required, simulations of relativistic jets were carried out only recently. At the time of writing, no large scale 3D simulation of a magnetised relativistic jet came to the knowledge of the author.

A hydrodynamic relativistic 3D jet has been simulated by Aloy et al. (1999). One of the most important effects is the relativistic mass increase. This increases the effective beam density by Γ^2, where Γ is the bulk Lorentz factor. Consequently the $\eta = 0.01, \Gamma = 7$ jet of Aloy et al. (1999) is effectively nearly ballistic, developing only a small cocoon. Furthermore, the jet is more stable than non-relativistic jets, both magnetised and non-magnetised. It is essentially a straight line.

2D simulations of relativistic jets with toroidal field yielded very similar results than the non-relativistic ones, if one takes into account the relativistic mass increase (Komissarov, 1999). 3D simulations have been performed only up to an axial extention of 20 jet radii (Nishikawa et al., 1997, 1998). The preliminary results indicate no spectacular new feature.

Protons or positrons?

So far, it was always assumed that the jet plasma consists of a proton-electron plasma. However, there is no consensus on the nature of the beam material. Recent developments enabled the inclusion of special equations of state into a relativistic hydrodynamic code. Scheck et al. (2002) simulated a cold baryonic, a hot leptonic, and a cold leptonic jet. The results are strikingly similar, concerning morphology and dynamics. Besides a more knotty structure in the synthetic radio map of the hot leptonic jet, the main observational criterion for discerning between the different jet ingredients may be the thermal bremsstrahlung emission. While for all models a X-ray cavity is created, because the thin jet material pushes the X-ray atmosphere aside, at energies above 10 MeV the emission from the hot (10^{12} K) cocoon begins to dominate over the shell emission in the baryonic and hot leptonic case. Because of the comparatively cold cocoon (10^{11} K), this is not the case in the leptonic cold jet.

Stability analysis

Besides the numerical study of jets propagating in an undisturbed ambient medium, there has been considerable and increasing interest in the stability properties of jets during the last decade. The main agent of instability and possible destroyer of the jet is the Kelvin-Helmholtz (KH) shear instability. A fundamental result of its linear analysis (Appl and Camenzind, 1992; Appl, 1996) is that hydrodynamical jets without magnetic field are unstable to KH instabilities of a wide range of wavelengths, while jets with a poloidal field and even more those with a toroidal field in the cocoon (a distribution which is supported by simulation results, see Kössl et al. (1990a)) are essentially stable to small wavelength perturbations. Stability increases also with Mach number. The development of long wavelength instabilities into the nonlinear regime was investigated for the hydrodynamical case in cylindrical and slab symmetry and in three dimensions by Bodo and coworkers (Bodo et al., 1995, 1994, 1998), respectively). They find that the instabilities destroy the jet in a time comparatively small with respect to the typical lifetime of an astrophysical jet source. This disruption could be proven to be less severe in the case where the jet is denser than the surrounding medium, when radiative losses are taken into account (Micono et al., 2000, for the three dimensional case), and is even impeded if one includes an equipartition magnetic field (Hardee et al. (1997), three dimensional, poloidal fields; Rosen et al. (1999), three dimensional, also toroidal fields).

At the time of writing, many interesting jet simulations are still limited by the available computing power. Therefore, it can be expected that progress in computer technology will also advance the simulation of jets and finally the understanding of their physics.

I.3 Aim & Outline

Two fortunate instances had to come together for this project to emerge. At first, the observations of ever higher redshifted radio galaxies showed that these objects are located in comparatively dense environments. Extended emission line regions like e.g. in 3C 368 (Meisenheimer and Hippelein, 1992), gave clear hints that cooling in post-shock regions could be important at least in some cases to produce them. The evidence of shock induced star formation in 4C 41.17 at $z = 3.8$ (Dey et al., 1997) further supported the idea of dense environments.

On the other hand, the radiation MHD code NIRVANA_CP, originally coded by U. Ziegler (Ziegler and Yorke, 1997), and upgraded due to optically thin cooling by M. Thiele (Thiele, 2000) at the Landessternwarte theory group, became ready for use. Consequently, it was decided to use NIRVANA_CP to study the propagation of jets into a dense medium, including cooling of that gas.

Simulations of jets had been made with NIRVANA_CP only in the protostellar regime, so far. Therefore, the reliability of the code, for parameters applicable to extragalactic jets, had to be established, firstly. This has been carried out, and, after a basic description of the methods and the code used in chapter II, which also includes the code adaptation for running on the NEC SX-5 supercomputer, the results of a comparison of NIRVANA_CP recomputations with two refereed simulation results are described in chapter III. Considerations about the basic jet parameters for HZRG lead to low density contrasts (η). Therefore, a parameter study was carried out in chapter IV in the region of $10^{-5} < \eta < 10^{-2}$. This region was unexplored so far, due to computer power constraints. Next a simulation with time implicit cooling of shocked external material for parameters assumed to be typical for powerful HZRG is presented. Because the results show that very interesting things happen in the plane of symmetry, the remaining simulations are in bipolar mode: A 3D simulation with both jets simulated is presented in chapter VI. This simulation was carried out for parameters from the literature for the nearby radio galaxy Cygnus A, because recent Chandra observations could identify for the first time the clear shape of the bow shock in this source. The shape of the bow shock turned out to be a good indicator for the underlying physical model assumed. The considered parameters failed to reproduce the Cygnus A bow shock. Nevertheless, by comparison to the model, the conditions in Cygnus A can be constrained. Cygnus A is an extraordinary source, and can serve as a nearby model for HZRG, in many respects. In chapter VII, again a 2D simulation is presented. A realistic density profile is used, and cooling is done in a more approximate, time explicit, way. This saves computational resources, gives almost as good results as the implicit version and allows higher resolutions or, at low resolution a long time study of a bipolar jet on a large grid. Both strategies are followed. The last chapter gives a short summary of the results obtained in this work.

I.4 Units & Constants

The CGS system is widely used in astronomy, and is also applied in this work. However, for large scale jets there is a typical length scale of 1000 parsec, abbreviated kpc ($= 3.0856 \times 10^{21}$ cm), and a typical time scale of 10^6 years which is abbreviated by Ma (for Mega-annum, corresponding to 3.156×10^{13} s) in this work. With this typical scale, one can construct a typical velocity: 1 kpc/Ma = 978 km/s. The speed of light in these units is 307 kpc/Ma. Where not stated explicitly, a Hubble constant of 65 km/s/Mpc was used.

Chapter II

Numerics

The numerical computations in this work were carried out with the 3D non-relativistic radiation MHD code NIRVANA_CP. The MHD part was coded by U.Ziegler (Ziegler and Yorke, 1997). Optically thin cooling was added by M.Thiele (Thiele, 2000). The code was vectorised with Open-MP like methods, tested and run on the shared memory super-computer NEC-SX5. The results in chapter VI, and partly chapter VII, were obtained on the SX5. The numerics is described in more detail in Thiele (2000) and Ziegler and Yorke (1997).

II.1 The Magnetohydrodynamic Approximation

The study of extragalactic jets in this work is completely based on the assumption, that all the plasmas under consideration can be properly described by the theory of magnetohydrodynamics. However, this is only correct, if the characteristic scale length (the jet radius $\approx$ kpc) is large compared to the mean free path (Priest, 1994):

$$\lambda_{\mathrm{mfp}} \approx 1 \left(\frac{T}{10^9\mathrm{K}}\right)^2 \left(\frac{n}{\mathrm{cm}^{-3}}\right)^{-1} \mathrm{kpc}. \tag{II.1}$$

Since the density in the jet is much lower than 1 cm^{-3} and the temperature can easily exceed 10^9 K, and can even reach 10^{13} K, this condition is clearly not satisfied. Therefore, one has to assume that the magnetic field provides the coupling between the particles in the jet plasma. In this work, the jet is considered to consist of thermal protons and possibly non-thermal electrons. The non-thermal electron component is not modeled here. However, for an understanding of the synchrotron emission a self-consistent treatment with a two-component plasma will be necessary. This is beyond the scope of this work.

II.2 The Code NIRVANA_CP

The MHD part of NIRVANA_CP is identical to the NIRVANA basis and solves the following equations in 3D for density ρ, velocity $\mathbf{v}$, internal energy e, and magnetic field **B**:

$$\frac{\partial \rho}{\partial t} + \nabla \cdot (\rho \mathbf{v}) = 0 \tag{II.2}$$

$$\frac{\partial \rho \mathbf{v}}{\partial t} + \nabla \cdot (\rho \mathbf{v}\mathbf{v}) = -\nabla p + \frac{1}{4\pi}(\mathbf{B}\cdot\nabla)\,\mathbf{B} - \frac{1}{8\pi}\nabla \mathbf{B}^2 \tag{II.3}$$

$$\frac{\partial e}{\partial t} + \nabla \cdot (e\mathbf{v}) = -p\,\nabla \cdot \mathbf{v} \tag{II.4}$$

$$\frac{\partial \mathbf{B}}{\partial t} = \nabla \times (\mathbf{v} \times \mathbf{B}), \tag{II.5}$$

where the pressure p is given by: $p = (\gamma - 1)e$, with the adiabatic index γ which was assumed to be 5/3 everywhere. NIRVANA can be characterised by the following properties:

1. second order accurate
2. explicit Eulerian time–stepping,
3. operator–splitting formalism,
4. method of characteristics (MOC) / constraint–transport (CT)
5. artificial viscosity

ad 1) Standard finite difference and finite volume methods, similar to ZEUS (Stone and Norman, 1992a,b) were applied. The mesh is staggered, where scalars are defined in the corners and vectors on the center of the surfaces of the cells. The van Leer interpolation method is used, which gives second order accuracy.
ad 2) Explicit Eulerian time–stepping was implemented, with a Courant number of 0.5.
ad 3) Operator–splitting was applied in the advection part. The scheme computes the source terms first ($-\nabla p$, $-\nabla \mathbf{B}^2/8\pi$, and $-p\nabla \cdot \mathbf{v}$), then the artificial viscosity (see below), afterwards the magnetic tension part and the induction equation (see below). Finally, the advection is carried out.
ad 4) Magnetic tension ($(\mathbf{B}\cdot\nabla)\mathbf{B}/4\pi$) and induction equation (II.5) are treated by a MOC and CT algorithm (Thiele, 2000, and references therein). This method guarantees that the divergence of the magnetic field stays zero, if it was so initially. Alfvén waves are described correctly.
ad 5) Artificial viscosity terms have been included on the right hand side of momentum (II.3) and energy (II.4) equation. This dissipates high frequency noise and damps overshootings in shock regions, at the cost of smearing the shocks over a few grid cells.

Upgrading to NIRVANA_C due to optically thin cooling, Thiele (2000) replaced equation (II.4) by:

$$\frac{\partial e}{\partial t} + \nabla \cdot (e\mathbf{v}) = -p\,\nabla \cdot \mathbf{v} - \mathcal{K}. \tag{II.6}$$

He also added an additional equation due to generation and depletion of individual atomic species, with masses m_α, by ionisation and recombination:

$$\frac{\partial \rho_\alpha}{\partial t} + \nabla \cdot (\rho_\alpha \mathbf{v}) = k_\alpha \ . \tag{II.7}$$

$\mathcal{K}$ and k_α are computed by the following equations:

$$\mathcal{K} = \sum_{\alpha=0}^{N} \sum_{\beta=0}^{N} \frac{\rho_\alpha}{m_\alpha} \frac{\rho_\beta}{m_\beta} \Lambda_{\alpha\,\beta} \tag{II.8}$$

$$k_\alpha = m_\alpha \sum_{\beta=0}^{N} \left(\sum_{\gamma=\beta}^{N} \frac{\rho_\beta}{m_\beta} \frac{\rho_\gamma}{m_\gamma} \mathrm{IF}^{+}_{\alpha\,\beta\,\gamma} - \rho_\alpha \frac{\rho_\beta}{m_\beta} \mathrm{IF}^{-}_{\alpha\,\beta} \right) \ , \tag{II.9}$$

where the Λ and IF functions summarise the details of atomic physics and are functions of temperature and, in general, also of the number densities ρ_α/m_α. Λ can also be used to include bremsstrahlung, which was done in chapter V, or cyclotron emission.

II.3 Porting to NEC SX-5 Supercomputer

Part of this work was a further upgrade of the code (to *NIRVANA_CP*) consisting in vectorisation and parallelisation for use on a NEC SX-5 computer by OPEN_MP like methods, provided by the standard NEC C compiler for this machine. The SX-5 is a shared memory machine. Therefore the changes are moderate. Particularly, no domain decomposition or data transfer between processors had to be coded, like in the distributed memory case, because all the up to 16 processors have access to the whole memory. The code was revised and fine tuned in order to achieve the maximum possible performance for the given hardware. So far, the code was used with one processor only. A performance of approximately 10^9 floating point operations per second (FLOPS) was achieved, which corresponds to 25% of the peak performance.

II.3.1 Test calculations

The reliability of the code was tested by computing test problems with the new code version on SX-5 and comparing the result to the output of the old – sufficiently validated – version run on a Linux PC. Since in this work only hydrodynamic calculations were performed on the SX-5 (chapters VI and VII), a hydrodynamic test problem with one species is reported.

The one-dimensional Sod shock problem was computed, which even has a semi-analytic solution (Courant and Friedrichs, 1948). A grid with 4095 cells was used in order to get the maximum possible vectorisation efficiency. This grid was initially divided into two areas. On the left-hand side, density and temperature were set to one, and on the right-hand side they were set to 0.125

Table II.1: Initialisation for Sod Shock Problem

Variable	Left Hand Side	Right Hand Side
ρ	1.0	0.125
T	1.0	0.8
v	0.0	0.0
γ	1.4	1.4

and 0.8, respectively. The velocity was zero, everywhere, and the adiabatic index 1.4.

Due to the ten times higher pressure on the left hand side, a shock wave develops. The computation was carried out both on a Linux PC and on the NEC SX-5 at the High Performance Computing Center in Stuttgart (HLRS). The result after 6000 timesteps and a physical time of 2.3×10^{-5} is shown in Fig. II.1 Differences between the two computations could be found only in the velocity in regions where it is close to zero. This velocity differences of the order $\Delta v \approx 10^{-12}$ should reflect the numerical truncation error. The test calculation also demonstrates the high suitability of *NIRVANA_CP* in the handling of shock waves. As is shown in Table II.2, a high degree of vectorisation was achieved.

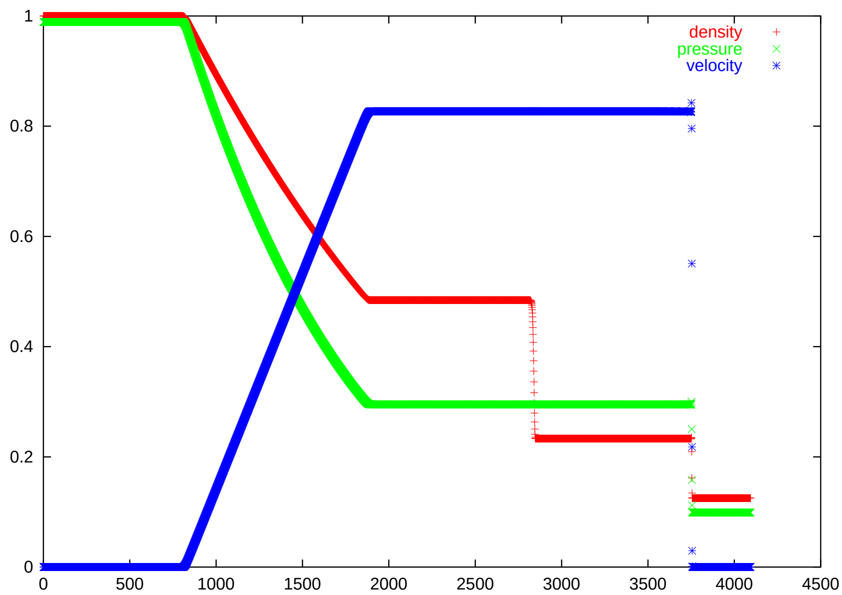

Figure II.1: *Density, pressure and velocity for the Sod shock test problem after 6000 timesteps, corresponding to a physical time of* $2.3\ 10^{-5}$. *The output from the SX-5 computation is plotted, but the output from the PC would be indistinguishable on this graph. The units are normalised in order to fit in the graph, and on the horizontal axis, grid points are indicated.*

85% of the user time the code was in vector mode, the vector operation ratio was

99.3%, and with the one SX-5 processor used here, a FLOP rate of 1.0 GFLOPS was achieved. This is the expected value, given the maximum performance of 4 GFLOPS, which only can be achieved if the instructions are especially fine tuned. The high vectorisation degree also was indicated by the compiler report: almost every significant loop was vectorised.

Table II.2: Profile Information for Sod Test

****** Program Information ******			
Real Time (sec) :	12.189758	User Time (sec) :	8.827777
Sys Time (sec) :	0.628303	Vector Time (sec):	7.538145
Inst. Count :	306726730	V. Inst. Count :	110947808
V. Element Count:	27955444095	FLOP Count :	8572226294
MOPS :	3188.936809	MFLOPS :	971.051522
A.V. Length :	251.969323	V. Op. Ratio (%):	99.304546

II.4 Boundary Conditions for the 3D Cylindrical Grid

The cylindrical grid is used for a 3D simulation in chapter VI. The disadvantage of the cylindrical coordinates (Z, R, ϕ) compared to the Cartesian ones is the appearance of internal boundaries. The grid has to be connected somehow over these boundaries. In the ϕ direction, periodic boundary conditions were applied. In a test problem for the advection part, a pulse could be advected over such a boundary without energy or mass loss. This is only possible because in the advection part of the solver a total variation diminishing (TVD) scheme is applied. For the boundary on the axis, no analogue could be found in the literature. The boundary condition here is similar to the periodic case: One side of the grid should know about the other side. Therefore, three cells were used below the axis, to which consequently the index $i_R = 3$ was assigned. With this choice and the staggered mesh, equations (II.2-II.5) are well defined everywhere on the grid. For the scalar quantities, the following boundary conditions were applied:

$$\begin{aligned} f(i_Z, j, i_\phi) &:= f(i_Z + i_\pi, 6 - j, i_\phi) \quad , j = 0, 1, 2 \\ f(i_Z, 3, i_\phi) &:= < f(i_Z, 3, i_\phi) > |_{i_Z = \text{const}} \; , \end{aligned}$$

where i_π denotes the number of grid cells corresponding to the angle π. The last equation indicates that directly on the axis , the scalars were averaged over i_ϕ for constant i_Z, since all the different i_ϕ refer to the same physical point. Due to the staggered mesh, the Z and ϕ components of vectors are shifted by half a grid cell away from the axis. Therefore for these components, there arise

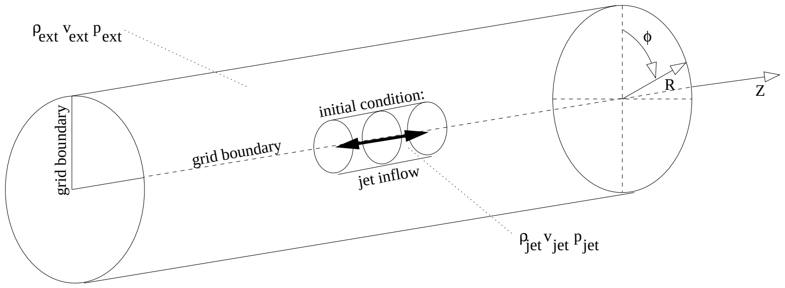

Figure II.2: Sketch of the cylindrical grid.

no special problems, and the boundary condition is:

$$v_{Z,\phi}(i_Z, j, i_\phi) := v_{Z,\phi}(i_Z + i_\pi, 5 - j, i_\phi) \quad , j = 0, 1, 2$$

The radial vector components are not shifted away from the axis. So, in principal they all denote the same physical point. However, the flow should be allowed to cross the axis from one side to the other. This is only possible, if the radial velocity takes a reasonable value there. Therefore, two possibilities arise for the boundary conditions:

$$\begin{aligned} v_R(i_Z, j, i_\phi) &:= -v_R(i_Z + i_\pi, 6 - j, i_\phi) \quad , j = 0, 1, 2 \\ v_R(i_Z, 3, i_\phi) &:= \begin{cases} 0 & : \text{ case I} \\ (v_R(i_Z, 4, i_\phi) - v_R(i_Z, 2, i_\phi))/2 & : \text{ case II} \end{cases} \end{aligned}$$

In order to check the influence of these two different boundary conditions on the simulation, the jet from chapter VI was simulated twice, the first time with the case I, and the second time with the case II boundary condition. For both runs, the integrated quantities (directionally split energy and momentum, and mass) and also the timesteps were equal. Also, from comparison of the contour plots, no difference could be found. Hence, the flow seems to have enough possibility to flow past the axis, and the detailed behaviour at that line does not influence the result by much. The simulation result also shows, that this approach in general works fine in regions of undisturbed jet flow. Where the jet is dominated by instabilities and wants to bend, the axis looks like an obstacle. Therefore, the method seems to be problematic if details about the jet beam are of special interest. Nevertheless, the results confirm that the representation of the beam is acceptable, and for the other regions the output was fine. There are severe advantages of the cylindrical grid:

1. Since the jet itself has cylindrical geometry, the required volume for the computational domain is reduced by $1 - \pi/4 \approx 22\%$ (for a grid of equal extension in R and positive Z direction).

2. The grid points are naturally concentrated in the area of the jet beam. This is preferable if no cooling of the external medium is taken into account or if the cooling length there is long.

3. There is one special axis (the Z axis) with much more points than the two other directions. This increases the performance for vectorisation, since only inner loops – and therefore one of the directions – are vectorised.

Chapter III

Inter-Code Reliability and Numerical Convergence

The code Nirvana was sufficiently validated concerning MHD test problems (Ziegler and Yorke, 1997) as well as the cooling part (Thiele, 2000). However, the code was not used for the simulation of light extragalactic jets, before. Since also numerical convergence cannot be expected because of computer power limitations and the partly turbulent nature of the problem (Kössl and Müller, 1988), it is not a priori clear how trustworthy individual features are. So, it was decided to test the behaviour of Nirvana in the regime under consideration in comparison to published results, both for the magnetised, and also for the pure hydrodynamic case. It turned out to be of great advantage that one of the reference simulations was a resolution study. So, a statement about the effectiveness of Nirvana compared to other codes could be derived. The resolution study could be extended with Nirvana, resulting in a very high resolution simulation with 400 points per beam radius. This revealed interesting, new, insights especially into the physics of jet boundary layers.

Nirvana and the two codes it is compared to are all second order accurate with van Leer interpolation. A hydrodynamic or MHD code constructed after the van Leer scheme is certainly less effective than a code with a piecewise parabolic method (Kössl and Müller, 1988; Woodward and Colella, 1984). Woodward and Colella (1984) showed that besides strong differences in a 1D test problem, the second order accurate codes they tested performed overall equally well in a 2D test, although differences occurred in some details. They note (Woodward and Colella, 1984, p166): *Does the accurate representation of a jet in one part of the flow compensate for the presence of noise in another part?* So, it really depends on the problem, which code is best suited. For astrophysical jet simulations, there is no comparison of the results of different van Leer scheme codes available, up to now. This study is the first attempt, to the knowledge of the author, to compare the output of different codes in the field of jet simulations, so far. It can be expected that an understanding of the different representations of hydrodynamical features in the different codes will also increase the confidence in jet simulation results in general.

III.1 Description of the Codes

The reference codes are a two dimensional MHD code by Lind (Lind, 1987; Lind et al., 1989), named *FLOW*, and an also two dimensional HD code by Kössl (Kössl and Müller, 1988), hereafter *DKC*. A precise description of FLOW can be found only in Lind's Ph.D. thesis (Lind, 1987). There, Lind points out two special features of FLOW. First, it uses a predictor corrector algorithm for the timestep calculation and second, a specific advection method is applied. This method considers the matter density flux as the primary advective quantity and calculates the remaining fluxes by multiplying the matter density by the specific density in the cell origin. It is not a Godunov scheme, and does not use an exact or approximate Riemann solver. All these codes use explicit Eulerian time stepping. They are second order accurate and use a monotonic upwind differencing scheme. They treat the standard set of ideal (magneto-) hydrodynamic equations (II.2-II.5): Instead of the internal energy e, FLOW and DKC use the total energy $u = \rho v^2/2 + e + B^2/8\pi$. Equation (II.4) is then replaced by:

$$\frac{\partial u}{\partial t} + \nabla \cdot (u\mathbf{v}) = -\nabla \cdot (p\mathbf{v}). \tag{III.1}$$

This is analytically equivalent, but may give different numerical results, in particular in regions of discontinuous flows. Another difference of the codes is the use of artificial viscosity. FLOW has no need for artificial viscosity at all, according to test calculations reported in Lind (1986). DKC and Nirvana use an artificial viscosity in order to enhance the diffusion in regions of strong gradients. This has the effect that shocks are transported correctly without numerical oscillations at the cost of smoothing the shocks over some grid zones. DKC even makes use of an antidiffusion term, which cancels the effects of artificial viscosity in regions of smooth flow. This point reflects the differences in the details of the implementation of the three codes as summarised in Table III.1.

Table III.1: Differences between the discussed codes

	FLOW	DKC	Nirvana
uses e			x
uses u	x	x	
art. viscosity		x	x
antidiffusion		x	

III.2 Hydrodynamic Jet Simulations

III.2.1 Numerical setup

As is appropriate for the simulation of axially symmetric jets (normalised) cylindrical coordinates (r,z) are used. The jet is injected into a homogeneous ambient medium. Density and the pressure there are set to unity. Therefore the sound speed in this external medium is $\sqrt{\gamma}$. The jets are injected in pressure equilibrium and have a density contrast of $\eta = 0.1$ which means that the jet material has 0.1 times the density of the ambient medium. The unit of length is the jet radius R_J. Velocity is measured in units of $\sqrt{p_\mathrm{m}/\rho_\mathrm{m}}$, where p_m is the pressure and ρ_m the density in the ambient medium, and the time unit is $R_\mathrm{J}/\sqrt{p_\mathrm{m}/\rho_\mathrm{m}}$. The units were chosen to match the normalised units in Lind et al. (1989) and Kössl and Müller (1988) as closely as possible. The boundary conditions are rotational symmetry at the jet axis, an outflow condition at the upwind boundary for setup A and an impenetrable wall for setup B and C (except for the nozzle). Open boundaries were applied on the two other sides besides setup C where outflow was specified in order to match the original conditions. This should have no noticeable effect, since inflows from those sides are hardly expected. The simulations are carried out at different resolution characterised by the number of grid points the jet beam is resolved with (ppb). Also, higher resolution images than in the original computations are added. Setup A and B recompute the results from Kössl and Müller (1988), where two simulations with higher resolution were added to setup B, and setup C is designed according to the hydrodynamic jet from Lind et al. (1989). The parameters are summarised in Table III.2. Note the following on the jet nozzle: In the MHD simulations, problems were encountered when the boundary condition was applied in the usual one grid zone only. Therefore the jet values were fixed in an area of four cells from the upwind boundary. In the simulations without magnetic field, the same was done, although it did not influence the results here.

Table III.2: Parameters of the jet models

Setup	A	B	C
Jet velocity v_J	24.5	24.5	25.0
Resolution (ppb)	40	10,20,40,70, 100,200,400	15,30
upwind boundary	outflow	reflecting	reflecting
comp. area (in R_J)	8×30	4×10	10×40
reference code	DKC	DKC	FLOW

III.2.2 Setup A: inter-code comparison of a time series

The time evolution of the jet model of setup A is shown in Fig. III.1. The times of the snapshots were chosen very similar to the corresponding model in Kössl and Müller (1988). Comparing the two computations, at the first glance, one recognises a great similarity: In both cases at early times, a laminar backflow is established, where the terminal Mach disk is nearly perpendicular to the z-axis. At $t = 3.18$ the laminar backflow phase terminates with the Mach disk becoming oblique and one of the forward and backward moving shocks from the beam extending into the backflow where it decelerates the backflow deflecting it away from the axis. The material to the left of this shock structure at approximately $z = 8$ at $t = 3.89$ is pumped off the grid and has disappeared at $t = 6.12$. The rest of the backflow material essentially stays at its place until the end of the simulation expanding from 2 up to 6 jet radii. Also visible in the simulation are the crossing oblique shock waves in the beam. So far the described features matched the corresponding ones in the

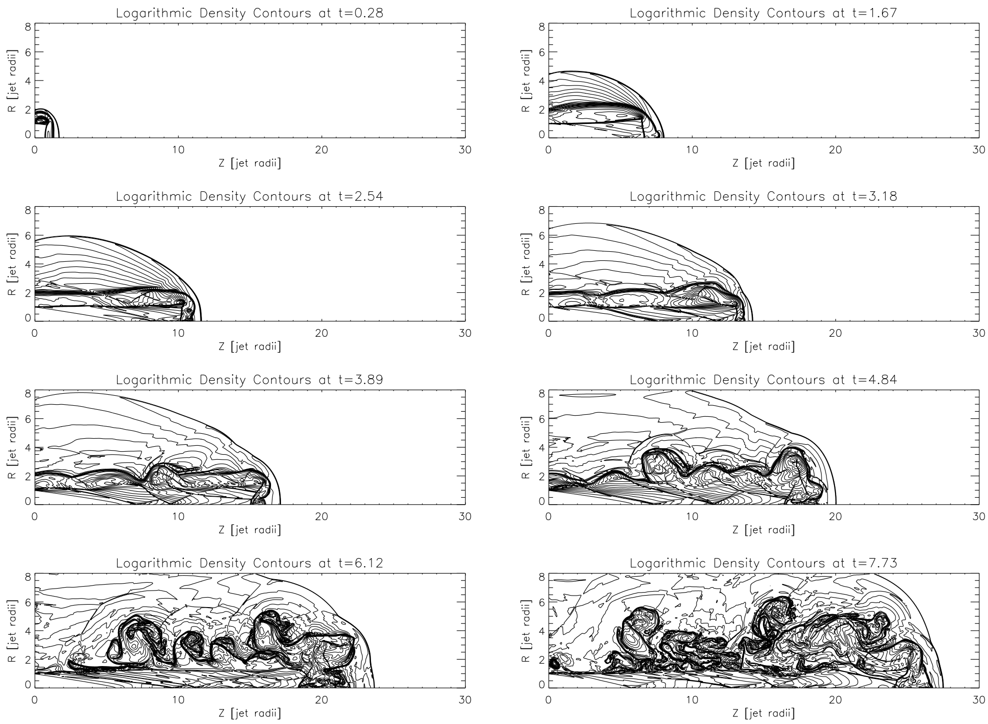

Figure III.1: *Contour plots of the density (30 logarithmically spaced lines) for the jet model of setup A. The times for the snapshots were chosen in order to match Fig. 11 of Kössl and Müller (1988) closely.*

original publication very well. In Fig. III.5 the bow shock velocity from this computation is compared to the one in the original publication. It shows a variation on the level of every evaluated timestep with an amplitude of roughly one in the Mach number. This was unrevealed in the original paper due to the lower sampling rate (23 versus 76 snapshots in this computation). The oscillation is modulated by a mode with longer wavelength (represented by the

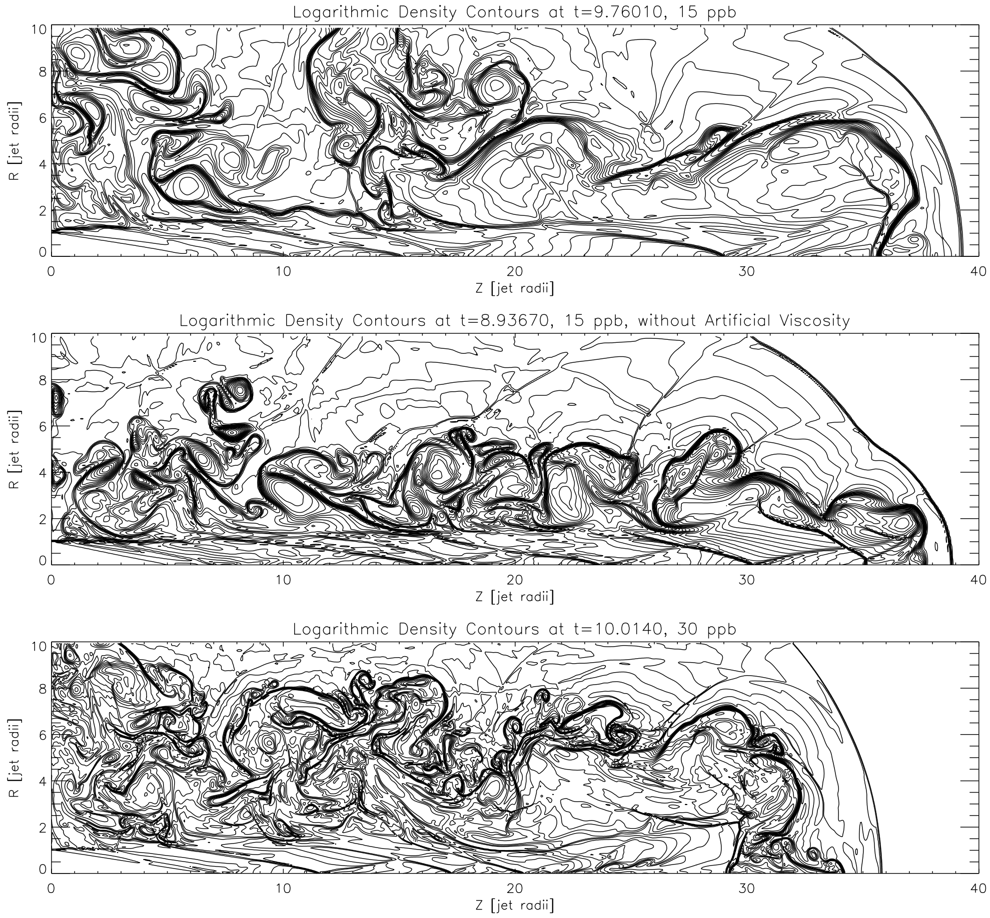

Figure III.2: *Logarithmic density plot of the jet from setup C. Top: 15 ppb resolution, t=9.76; middle: 15 ppb resolution without artificial viscosity, t=8.94; bottom: 30 ppb resolution, t=10.01*

smoothed curve in Fig. III.5) which is about 2 in the present results and 1.7 in Kössl and Müller (1988). They called this periodic de- and reaccelleration “beam pumping”. It was interpreted by Massaglia et al. (1996) in the following manner: The oblique shocks have a high pressure on the axis. Each time they arrive at the jet head, the head is accelerated due to this pressure gradient. Because of this phenomenon multiple bow shocks appear which can be seen in Fig. III.1 (especially at $t = 6.12$). The overall jet velocity decreases in the laminar phase in a similar way as in the DKC computation. But after $t \approx 4$ the decrease in the present computation is faster. At $t = 7.73$ the jet of the present computation has approached $z = 27.43$ which is 9% less than the reference value. At a first glance, it is surprising that the jet velocity decreases at all, for it was derived that the bow shock velocity should be constant (I.2). For the jet under consideration this bow shock velocity should evaluate to 5.9, approximately achieved in very early times of the simulation. The explanation for this decrease in the bow shock velocity was given by Lind et al. (1989): As the jet propagates, its head expands and ϵ in (I.2) decreases with time. It

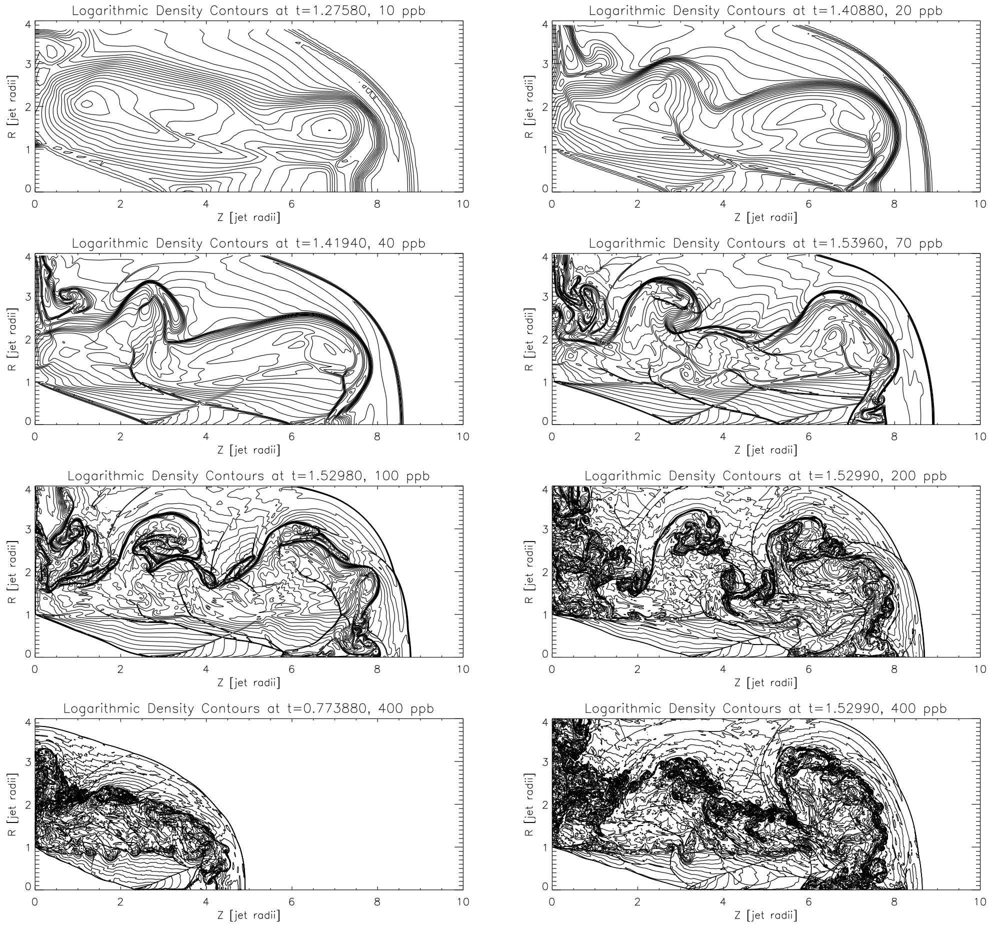

Figure III.3: *Jets from setup B. 30 logarithmically spaced density contours are shown. Time and resolution are indicated on top of the individual pictures.*

follows that the effective working surface for the jet is $\approx 3R_{\rm J}$ at late times of the simulation. This corresponds well to the extent of the jet head in the contour plots (Fig. III.1). A clear discrepancy between the simulations is the appearance of the Kelvin-Helmholtz (KH) instabilities. Where in the original publication only an unstructured bump is visible, in the Nirvana computation a round filigree system with additional instabilities can be seen. The observed differences could be caused by a different effective resolution of the two codes (This question will be examined in more detail in Sect. 3.4). So one can say that the qualitative behaviour of the simulation is well reproduced, which gives additional confidence in the quality of both simulations. But on a quantitative level there are differences. The Nirvana jet is slower at late times and develops a richer cocoon structure. The differences arise in the non-laminar flow phase.

III.2.3 Setup C: the effect of artificial viscosity

The reference paper for this subsection is Lind et al. (1989). They plot their hydrodynamic jet model at t=10 (in the units used here). This is not possible for the recomputation because at t=10 the Nirvana jet has left the computational domain. For that reason, the last timestep with the bow shock not having left the grid ($t = 9.76$, see Fig. III.2) is discussed. At a first glance, it seems that the Nirvana jet differs quite a lot from the reference jet: It propagates faster (average velocity of 4 versus 3.5), the region between bow shock and contact discontinuity on the axis (at z $\approx$ 36 in Fig. III.2) extends over one jet radius (versus three, compare Fig. III.6), the inner beam shock structure is by far more irregular in the recomputation and this prevents the cocoon from developing regular vortices. In the original publication the cocoon extended everywhere over about 7 jet radii, whereas at the end of the Nirvana simulation one vortex has even started to leave the grid over the upper boundary. Why are there such strong differences? In order to investigate this question the simulation was performed again with twice the resolution (Fig. III.2). The result is striking. The average velocity reduces to 3.6 which is only 2% higher than the 3.5 reference value. The region between bow shock and contact discontinuity is amplified to two jet radii (compare Fig. III.7), the cocoon extends over 8 jet radii, approximately, and in the interior of the beam there are more oblique shocks. This strongly suggests that with a little bit more than twice the resolution Nirvana reproduces the global parameters achieved in the FLOW simulation. Another reason for the differences might be the shock handling by methods of artificial viscosity in Nirvana. Therefore, the simulation was repeated at the original resolution (15 ppb), but without artificial viscosity. Artificial viscosity is not an option but a necessity in order to handle shocks correctly, for Nirvana. Fig. III.2 shows that there is now almost nothing of the cocoon material accumulating on the left hand boundary. Instead most of it is consumed in KH instabilities of approximately equal wavelength than in the original publication. There are more oblique shocks in the beam, too. It follows, that Lind's hydrodynamic jet simulation is, strictly speaking, not reproducible by Nirvana. But one can explain the shape of the cocoon by the different diffusivity description in Lind's code and the global parameters by a doubling of the resolution in Nirvana. The comparison between the recomputed 15 ppb and 30 ppb model clearly shows a strong dependence of the growth of the KH instability on the resolution.

III.2.4 Setup B: the numerical convergence of a hydrodynamic jet in comparison to Kössl and Müller (1988)

Details of the flow

The results are shown in a series of logarithmic density plots in Fig. III.3. The times for the snapshots were chosen in order to match the one in the original computation with an accuracy of better than one percent. Comparing the contour plots with the results from Kössl and Müller (1988) one can immediately see that they are very similar with the exception that Nirvana needed only about half the resolution to achieve the same result: At the resolution of 10 ppb, the conspicuous ledge at $(r, z) \approx (1.5, 8)$ of the contact discontinuity shows up which appears only at 20 ppb in the original. The hook like structure at

$(r, z) \approx (3, 1)$ can be seen for the first time in the 20 ppb plot with Nirvana and looks almost identical to the 40 ppb picture in Kössl and Müller (1988). Nirvana is able to resolve internal shock waves with the lowest resolution (10 ppb versus 20 ppb). Crossing shock waves become visible at 20 ppb (versus 40 ppb) and the upper right one of the cross like shocks appears at 40 ppb (versus $\approx$ 70 ppb). The inner beam also consists of plane and centered rarefaction waves (see Kössl and Müller (1988) for details) which one can identify at 10 ppb in the Nirvana simulation (versus 20 ppb). The cocoon is dominated by a prominent KH instability of wavelength ≈ 4 in the original publication which becomes somewhat shorter in the resimulations. It appears as a break in the contact discontinuity at low resolution. At 70 ppb in the Nirvana simulation, a round structure has formed which, approximately, retains this size up to 200 ppb. Only a part of the interior of this structure develops higher mode KH instabilities. This means that this region becomes turbulent. No sign of that can be seen in the DKC simulations. They resolve KH instabilities on the level of breakpoints in the contact discontinuity even at 100 ppb.

Kelvin-Helmholtz instabilities

At the highest resolution of 400 ppb, for the first time a completely different behaviour of the KH instability is discovered. A close look at Fig. III.3 shows that the amplitude of the dominant KH mode in the cocoon, which is continously growing at lower resolution, is only about half as big in the 400 ppb plot as in the 200 ppb plot. Furthermore, the contact discontinuity is turbulent almost everywhere, already at earlier times, when the dominant mode was not yet evolved (see lower left picture in Fig. III.3). This is quite contrary to the situation at lower resolution, where the longest wavelength mode develops first. Gray scale plots of the logarithmic density for the three highest resolution simulations at time $t \approx 0.5$ are shown in Figs. III.4 and III.8. They show that at 100 ppb the contact discontinuity between shocked ambient medium and jet backflow is smooth. This changes at 200 ppb. Here at about $R = 2$, evolved KH instabilities show up over about one jet radius. In the magnification, one can see that a high density flow emerging from the triple shock point at the Mach disk, which is also present at lower resolution, develops also KH instabilities. These two seem to interact with each other. In the 400 ppb gray scale plots, the bumps of the first one are located in immediate vicinity of the bumps of the other one. In the 200 ppb plot at $R \approx 0.8$, the bump in the inner flow even seems to hit the contact discontinuity. Furthermore, the two phenomena arise at the same resolution threshold. The bumps in the contact discontinuity are not stationary. They move to the left (see Fig. III.9d). The backflow of the jet gas in the vicinity of the contact discontinuity has a velocity of about 12 towards the left. It accelerates the almost only outward moving shocked external medium to velocities in excess of 7, which is about 30% of the jet velocity. Because of that motion, the KH instabilities in the head region of the jet are always small in this early phase. These moving KH instabilities act like a piston on the shocked external medium. They drive weak waves, 3 of which are seen

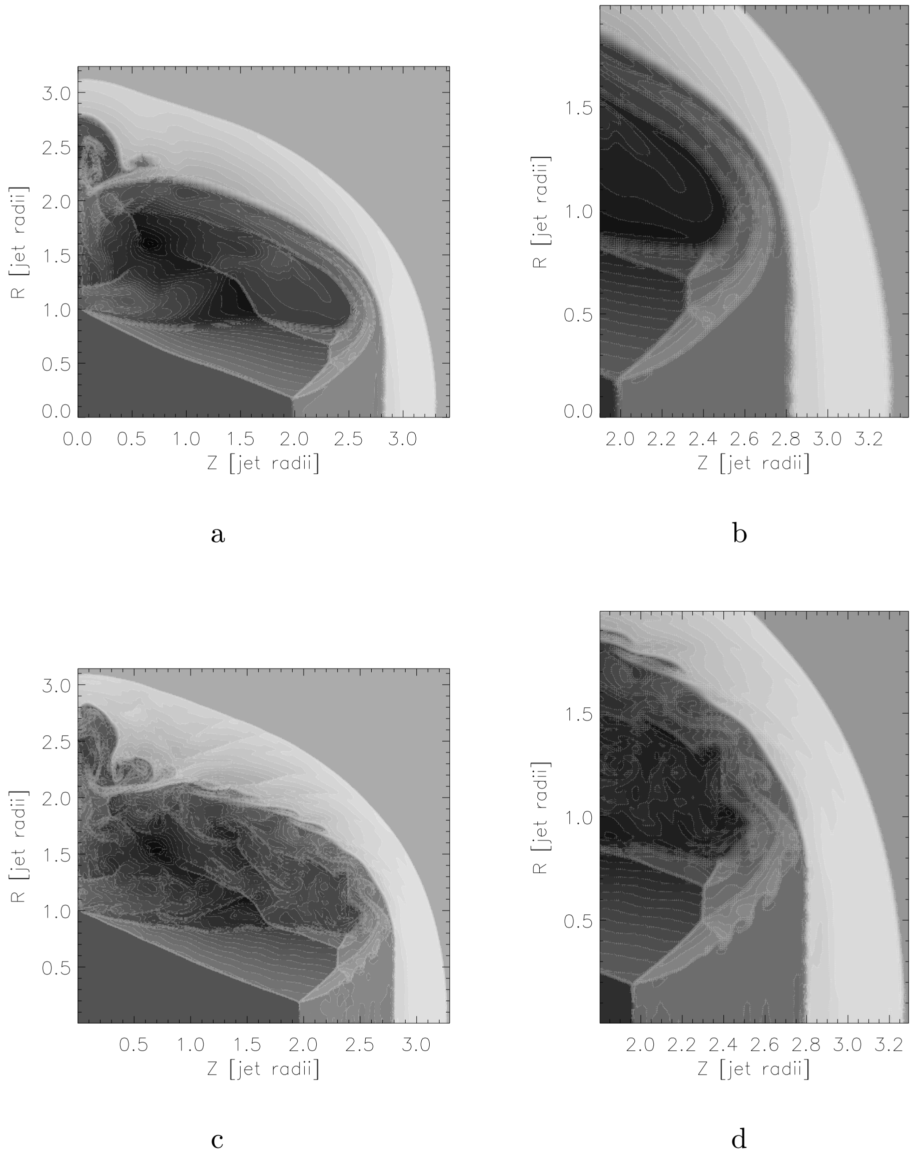

Figure III.4: *Gray scale plots of the logarithmic density for the jets of setup B. On the right hand side are magnifications of the head region of the corresponding picture to the left. The upper (a and b) and lower (c and d) pictures show the 100 ppb and 200 ppb simulations, respectively. The time is 0.500 in all cases.*

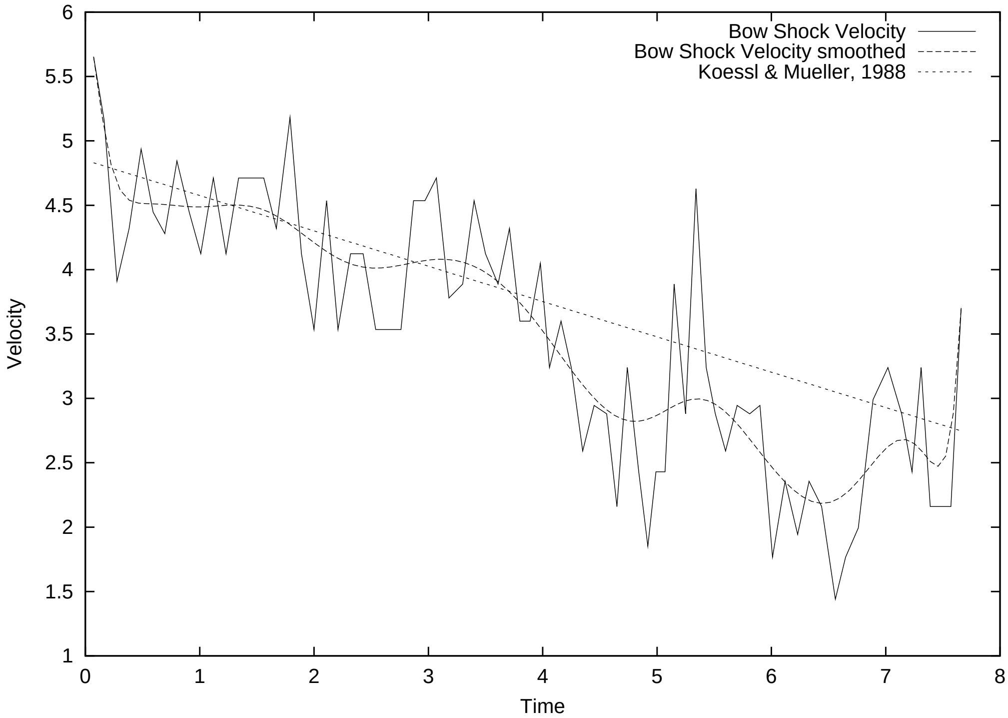

Figure III.5: *Bow shock velocity over time for the jet of setup A (solid line), smoothed (long dashed line) and for comparison the approximate behaviour in KM88 adopted from their figure 9a (short dashed line). 76 time steps were used for this graph.*

in the lower left plot of Fig. III.3. Indeed, their appearance can be best seen in the radial slices of the density and radial velocity (Fig. III.9a-c). The resolution comparison shows at 100 ppb in the region between $R \approx 2$ and $R \approx 2.7$ a nearly linear density increase. At 200 and 400 ppb the peaks of the discussed waves are clearly visible. Thus, it seems that the stream from the Mach disk triple shock point causes the KH instabilities at the contact discontinuity, which in turn drives weak waves into the shocked external medium. Small KH instabilities are also observed at the beam boundary, at highest resolution (Fig. III.3). They move towards the jet head. For example, the biggest bump in the lower plots of Fig. III.3 is located at $Z \approx 2$ in the left hand plot and at $Z \approx 3$ in the right hand plot. It depends on their velocity if they can be dangerous for the beam stability before they reach the jet head.

Rayleigh-Taylor instabilities at the jet head

The "beam pumping" (see above) gives rise to the onset of Rayleigh-Taylor (RT) instabilities near the axis in the contact discontinuity, which appear for the first time at a resolution of 100 ppb in the original publication, but can be clearly identified in the 70 ppb Nirvana contour plot ($(r, z) \approx (0.5, 7.5)$). Close examination of the jet head (Fig. III.3 ,III.4, and III.8) reveals that also the development of RT instabilities is crucially dependent on the resolution. The RT instability needs an accelerating jet, which only appears at a certain

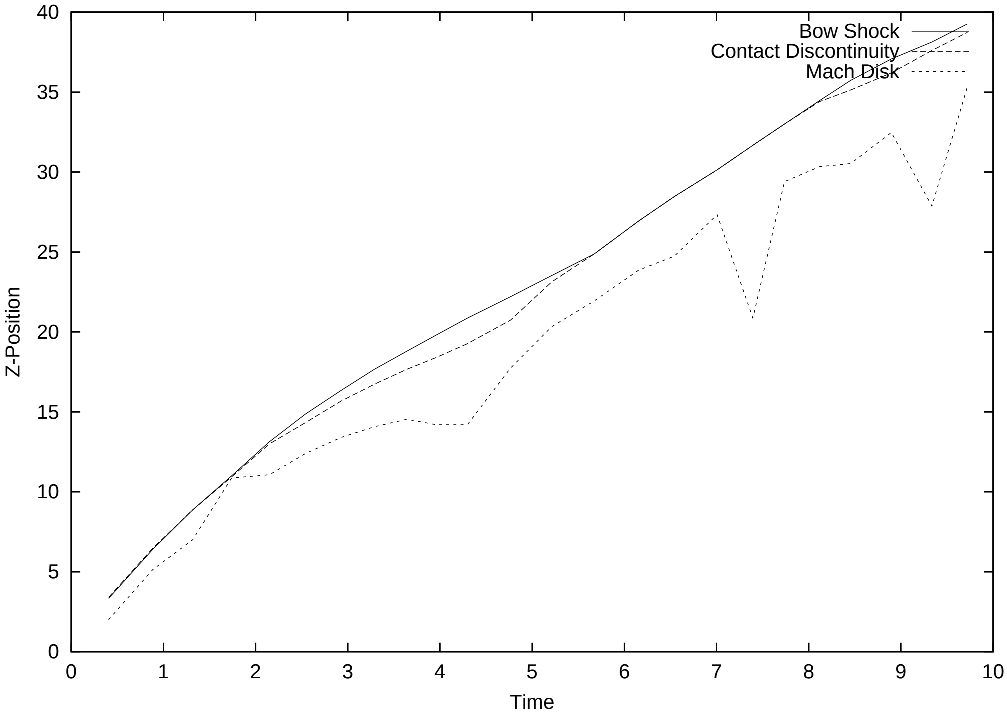

Figure III.6: *Flow parameters for the hydrodynamic jet model of setup C at 15 ppb with shock handling by artificial viscosity. The vertical axis displays the z-coordinate and the horizontal axis the time in the units used here, which is 1/15 of Lind's time unit. The highest z-value has always the bow shock, the contact discontinuity has a lower or equal z-value and the Mach disk takes the lowest value.*

resolution threshold connected to the appearance of oblique shocks in the jet, which are responsible for the acceleration. In order to investigate the mass entrainment into the jet head in more detail, the radial average of the density in the jet beam is shown in Fig. III.16. In the low resolution plots, the contact discontinuity is visible as a nearly vertical line joining the density in the beam at nearly 90 degree. At 70 ppb small peaks appear at the contact discontinuity. This is the first sign of the RT instability. At higher resolution the differences between five and eight jet radii become more pronounced. At 400 ppb, the density in the region between $R = 5$ and $R = 7.5$ exceeds the density in the 10 ppb simulation by 0.2, on average. This corresponds to an entrained mass of about $\rho_{\mathrm{m}} R_{\mathrm{J}}^3$.

Convergence of global quantities

Global quantities were computed for each simulation. Fig. III.12 shows that at every resolution the Nirvana jet is slower than its counterpart in the original publication by $\approx (4.5 \pm 2)\%$. If one uses with Nirvana a lower resolution by a factor of $2 - 2.5$ than the corresponding computation in the original publication, one gets the same average bow shock velocity. Fig. III.13 shows the convergence of four global quantities up to the highest resolution. The first

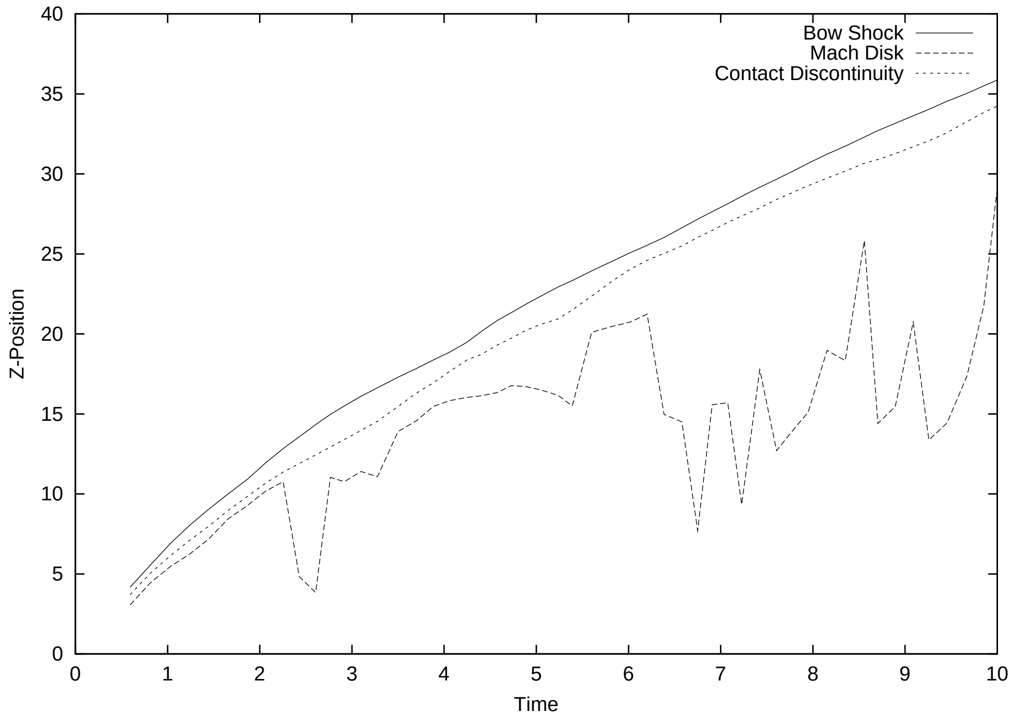

Figure III.7: *Same as Fig. III.6, but at a higher resolution of 30 ppb.*

two are the bow shock velocity averaged over the computation time and the total mass in the computational domain. These two parameters should be correlated because the bow shock sweeps the mass, which is concentrated in the ambient medium, off the grid. They converge at 100 ppb. This reflects the fact that the cocoon develops only additional small scale structure once the long wavelength instability has been sufficiently resolved. The behaviour changes at 400 ppb, where again more matter remains within the computational domain after a stagnation between 100 and 200 ppb. Axial momentum is mainly situated in the region between contact discontinuity and bow shock (shroud), the beam and the backflow (decreasing order). In all the simulations compared in Fig. III.13, the axial momentum changes by only 5% indicating that the global flow pattern is reproduced quite well already at low resolution. The internal energy is concentrated in the region behind the bow shock and in front of the Mach disk. This is why it is partly correlated to the axial momentum. But convergence of this number indicates also a correct description of the terminal shock region. As can be seen in Fig. III.3, the terminal shock region seems to behave quite differently in simulations with different resolution. Changes of the internal energy on the 5% level remain up to 200 ppb. The flat behaviour between 200 and 400 ppb might be due to coincidence.

Summarising, it seems that the simulation was well on its way to convergence up to 200 ppb. But the surprising damping of the long wavelength KH instability opened up a new chapter in the convergence behaviour.

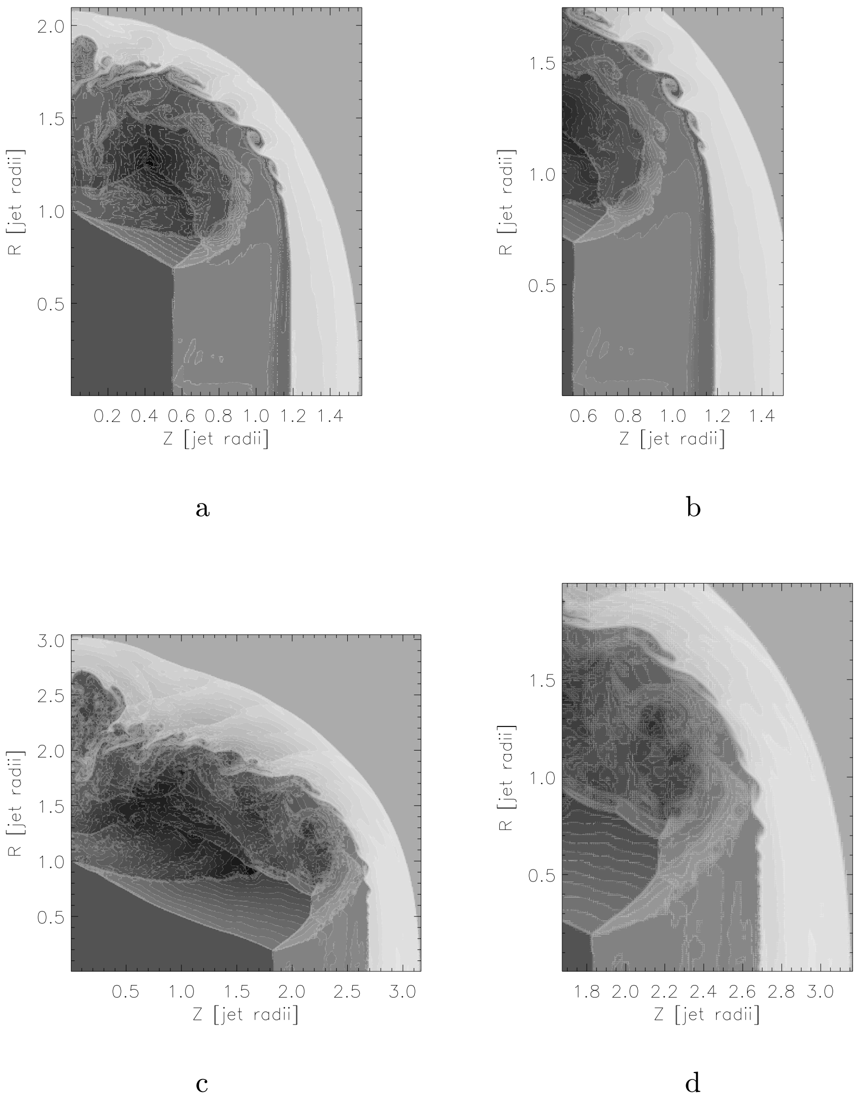

Figure III.8: *Same as III.4 but for 400 ppb and at times t=0.216 (upper pictures) and t=0.483 (lower pictures). (The data in this figure and in Fig. III.4 was rebinned to 100 ppb for visualisation.)*

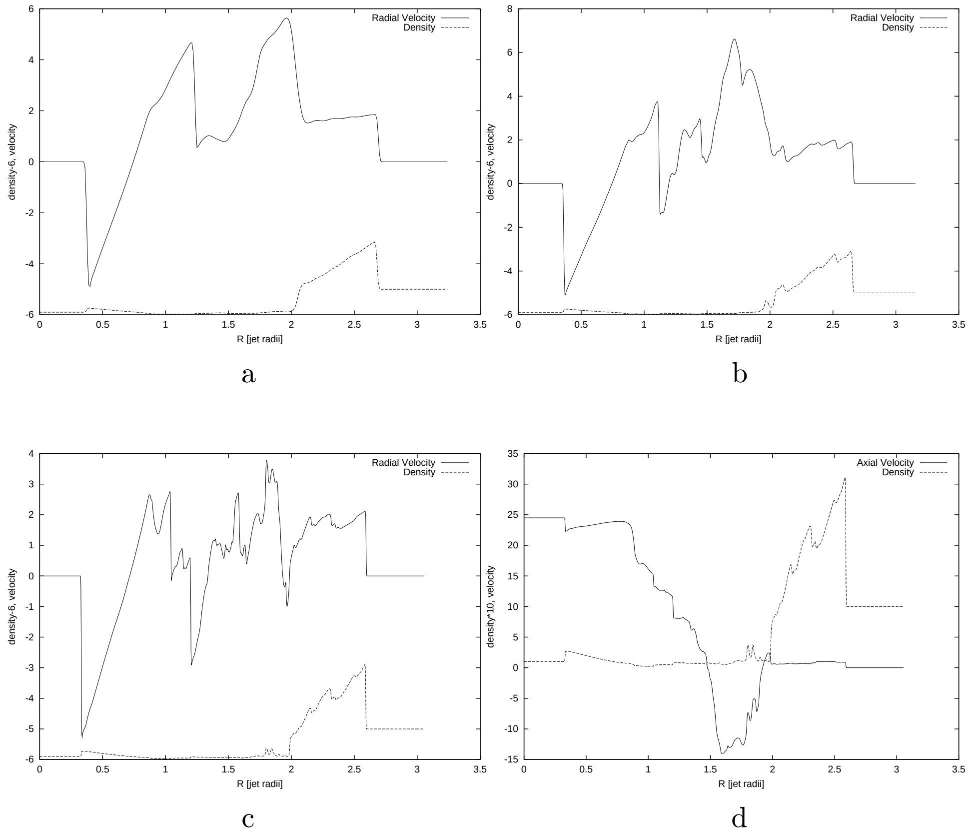

Figure III.9: **a-c:** *Slices at* $Z = 1.5$ *for radial velocity (solid) and density* (-6) *(dashed) over radius at time t=0.5 for setup B. The resolution is 100, 200, and 400 ppb for plot a to c, respectively. The shocked external medium is located between* $R = 2$ *and* $R = 2.7$. **d:** *Radial slice for density* $(\cdot 10)$ *and axial velocity at t=0.5, Z=1.5 for the 400 ppb simulation. At R=1.9 the fingers of the KH instabilities are visible (increase in the density). They also appear in the velocity as slower regions.*

III.3 Magnetohydrodynamic Jet Simulations

III.3.1 Configuration

The setup here is essentially the same as in setup C of the previous section except for a toroidal magnetic field (B_ϕ) and a jet pressure profile which assures initial transverse hydromagnetic equilibrium (see Lind et al. (1989) for details). The jet profile is:

$$B_\phi = \begin{cases} B_\mathrm{m}\, r/R_\mathrm{m} & , \quad 0 \le r < R_\mathrm{m} \\ B_\mathrm{m}\, R_\mathrm{m}/r & , \quad R_\mathrm{m} \le r < R_\mathrm{J} \\ 0 & , \quad R_\mathrm{J} \le r \end{cases} \tag{III.2}$$

and

$$p = \begin{cases} \left[\alpha + \frac{2}{\beta_{\rm m}}\left(1 - \frac{r^2}{R_{\rm m}^2}\right)\right] p_{\rm m} & , \quad 0 \le r < R_m \\ \alpha\, p_{\rm m} & , \quad R_{\rm m} \le r < R_{\rm J} \\ p_{\rm m} & , \quad R_{\rm J} \le r \end{cases} \tag{III.3}$$

where $R_{\rm m} = 0.37(R_{\rm J})$, $B_{\rm m} = 11.09$, $\alpha = 0.33$, and $\beta_{\rm m} = 0.205$. The average plasma $\bar{\beta}$ which gives the ratio of the mean internal gas pressure to mean internal magnetic pressure is defined as:

$$\bar{\beta} := \frac{\bar{p}}{\frac{1}{8\pi}\frac{2}{R_{\rm J}^2}\int_0^{R_{\rm J}} B_\phi^2(r')\, r'\, dr'} \tag{III.4}$$

and has the value of 0.6. The mean magneto-sonic Mach number,

$$\bar{M_{\rm J}} = v_{\rm J}\left(\frac{2}{R_{\rm J}^2}\int_0^{R_{\rm J}} (\gamma + B_\phi^2/(4\pi p))\frac{p}{\rho}\, r\prime\, dr\prime\right)^{-1/2} , \tag{III.5}$$

is 3.5. This corresponds to the highly magnetised jet model in Lind et al. (1989).

III.3.2 Comparison of results

Detailed contour plots of the MHD jet at the end of the simulation are given in Fig. III.10. At first sight, one recognises a great similarity to the corresponding picture in Lind et al. (1989). The same nearly stationary big terminal vortex forms which includes the Mach disk. Here the jet material is driven away from the axis out to about $r = 6$, where it is partly refocused onto the axis due to the Lorentz force, and another part manages to establish a backflow. This backflow turns again joining the main stream. As can be seen quite well in the sonic line plot the refocused material hits the z-axis at about $z = 13$. There it separates itself again, forming an on-axis backflow (which enhances the deflection from the axis and then joins the main stream) and a time dependent outflow from the region in the z-direction which leaves at $z \approx 15$. Due to the low pressure and the high magnetic field ($\beta \equiv 8\pi p/\mathbf{B}^2 \approx 10^{-2}$), this area was called *magnetically dominated cavity* by Lind et al. (1989). This is reproduced well in the resimulation. When the plasma leaves this cavity, it forms a so called *nose-cone* of about $4\,R_{\rm J}$ width, as it should be. This nose-cone ends at a contact discontinuity which can be seen in the plot of the toroidal magnetic field. At $t = 5.7$ (Fig. III.10) the bow shock has an average velocity of 6.27 which is about 3% slower than the corresponding jet in Lind et al. (1989). This might be due to the accuracy of the measurement which was carried out using an ordinary ruler for z-position of the bow shock in Lind's publication and dividing it by the simulation time. The advance of bow shock, Mach disk and contact discontinuity is shown in Fig. III.14 and is generally very similar to the corresponding picture in Lind et al. (1989). The exception is the position of the Mach disk, which has a considerably lower z-value in the Nirvana simulation. At $t \approx 5.7$ the Mach disk has reached $z \approx 5$ versus $z \approx 7$ in the original publication. The advance of the Mach disk seems to be coupled to the size

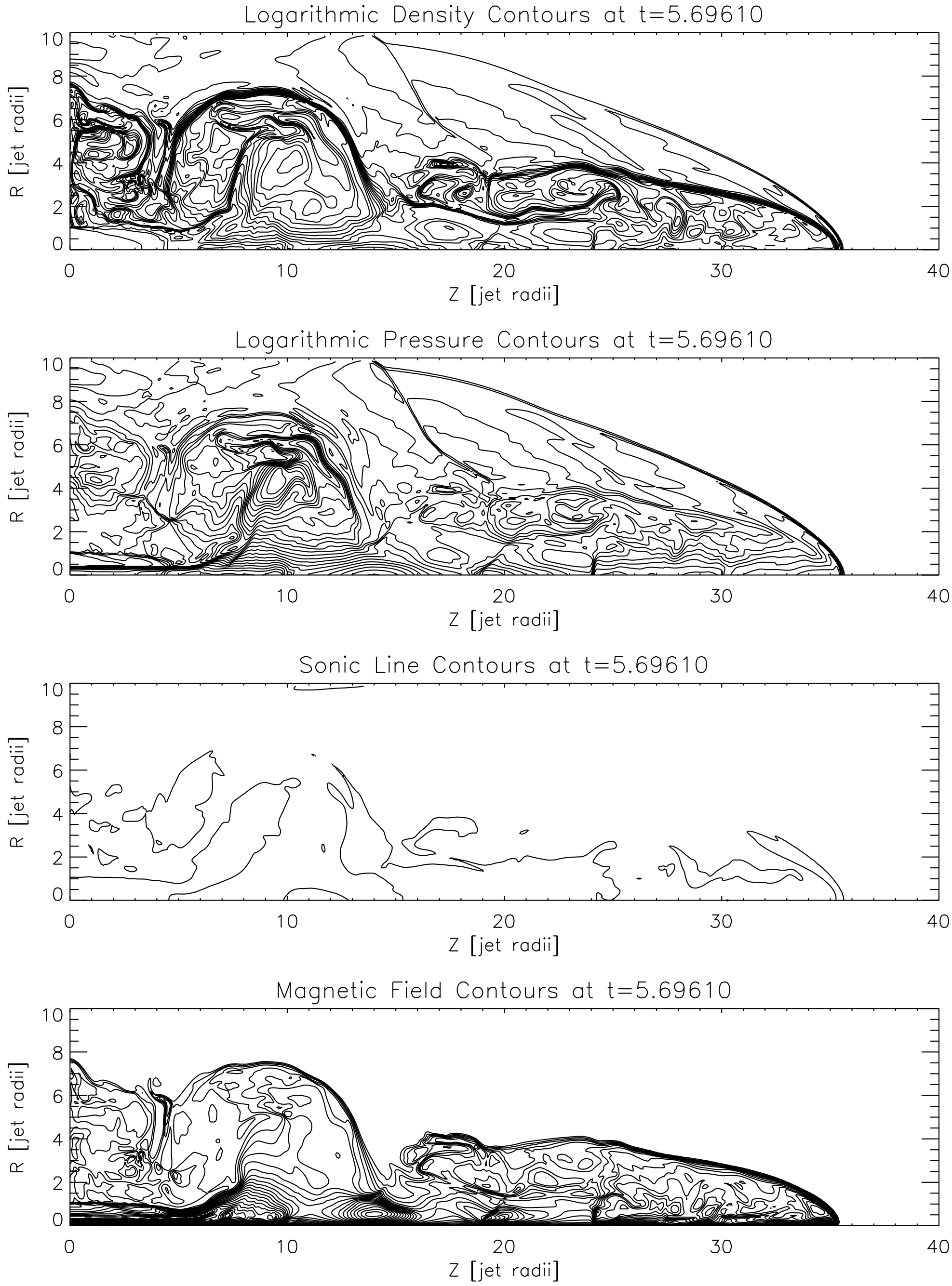

Figure III.10: *Contour plots of the density (30 logarithmically spaced lines), pressure (30 logarithmically spaced lines), magneto-sonic lines (magneto-sonic Mach number equals 1 or -1) and toroidal magnetic field (30 lines) of the highly magnetised jet model at timestep 13500. This corresponds to a simulation time of 5.70. In units of Lind et al. (1989) that would be 85.5.*

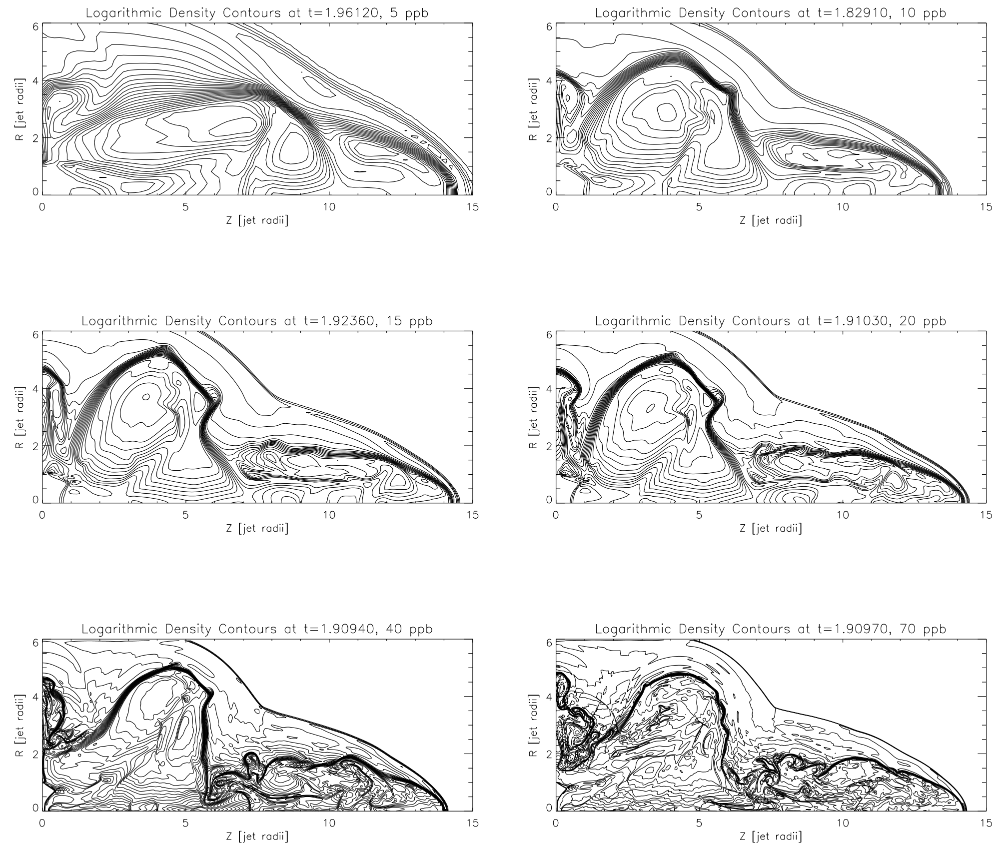

Figure III.11: *Snapshots of the logarithmic density contours of the MHD jet at different resolutions. Times of the snapshots and resolution are indicated on top of the figures.*

of the on-axis backflow described above. The amount of this on-axis backflow turns out to be sensible to the code used for the simulation: It is stronger in the resimulation and therefore the Mach disk moves slower. Gas and magnetic pressure close to the axis are plotted in Fig. III.15. One can see the close correlation of the magnetic pressure and the gas pressure. Directly on the axis the magnetic field vanishes because of axi-symmetry. Therefore the magnetic field is generally weak in vicinity to the jet axis. The plot confirms also the original publication: Behind the Mach disk the gas pressure rises up to 60 and in the nose-cone it is on average $25 - 30$. RT instabilities could not be found in the Nirvana computation. In contrast, one prominent KH instability develops at the upper right edge of the big vortex, probably excited by the jet stream that hits the contact discontinuity here. This was not observed in the original publication. The instability circled around the vortex and deposited an amount of jet plasma to the left of the vortex where one can see shocked ambient gas in the original publication. Other differences are the shock structures in the nose-cone. They are sharper in the original which one can trace back to the lower amount of diffusivity in shock regions by the FLOW code (compare also setup C of the hydrodynamic section).

III.3.3 Convergence

To investigate the convergence behaviour the simulation was repeated at lower and at higher resolutions (5 ppb, 10 ppb, 20 ppb, 40 ppb and 70 ppb). The results are shown in Fig. III.11. The time chosen for the snapshots was approximately 1.9. At that time the KH instability is excited as a bump at $(r, z) \approx (3.5, 6)$. Interestingly, this bump disappears at a resolution of 70 ppb like in the original publication. The behaviour of the internal structure of the nose-cone does not seem to converge. The Mach disk moves slower at higher resolution. It has advanced $\approx 0.2\, R_\mathrm{J}$ less at 20 ppb than at 15 ppb in Fig. III.11. At 70 ppb the Mach disk has reached the inflow boundary. Already at 40 ppb the shape of the contact discontinuity changes. This is probably due to the vicinity of the Mach disc to the inflow boundary. The retreat of the Mach disk is surprising. Given higher efficiency of FLOW, one should compare the 20 or 40 ppb simulation to the FLOW result. Therefore the two simulations seriously disagree on the propagation of the Mach disk, and it seems that Nirvana approaches convergence in a different way than FLOW, at least, if a dominant magnetic field is present. Nevertheless the overall shape of the bow shock and the contact surface remains essentially the same. Also the average bow shock velocity stays remarkably constant, 7.6 at 15 ppb and 7.5 at the others: It seems to be converged. With an eye on the lower resolution plots one could say that even 10 ppb are sufficient to catch the correct behaviour at the contact discontinuity and the bow shock. But there is a sharp transition to lower resolution. This tells us that the essential features dictating the shape of the bow shock and essentially also of the contact discontinuity are of the order 1/10 of a jet radius.

III.4 Discussion

Simulations of magnetised and unmagnetised astrophysical jets in 2D were performed. In the pure hydrodynamic simulations, it was shown by detailed examination of a time series which was compared to the simulation by Kössl and Müller (1988) and by a recomputation of the model of Lind et al. (1989) that in principle each of the evaluated codes is able to produce similar results. However they do not achieve this result with the same resolution: DKC needs more than twice the resolution to achieve similar results compared to Nirvana. Nirvana in turn needs somewhat more than twice the resolution in order to achieve the same results as FLOW. The results have revealed that depending on the exact method of shock handling the effective resolution of MHD codes – measured through the convergence of global variables and inspection of characteristic features in the contour plots by eye – differs considerably more than in the test calculations by Woodward and Colella (1984) – when applied to the jet propagation problem. If one looks at results produced by the codes at moderate resolution (20 - 40 ppb) one finds a characteristic representation of KH instabilities: they appear as breaks in the contact discontinuity in DKC, as round

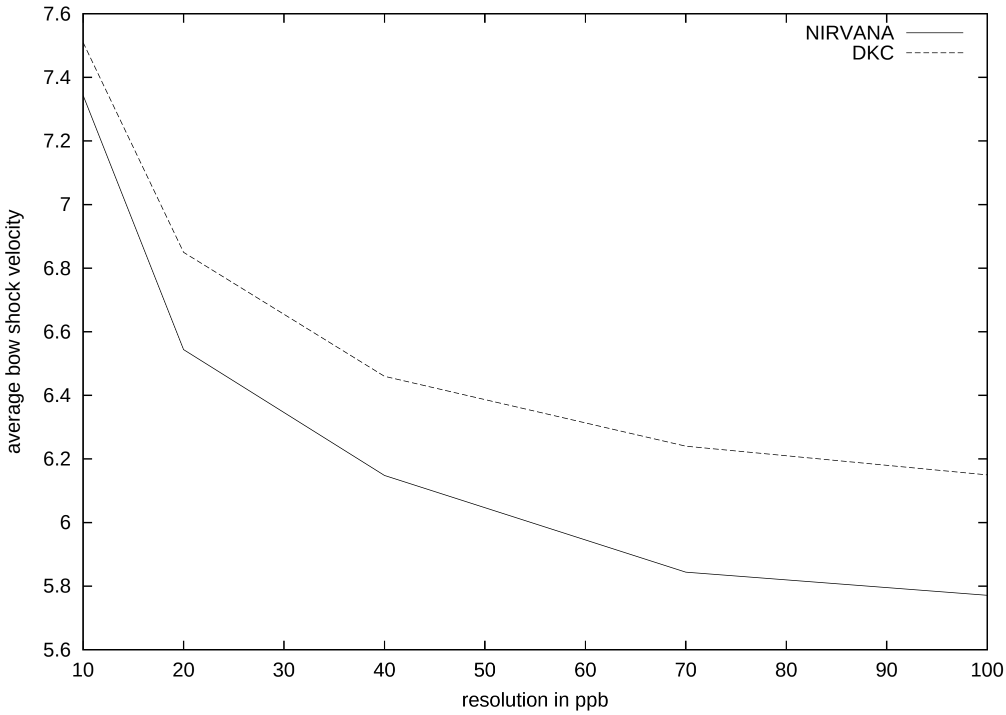

Figure III.12: *Comparison of the bow shock velocity of the setup B jets with the ones of equal snapshot time from Kössl and Müller (1988). The snapshot times were: 10 ppb: t=1.28, 20 ppb: t=1.41, 40 ppb: t=1.42, 70 ppb: t=1.99 and 100 ppb: t=1.98.*

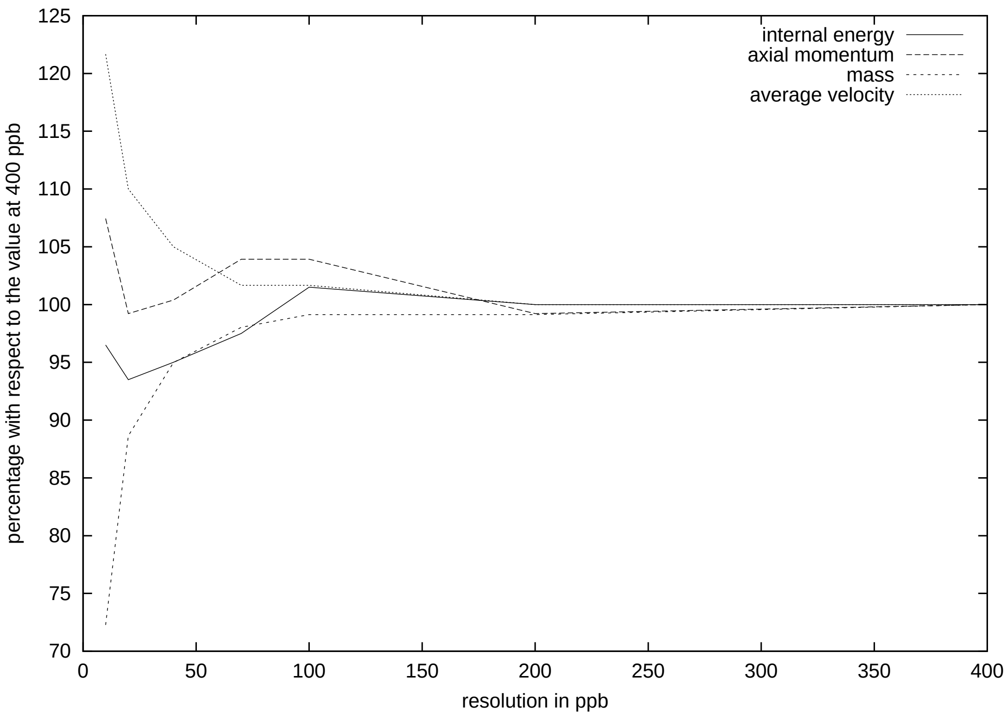

Figure III.13: *The total values of internal energy, axial momentum, mass and average bow shock velocity against resolution for the simulations from setup B at t=1.28 (t=1.27 for 70 ppb). At the resolution of 100 the mass is converged with an accuracy of 3 digits.*

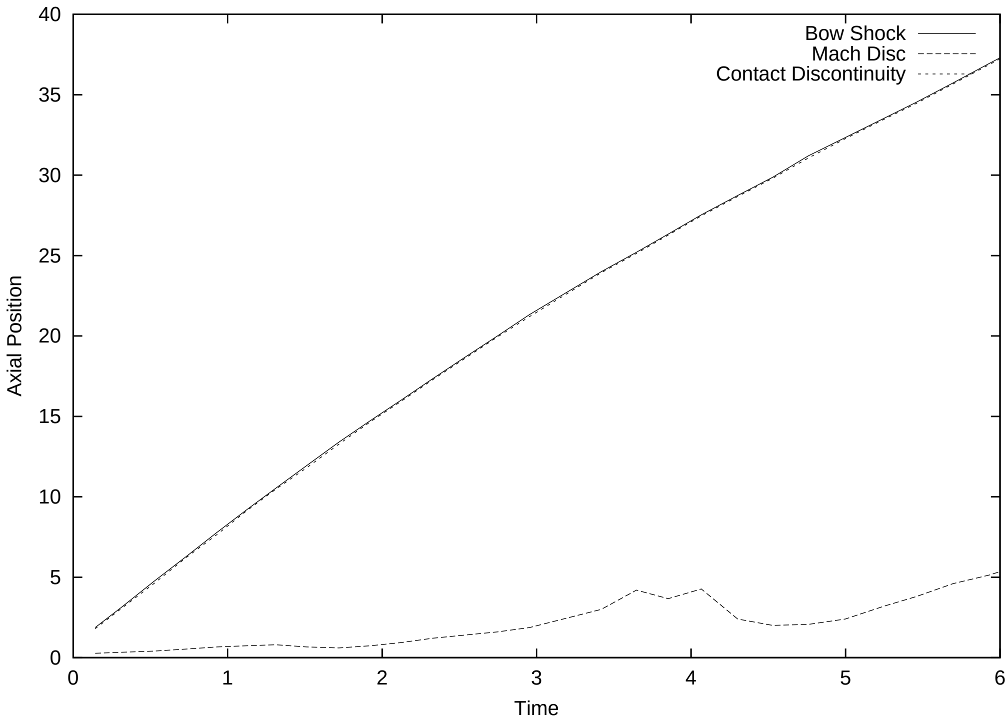

Figure III.14: *Time evolution of bow shock, Mach disk and contact discontinuity for the simulation of Fig. III.10. Notice that there is only a small difference between the positions of contact discontinuity and bow shock.*

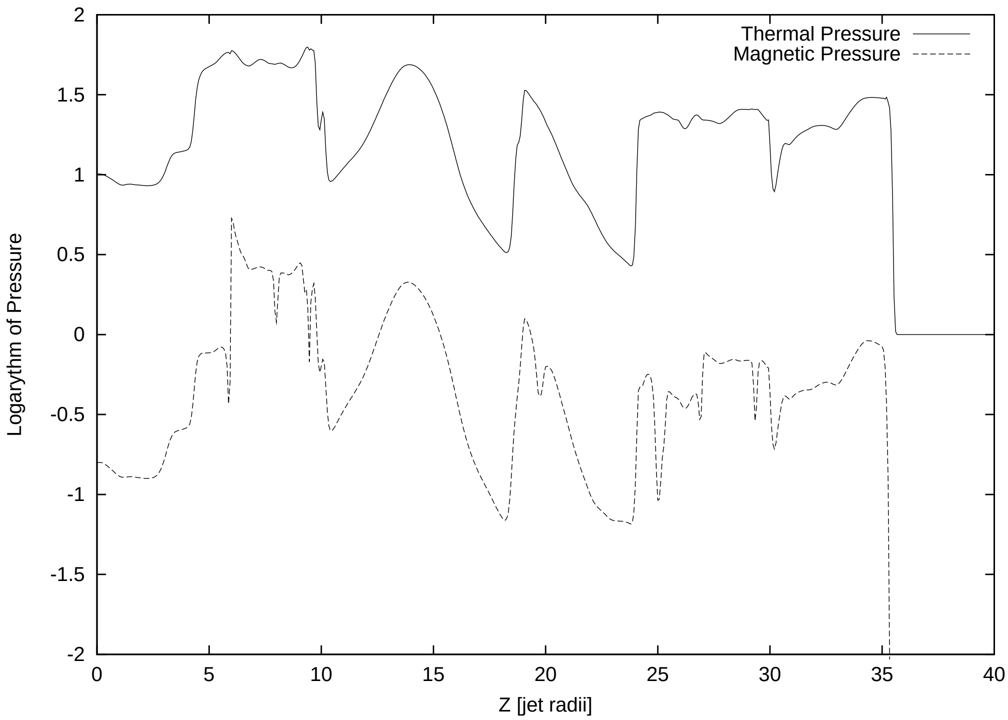

Figure III.15: *On axis ($r = 1/15$) gas and magnetic pressure for the simulation of Fig. III.10. The upper line displays the gas pressure and the lower one the magnetic pressure. Note the close relationship between them.*

structures in FLOW and as intermediate a little bit unregular but still round structures in Nirvana. While FLOW is quite an unusual code, because it needs no artificial viscosity, it turns out to be the most efficient code by far, at least, if no magnetic field is present. Strictly speaking, the results of FLOW cannot be reproduced with Nirvana. But the differences are explained by effects of resolution and artificial viscosity together. It was also shown that the resolution of the simulation influences the average bow shock velocity more in the non-laminar flow phase than in the laminar one. If one explains the differences between the codes with a resolution effect, as suggested here, it can be concluded that in the laminar phase the beam structure is indeed converged whereas in the non-laminar one it is not. The global jet parameters converge in HD simulations with Nirvana at ≈ 100 ppb. But even with the highest resolution computation (400 ppb) no fully converged beam structure is achieved: There are KH instable regions in the cocoon and a complicated terminal shock structure that seems to evolve in a turbulent manner. On the contrary, on the highest level of resolution qualitatively new behaviour arises: the long wavelength KH instabilities are damped by the onset of small-scale turbulence, which develops prior to the long wavelength modes, and the RT instability manages to entrain more and more mass into the jet's head with increasing resolution. In a real situation however, one can expect that KH instabilities at the contact discontinuity will arise because of inhomogeneities in the external medium or a not completely steady jet flow. The present computation shows that they arise, even with a homogeneous external medium and a steady jet flow.

Concerning the jet with a toroidal magnetic field, a good convergence behaviour was found up to 20 ppb: At 10 ppb, the shape of the bow shock and the contact discontinuity is essentially converged. The average bow shock velocity changes marginally up to 20 ppb. (It remains constant for higher resolution.) A big problem is the discovered movement of the Mach disk towards the inflow boundary. It tells us that this particular simulation does not converge, when computed with Nirvana. It would be interesting to check this result for different initial conditions. A better configuration for the jet with a toroidal magnetic field would probably be one with a time dependent injection like the outflow from the magnetically dominated cavity. Also, this is a disagreement between FLOW and Nirvana. A possible explanation could be that the efficiency derived in the hydrodynamic case can not be applied for MHD simulations, maybe, because the different diffusivity description puts Nirvana and FLOW on two different convergence branches. How the propagation of the Mach disk would change with resolution for the FLOW case remains unclear. Resolution studies with different codes are therefore desirable. It was shown that Nirvana produces results comparable to established codes when applied to the light jet problem, including the magnetised case, except the receding Mach disk problem. This could indicate that some magnetic field configurations cannot be studied with Nirvana, because of the lack of convergence. Alternatively, Nirvana is simply right. This could be checked by resimulations with different codes.

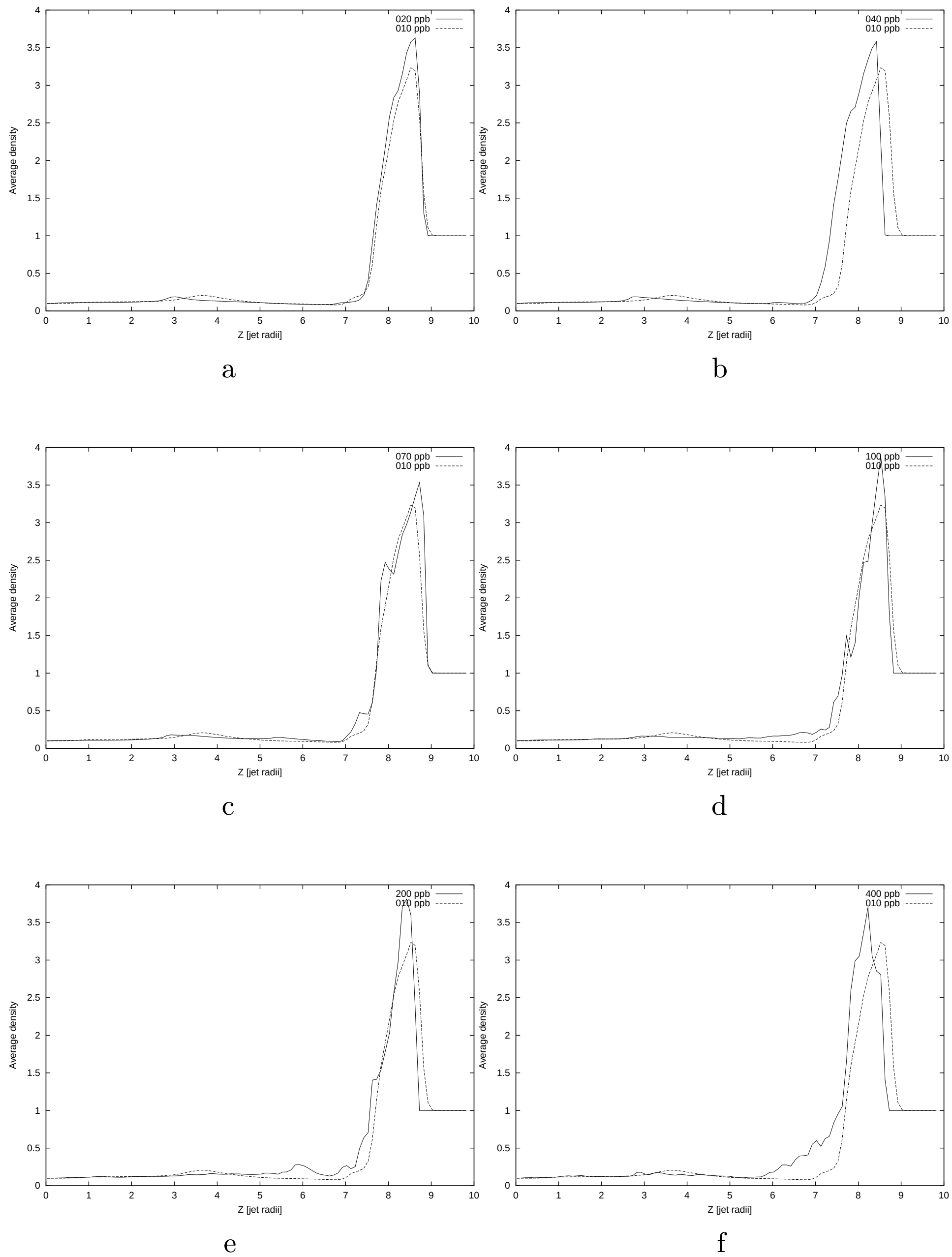

Figure III.16: *Density averaged over the beam radius for the simulations of setup B. Plots a to f apply to 20 ppb, 40 ppb, 70 ppb, 100 ppb, 200 ppb and 400 ppb, respectively. The mass entrainment into the jet head can be seen in plot f, between* $Z = 6$ *and* $Z = 7.5$. *For comparison, the 10 ppb curve is plotted as a dashed line in each figure.*

Chapter IV

The Parameter Space at Low Jet Density

IV.1 Constraints from Observations

In nearby radio galaxies, the movement of individual jet features can be observed in the inner ≈ 100 parsecs (e.g. Britzen et al., 2000). The measurements indicate apparent superluminal motion, which is a unique feature of relativistic velocities, very close to the speed of light c. The velocity at kpc scale is not so easy measurable. Carilli and Barthel (1996) cite a value of $v_{\mathrm{J}} \approx 0.4\,c$ for the jet velocity in the kpc scale jet of Cygnus A, estimated from the hot spot spectra and consistent with luminosity, minimum energy hotspot pressure, lack of internal Faraday dispersion in the lobes, and the jet-to-counterjet surface brightness ratio. However, it should be emphasised, that this number is quite uncertain.

Parma et al. (1999) measure the radio source lifetime by synchrotron aging. Their straight forward analysis yields a lifetime $t_{\mathrm{s}} < 100\,\mathrm{Ma}$ for low power sources and $t_{\mathrm{s}} < 10\,\mathrm{Ma}$ for high power ones. However, they point out that this discrepancy does not have to be real, since the estimate depends on the magnetic field, which is more uncertain in high power radio galaxies. Reducing the magnetic field to one forth of the applied equipartition value would push the high power sources to 100 Ma, also. This would be supported by jet-to-counterjet length asymmetry constraints (Scheuer, 1995), and just be consistent with the age of the universe in the case of extended sources at the highest redshifts. Since there is the possibility that the older populations of synchrotron electrons are polluted by reaccelerated ones or mixed with younger populations in backflow regions, synchrotron ages indicate lower limits. Adopting 100 Ma as fiducial upper limit for radio galaxy lifetimes, Parma et al. (1999) arrive at a typical head advance speed of $v_{\mathrm{head}} = (0.5 - 5.0)$ kpc/Ma for the low power sources. It is not unreasonable that the same parameters apply for high power ones. For those, Scheuer (1995) gives an upper limit of $v_{\mathrm{head}} = 30$ kpc/Ma, from jet-to-counterjet length asymmetry measurements.

Jet radii (R_j) are of the order of kpc (e.g. Carilli and Barthel, 1996). From the total radio luminosities, one can estimate the total kinetic jet luminosity. Since the source needs at least the energy to inflate the radio lobes, the total power has to be at least about twice the radio power (for Cygnus A, Carilli and Barthel, 1996), probably more. The most powerful sources at high redshift should therefore have $L_\mathrm{kin} = 10^{46-47}$ erg/sec.

For HZRG, where good X-ray data is still lacking, one of the more difficult things is the estimate of environmental density. Pressure balance gives densities of $n_\mathrm{ext} \approx 0.1\,\mathrm{cm}^{-3}$ for the radio galaxy 1243+036 (=4C 03.24) at $z = 3.6$, assuming a hot $T = 10^7$ K intracluster medium. A detailed model for the radio galaxy 4C 41.17 at $z = 3.8$ by Bicknell et al. (2000), including shock excited emission lines, infered up to $n_\mathrm{ext} = 10\,\mathrm{cm}^{-3}$.

Approximating equation (I.2) by $v_\mathrm{head} = \sqrt{\eta\epsilon}\, v_\mathrm{j}$ and using the nonrelativistic formula for the kinetic jet luminosity

$$L_\mathrm{kin} = \pi R_\mathrm{j}^2 m_\mathrm{p} n_\mathrm{j} v_\mathrm{j}^3, \tag{IV.1}$$

one calculates the jet density to:

$$n_\mathrm{j} = 10^{-6} \left(\frac{1}{\epsilon}\right)^3 \left(\frac{R_\mathrm{j}}{\mathrm{kpc}}\right)^4 \left(\frac{10^{46}\,\mathrm{erg/s}}{L_\mathrm{kin}}\right)^2 \left(\frac{n_\mathrm{ext}}{\mathrm{cm}^{-3}}\right)^3 \left(\frac{v_\mathrm{head}}{\mathrm{kpc/Ma}}\right)^6 \mathrm{cm}^{-3}. \tag{IV.2}$$

The high powers involved, the uncertainties in the measurements, and the differences from source to source make an observational estimate of the jet density quite difficult. Nevertheless, the head advance speed used in (IV.2) could be regarded more like a lower limit (see above). Since it has the highest power, one can use $n_\mathrm{j} = 5 \times 10^{-6}\,\mathrm{cm}^{-3}$ as an approximate lower limit. This limits the density contrast formally to $5 \times 10^{-7} < \eta < 10$. η is even more constrained by the fact that radio lobes develop, and that v_head should not be much below 1 kpc/Ma:

$$10^{-5} < \eta < 1. \tag{IV.3}$$

Now one can estimate the jet velocity:

$$v_\mathrm{j} = 100 \left(\frac{10^{-4}}{\eta}\right)^{1/2} \left(\frac{1}{\epsilon}\right)^{1/2} \left(\frac{v_\mathrm{head}}{\mathrm{kpc/Ma}}\right) \mathrm{kpc/Ma}. \tag{IV.4}$$

Using the above parameter ranges, one arrives at:

$$1\,\mathrm{kpc/Ma} < v_\mathrm{j} < 300\,\mathrm{kpc/Ma}. \tag{IV.5}$$

IV.2 Simulation Study of the Parameter Space

So far, jet simulations have been performed mainly with $\eta \geq 10^{-2}$. This was justified by estimates from nearby sources and, even more important, the available computational power. Especially the latter has changed over the years, and a scan of the full parameter space is now possible.

IV.2.1 Setup

For a first scan of the parameter space 24 axisymmetric hydrodynamic simulations were performed. The jets were ejected in pressure equilibrium into a homogeneous external medium. Other parameters are given in Table IV.1. Since a relativistic code was not available, the jet velocity was restricted to the

Table IV.1: Simulation parameters

η	v_{j} [kpc/Ma]	M_{int}	M_{ext}
10^{-2}	95	808.3	8083
10^{-2}	31	255.6	2556
10^{-2}	9.5	80.83	808.3
10^{-2}	3.1	25.56	255.6
10^{-2}	0.95	8.083	80.83
10^{-2}	0.31	2.556	25.56
10^{-3}	95	255.6	8083
10^{-3}	31	80.83	2556
10^{-3}	9.5	25,56	808.3
10^{-3}	3.1	8.083	255.6
10^{-3}	0.95	2.556	80.83
10^{-3}	0.31	0.8083	25.56
10^{-4}	95	80.83	8083
10^{-4}	31	25.56	2556
10^{-4}	9.5	8.083	808.3
10^{-4}	3.1	2.556	255.6
10^{-4}	0.95	0.8083	80.83
10^{-4}	0.31	0.2556	25.56
10^{-5}	95	25.56	8083
10^{-5}	31	8.083	2556
10^{-5}	9.5	2.556	808.3
10^{-5}	3.1	0.8083	255.6
10^{-5}	0.95	0.2556	80.83
10^{-5}	0.31	0.08083	25.56

mildly relativistic regime. Also, relativistic simulations require more computer power, which may be critical at present.

The hydrodynamic simulations are fully determined by the internal Mach number M_{int}, the density ratio η, and the pressure ratio, which is unity. Hence, they are scalable to the parameter range needed in a specific source. Table IV.1 gives Mach number (M), density contrast (η), and the scaled velocity for a density of $n_{\mathrm{ext}} = 2\,\mathrm{cm}^{-3}$ and a temperature of $T_{\mathrm{ext}} = 5 \times 10^3$ K in the external medium, which was applied in the simulations. [1] The jet radius was set to

[1] All gas is assumed to be ionised. In reality gas is not ionised at that temperature. The

$R_\mathrm{j} = 1\,\mathrm{kpc}$. The grid covered an area of $Z \times R = 30 \times 30\,\mathrm{kpc}^2$ and the jet was resolved with 20 ppb. Boundary conditions were set to axial symmetry on the axis, reflecting on the left-hand side, and open on the other sides. The simulation was stopped when one of the following events happened:

1. The jet propagated to the right-hand side of the grid.
2. The computation time exceeded a reasonable amount without promising new behaviour in the near future. Typically, this time was several weeks.
3. The jet stopped at the nozzle, producing a shock at the inlet which ignored the shock jump conditions. This was caused by entrained material from the shocked external medium approaching the nozzle.

IV.2.2 Results

Cocoons

Coloured contour plots of the final timestep for each simulation are shown in Fig. IV.1. As expected from higher η simulations, the cocoons broaden with lower η. Also, a higher Mach number results in a cocoon more remote from the axis. At $\eta = 10^{-2}$, the cocoon detaches slightly from the beam, allowing the shocked external material, which crawls along the left-hand boundary, to move in between. Between $\eta = 10^{-2}$ and $\eta = 10^{-3}$, the cocoon undergoes a transition. Sometimes, the vortices it dissolves in are stringed in a line around the beam, but sometimes they join together forming a big vortex which extends approximately over the same size as the jet. This big turning vortex is especially prominent in the animation of the $(M, \eta) = (81, 10^{-4})$ simulation. Figure IV.1 $(M, \eta) = (81, 10^{-3})$ shows a new vortex just before being swallowed by the big one. The interface between cocoon and shocked external medium suffers from KH instabilities in a very similar way as the 400 ppb simulation in chapter III (compare Fig. III.8). The instabilities start at small size in the vicinity of the jet head. As they grow, extending their fingers into the cocoon, the backflow accelerates them towards the center. On the left-hand boundary, the fingers can get long enough to interact with the beam directly. In some cases, this caused a strong shock at the jet inflow, efficiently pushing the jet out of the computational domain (one of the reasons, why the simulation had to be stopped, see above). The $(M, \eta) = (81, 10^{-2})$ simulation in Fig. IV.1 shows a special behaviour: The left half of the cocoon is in a detached state, whereas the part next to the head huddles against the beam. Another extreme case are the six subsonic simulations in the lower right corner. Here the jet beam has almost disappeared, producing mainly a region of turbulent plasma rapidly mixing with its environment.

corresponding values for neutral gas, providing the same pressure, would be $n_\mathrm{ext} = 1\,\mathrm{cm}^{-3}$ and $T_\mathrm{ext} = 10^4$ K.

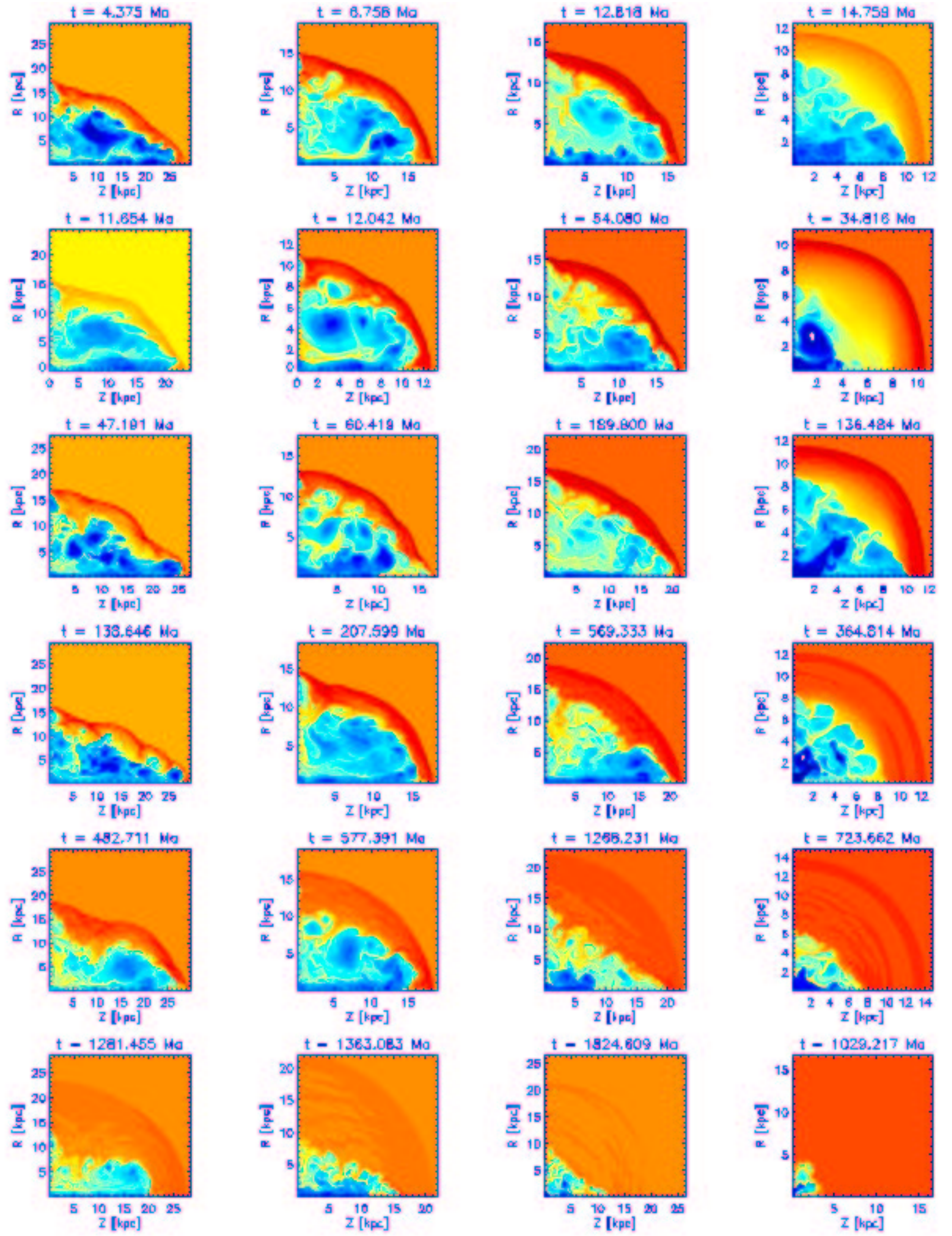

Figure IV.1: *Overview over the 24 simulations performed in order to scan the parameter space. The scaled velocity varies from 95 kpc/Ma (top row) to 0.31 kpc/Ma (bottom row). The Mach number (M) is constant on diagonals towards the top right. Density contrast ranges from* 10^{-2} *(left) to* 10^{-5} *(right). The logarithmic density contours vary from dark blue (low) to red (high).*

Bow shocks

The bow shocks in the presented simulations are quite different from one another and from simulations with higher η. Morphologically, they can be classified in four groups. The extremes are located in the four corners of Fig. IV.1. The jet in the upper left corner $(M, \eta) = (808, 10^{-2})$ shows an elongated bow shock, comparable to the simulation of Loken et al. (1992). Due to the high Mach number, the compression ratio is four over the whole surface of the bow shock. Reducing the Mach number to $(M, \eta) = (2.6, 10^{-2})$, lower left corner), the bow shock gets very regular. Evidently, this is caused by the lag of the contact discontinuity behind the bow shock. Even though there are some disturbances in the shocked external medium, they are not fast enough to catch the leading edge. The bow shock is still stronger in the direction of the jet propagation which produces a higher compression ratio near the head. The jet gets subsonic for the six simulations in the lower right corner. Therefore, no bow shock develops. Instead spherical sound waves are visible. In the remaining upper right corner $(M, \eta) = (26, 10^{-5})$, the sound wave has again steepened into a shock. This bow shock is now spherical. Applying equation (I.2) to these parameters gives a head propagation velocity of: $v_{\mathrm{head}} = v_{\mathrm{jet}}/316$, whereas the sound speed is $c_{\mathrm{s}} = v_{\mathrm{jet}}/26$, which is twelve times the head propagation velocity! One should therefore clearly expect a sound wave in front of this jet. So, what is it? A hint comes from the pressure versus number density (pn) histogram (Fig. IV.2). From their start position at pressure $p = 1.38 \times 10^{-12}$ dyn/cm^{-2}, and a density of $1\,\mathrm{cm}^{-3}$ and $10^{-5}\,\mathrm{cm}^{-3}$, respectively, the fluid elements move upwards to a thin line of constant pressure. The pressure equilibrium of all the fluid parts affected by the jet can be understood, if one considers that the sound speed in the jet ($\approx v_{\mathrm{jet}}/2$) is much higher than the propagation speed. The internal energy within the bubble of the bow shock is sufficient to drive a blastwave. The solution for the blastwave is derived in appendix A. In this limit the jet propagates slowly, and mainly transforms its constantly provided kinetic energy into heat. The resulting pressure drives the spherical blastwave. The velocity of the blastwave is proportional to $t^{-2/5}$. Hence, the blastwave is faster than the jet bow shock at early times, and slower later on. Using equation (A.12) and the radius of the blastwave bubble from the $(M, \eta) = (26, 10^{-5})$ simulation in Fig. IV.1 (≈ 11.5 kpc), one can derive a maximum ϵ of 0.7. This would correspond to a working surface with a radius of at least 1.2 kpc at the jet head. The density contours do not contradict to that, although the jet is in a quite complicated phase at the time shown in Fig. IV.1. One shock in the middle of the jet just became so strong that it developed a backflow there. The old jet head at $Z \approx 9$ kpc is dissolving. This is a short phase, and because the blastwave swept much of the matter away, the new jet will soon reach the position of the old one. One can understand the bow shock shapes of the other simulations as combinations of the four extreme ones, located in the corners of Fig. IV.1.

The final and average propagation velocity of the foremost entity of each simulation, which could be a bow shock, a sound wave or a blastwave, is shown in Table IV.2. Only some of the $\eta = 10^{-2}$ jets show mild acceleration, which can be explained by the usual beam pumping (compare page 29). Most of the other jets show deceleration, witnessing the fast blastwave phase, which is still undisturbed in the supersonic $\eta = 10^{-5}$ jets. The sound waves should travel with $c_{\mathrm{s}} = 0.012$ kpc/Ma. The high velocity in Table IV.2 is caused by a numeri-

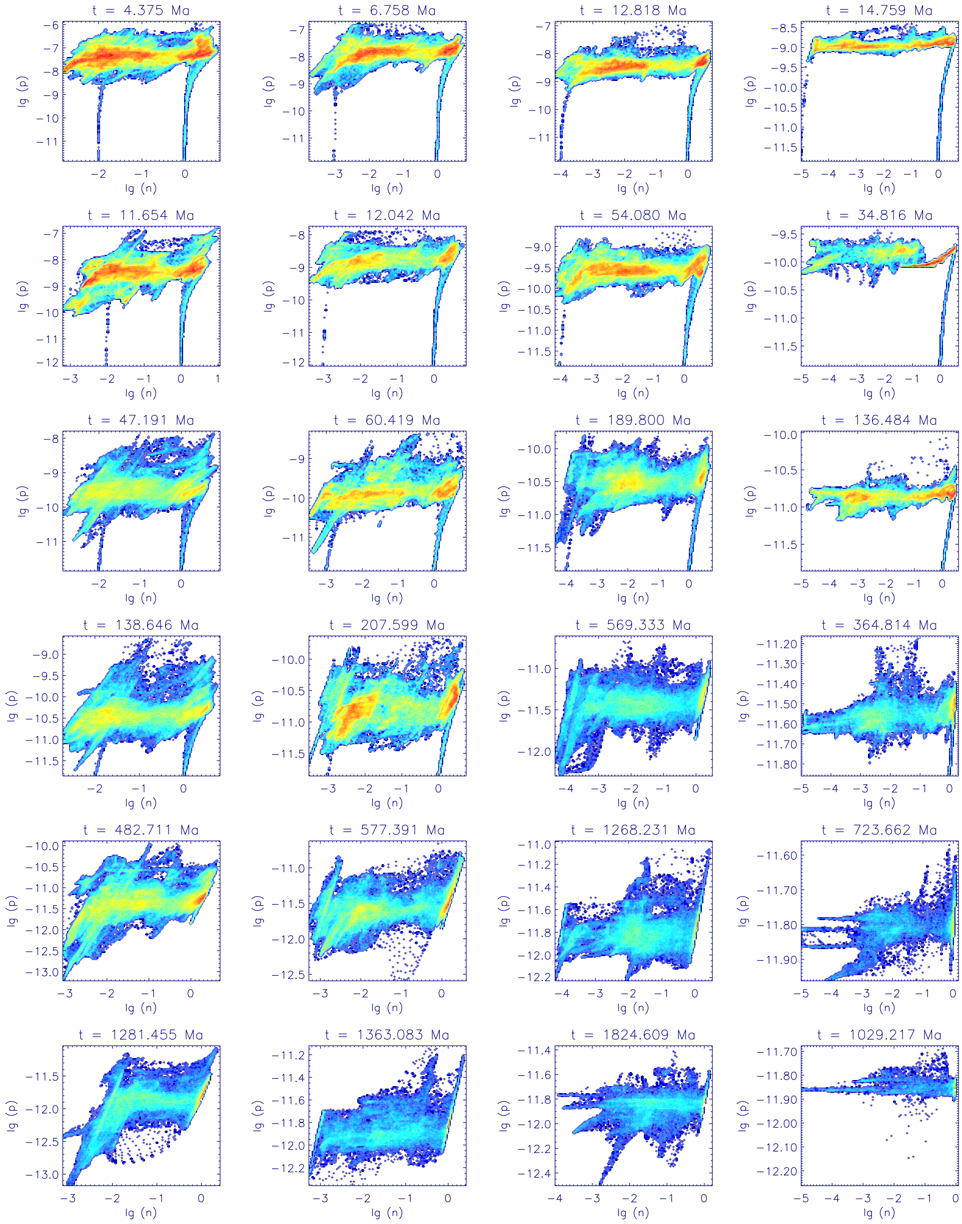

Figure IV.2: *Pressure over number density (pn) histograms. 100 bins were used on each axis. Pressure, number density, and counts are given in logarithmic units.*

cal artefact: In order to initiate the simulation, one has to provide a propagating jet at the nozzle. This rectangular area has quite a high kinetic energy, which produces the blastwave also at early times in the subsonic simulations, thereby increasing their average propagation velocity, artificially.

Using this propagation velocity (v_{prop}), one can define a propagation efficiency (ν), analogously to Norman et al. (1983):

$$\nu = v_{\mathrm{prop}} / \frac{\sqrt{\eta} v_{\mathrm{j}}}{1 + \sqrt{\eta}}$$

Table IV.2: Final and average propagation velocity

$\mathbf{v}_\mathrm{j}$	$-\log\eta$			
[kpc/Ma]	2	3	4	5
95	7.681/6.598	1.930/2.816	0.833/1.313	0.400/0.804
31	1.814/2.043	0.722/1.066	0.278/0.342	0.103/0.307
9.5	0.711/0.568	0.160/0.281	0.050/0.114	0.033/0.088
3.1	0.220/0.209	0.068/0.086	0.025/0.038	0.019/0.035
0.95	0.054/0.061	0.032/0.032	0.013/0.018	0.014/0.021
0.31	0.017/0.062	0.014/0.016	0.011/0.015	0.013/0.017

Final and average propagation efficiency are displayed in Fig. IV.3. The most efficient propagator is, of course, the sound wave, since its speed is constant, and the jet velocity can be arbitrarily reduced. The high efficiency in the low η simulations is readily explained by the high propagation efficiency of the blastwave, which still dominates at the time shown. Their final propagation efficiency has fallen below one (besides the $\eta = 10^{-5}$ simulation), indicating, in agreement with the density plots that the jet begins to shape the bow shock. In the following, the foremost shock will be called *bow shock* also if its actually the blastwave shock.

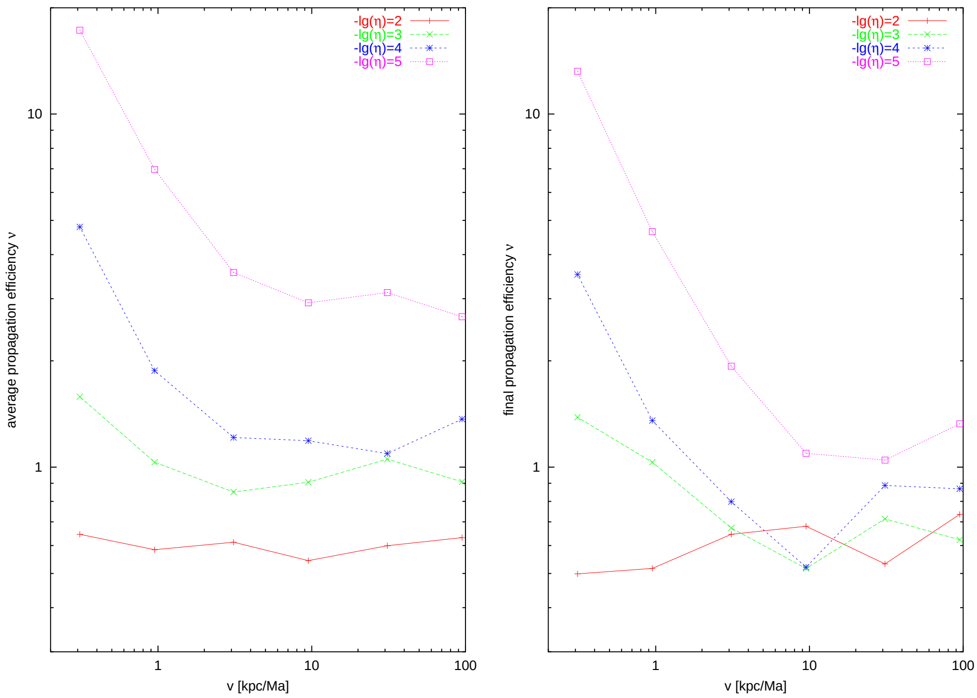

Figure IV.3: *Propagation efficiency defined as* $\nu = v_\mathrm{prop}/\frac{\sqrt{\eta}v_\mathrm{j}}{1+\sqrt{\eta}}$*, where* v_prop *is the average propagation velocity in the left panel and the final propagation velocity (averaged over the last 5% of the simulation time, approximately) in the right one.*

The broadening of the bow shocks can be characterised by the aspect ratio (Fig. IV.4), defined by the position where the bow shock hits the Z-axis divided by the position of the bow shock on the R-axis. Apart from the subsonic jets, where the cocoon is surrounded with the spherical sound wave, the aspect depends only weakly on the velocity of the jets.

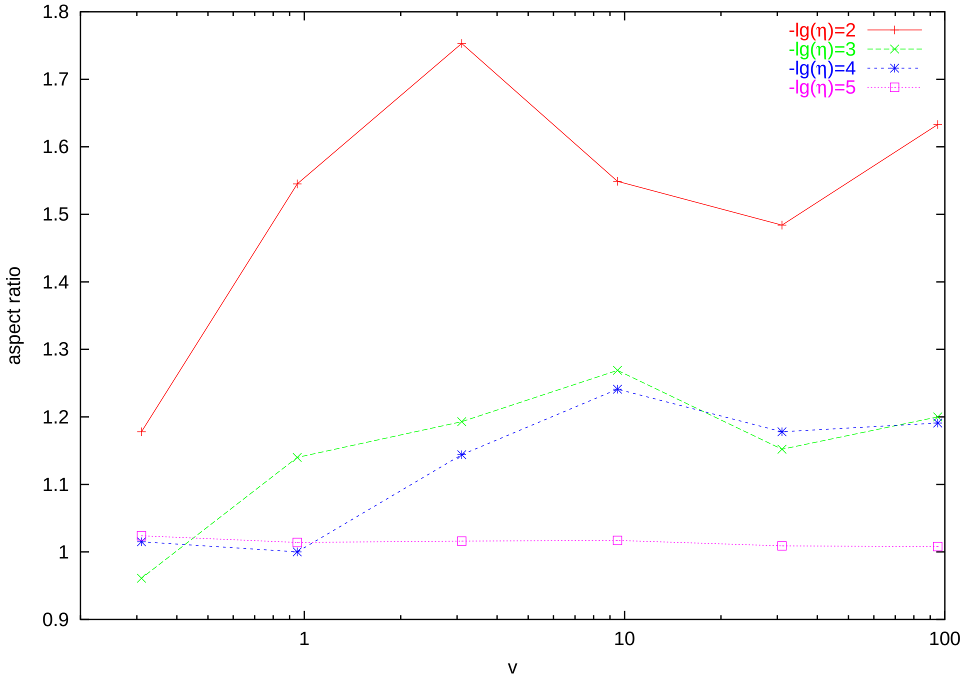

Figure IV.4: *Aspect ratio of the bow shock. The horizontal axis denotes the scaled velocity from Table IV.1*

Beams

In general, the beams are badly modeled in these simulations, because important physics is missing in the code (compare chapter I). However the hydrodynamics provides a first level of understanding of what is going on there in general.

High Mach numbers ($M > 3$) can be sustained for the $\eta = 10^{-2}$ jets (compare Fig. IV.5). With the exception of the $(M, \eta) = (26, 10^{-3})$ jet, all the other beams struggle around $M = 1 - 2$. Quite often they become subsonic, even if they start with high Mach numbers. Strong shocks decelerate those jets. Since also the cocoon detaches, nothing prevents the beams from being disrupted by the KH instability. A fine example is the $(M, \eta) = (26, 10^{-3})$ simulation (Fig. IV.1). The shocks in the beams sometimes get strong enough to shed vortices and produce backflows, thereby establishing a new jet head. The $\eta = 10^{-5}$ jets suffer from the short evolution time. At the time shown, the jets still have the prominent shock at the jet inlet, which was used as initial

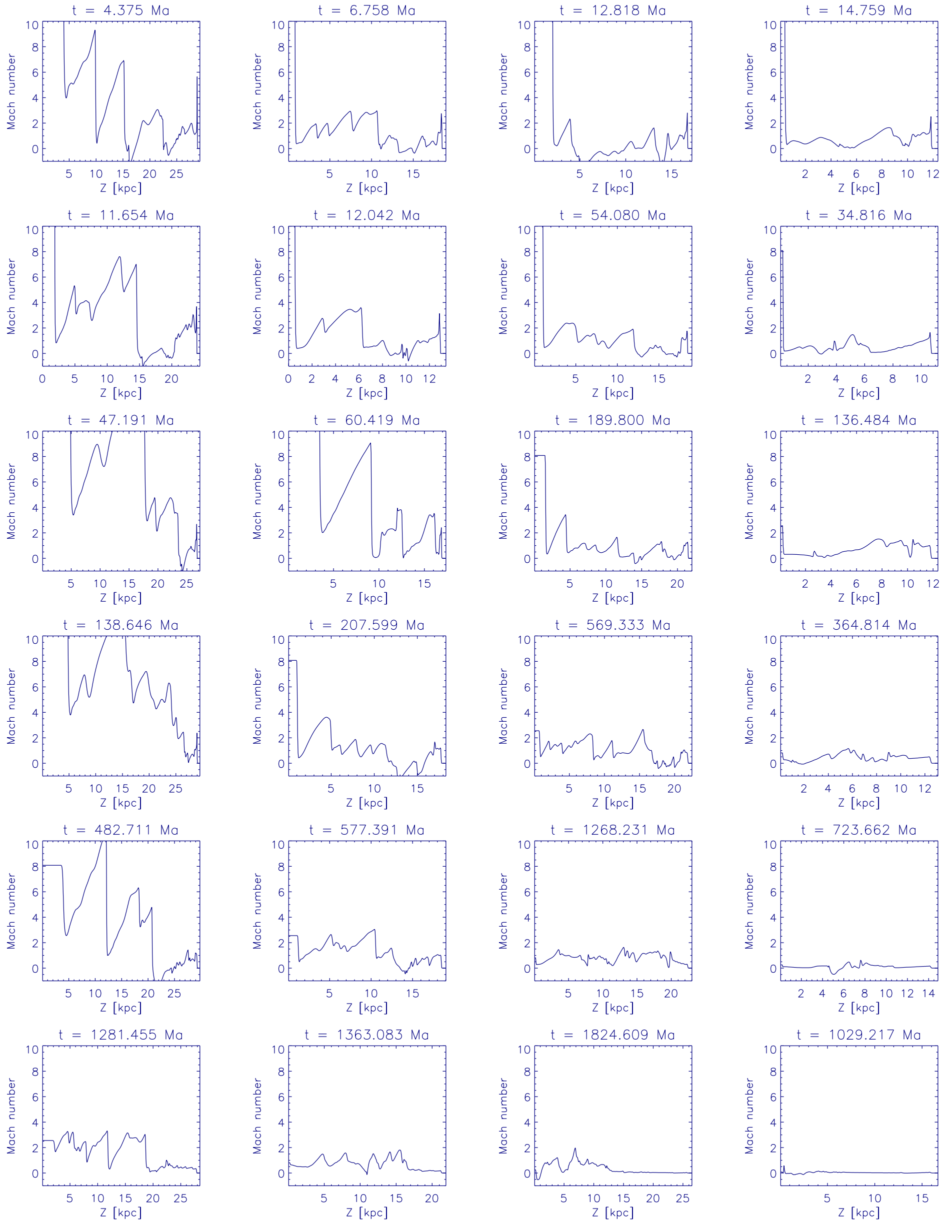

Figure IV.5: *On axis Mach number.*

condition. Since those are the computationally most expensive simulations, the problem can only be solved with a faster computer, evolving the jets longer.

Pressure versus number density histograms

From Fig. IV.2, it is evident that low η jets provide their own pressure everywhere. External medium as well as jet plasma get strongly shocked, and the high sound speed equalises the pressure within most of the jet bubble, especially in the higher Mach number cases. The external pressure is therefore unimportant, and the pressure matching, used as initial condition, can be dropped in future simulations, without much difference. The pn-histograms also show many counts at intermediate densities. They are caused by fluid elements resulting from mixing of jet plasma with shocked external medium. This is present in every simulation, although there are typically less counts than in the region of shocked external medium densities (right) or jet densities (left). For decreasing Mach number, the pressure range becomes wider, for all densities. Especially prominent are several straight lines in the pn-histograms. They extend to very low densities, present in the center of vortices. The following example examines the $(M, \eta) = (2.6, 10^{-2})$ jet. The density contours show two prominent vortices (dark blue) in the cocoon. Correspondingly, the pn-histogram shows two spikes extending down to 10^{-3}cm^{-3}. Now, two areas, each centered on one vortex were cut out and examined separately. The individual pn-histograms are shown in Fig. IV.6. Clearly, in the right figure, the upper spike has dis-

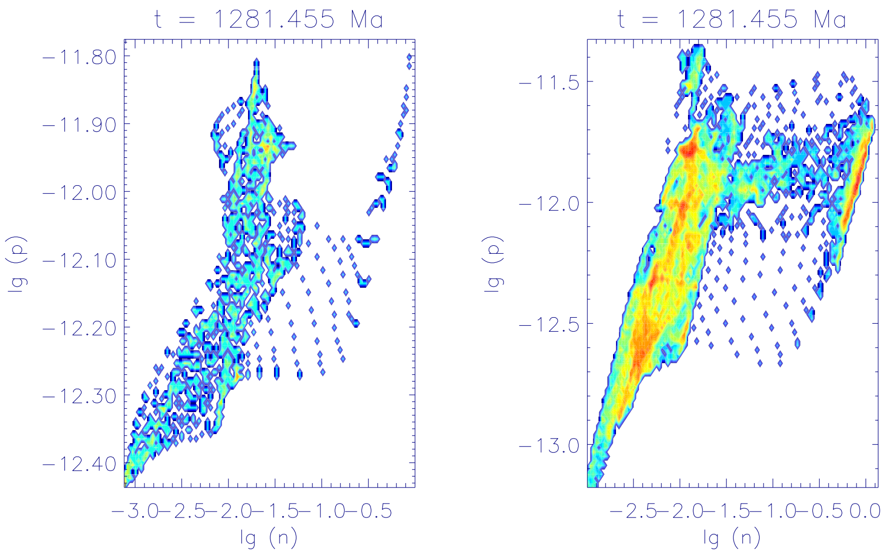

Figure IV.6: *pn-histograms for regions extracted around the two vortices of the* $(M, \eta) = (2.6, 10^{-2})$ *jet. The left figure corresponds to the left vortex.*

appeared. Nevertheless, it is prominent in the left figure. Hence, it is evident that vortices show up in the pn-histograms as straight lines. Therefore they follow the relation $p = \alpha n^{\Gamma}$. For the right vortex of Fig. IV.6 $\alpha = 3 \times 10^{-10}$ and $\Gamma = 1.26$, but obviously these parameters are different for the other vortex.

The bow shock obeys a curved line in the pn-histogram. This is especially evident from the $(M, \eta) = (8.1, 10^{-5})$ simulation. The density contours show most of the space occupied by shocked external medium. In the pn-histogram, these fluid elements, starting at $(\log(n), \log(p)) \approx (0, -12)$, first move upwards, bending to the right. The maximum pressure and density in the shock is reached in a rightmost pinnacle $((\log(n), \log(p)) \approx (0.6, -9.2))$. Then pressure and density decline fast to the isobaric regime. Here the density declines further from $n \approx 0.6$ to $n \approx 0.04$. Even in this case, with the smallest cocoon, 87 %

of the mass is concentrated in the region $8.5\,\mathrm{kpc} < r < 10.5\,\mathrm{kpc}$, justifying the thin shell approximation (see above).

IV.3 Discussion

A very interesting feature of the above results is the blastwave phase. Since the blastwave is faster at early times, it paves the way for the jet, effectively increasing the jet propagation velocity. In appendix A, this phase is mathematically treated, and it is derived that the maximum possible propagation time for a jet is given by (compare equation (A.17)):

$$\Theta_{\mathrm{max}} = 23 \left(\frac{n_0}{\mathrm{cm}^{-3}}\right)^{1/3} \left(\frac{R_\mathrm{j}}{20\,\mathrm{kpc}}\right)^{5/3} \left(\frac{L}{10^{46}\mathrm{erg/s}}\right)^{-1/3} \mathrm{Ma}. \tag{IV.6}$$

The variables in equation (IV.6) are in principal easily accessible for observations in any extragalactic jet. The number density n_0 can be measured, in principle, from X-ray observations, and limits for R and L can be computed from the radio maps. If one has additional information about the inclination and spectrum of a given source, one can further constrain R and L. Equation (IV.6) gives a strict upper limit for the lifetime of jets. Since synchrotron aging studies provide lower limits, equation (IV.6) could provide a useful complement for some jet sources. However, this estimate can still be improved, if the bow shock is detected (see below).

The KH instability at the contact discontinuity is ubiquitous. This is especially interesting since the same behaviour was found for $\eta = 10^{-1}$ at the highest resolution. The KH instability entrains shocked external medium into the jet cocoon, growing and accelerating it towards the center. This mechanism seems to be a promising candidate for the production of emission line regions: the gas is accelerated and pulled down inside the cocoon, where it can radiate by recombination or reradiation of quasar light. Given the high energy content of the radio lobes, one could also imagine that they transfer somehow energy to the emission line gas. Since the cocoon plasma is quite exotic, the classical heat conduction formulas are probably not appropriate. Therefore, exact computations are beyond the scope of this work. The instabilities are biggest on the left-hand boundary. Since the boundary influences the flow in the vicinity of it, the boundary is disturbing. Because of that, some of the later simulations have been made in bipolar mode, evolving both jets and removing the artificial boundary.

Concerning the beams, one can fairly say that those non-relativistic jets without significant magnetic field cannot travel to large distances without being disrupted. One needs a magnetic field in order to keep some of the cocoon around the beam, and to damp the KH instabilities in the beam. Alternatively, they would always look very disturbed, morphologically, until the bow shock had swept enough material away, so they could effectively travel into a less dense medium. For those reasons, such a parameter study should be repeated with magnetic fields.

Chapter V

Simulation of a Typical High Redshift Jet with Time-Implicit Cooling

Observations point to high environmental densities around high redshift radio galaxies (compare chapter I). The cooling time for gas heated by the bow shock due to thermal bremsstrahlung with an emissivity of

$$\Lambda_{\mathrm{ep}}^{\mathrm{brems}} = 2.1 \times 10^{-27} \sqrt{T/\mathrm{K}}\ \mathrm{erg\ cm^3\ s^{-1}} \tag{V.1}$$

is given by:

$$t_{\mathrm{cool}} \simeq \frac{2nkT}{n_{\mathrm{e}} n_{\mathrm{p}} \Lambda_{\mathrm{ep}}^{\mathrm{brems}}} \approx 3 \frac{\sqrt{T/10^7\ \mathrm{K}}}{n/4\ \mathrm{cm^{-3}}}\ \mathrm{Ma}. \tag{V.2}$$

Here the indices e and p refer to electron and proton number densities. This is less than the typical lifetime of a jet. Therefore, cooling has a major effect on the evolution of the post-shock gas. This gas will cool down to high densities and a temperature of about 10^4 K, where the cooling curve drops significantly (Sutherland and Dopita, 1993). In order to study this situation, a hydrodynamic simulation with optically thin non-equilibrium cooling was performed. The computation of hydrodynamic simulations at low density contrast is already quite expensive. The time-implicit cooling part of NIRVANA_C, used here, needed ≈ 95% of the computation time, which occupied the PC for about six weeks. Therefore, no parameter study was attempted.

V.1 Setup

What is typical for a HZRG? Certainly, the luminosity should be approximately 10^{46} erg/s. The model, chosen here, reaches a luminosity of 2.5×10^{45} erg/s for one jet with a proton density of $n_{\mathrm{j}} = 10^{-4}\,\mathrm{cm}^{-3}$, and a jet radius of $R_{\mathrm{j}} = 1$ kpc. The jet velocity was set to 102 kpc/Ma, approximately one third the speed

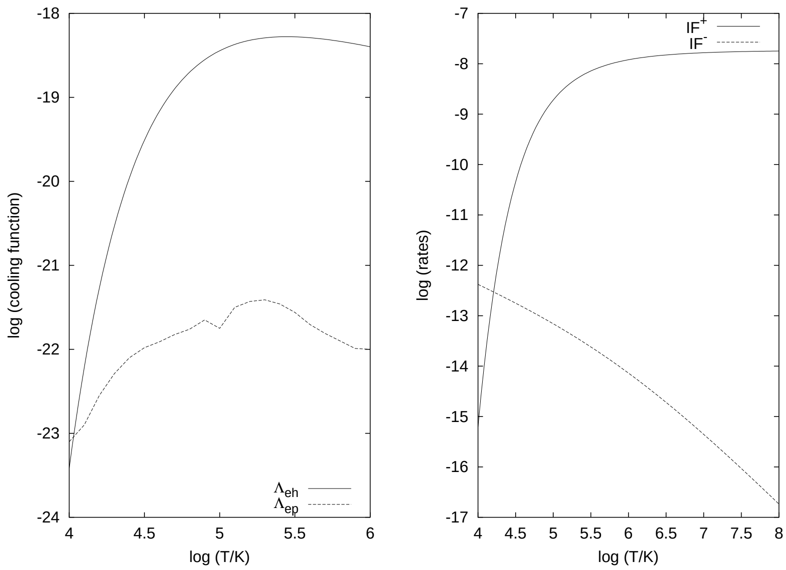

Figure V.1: Left: Cooling functions for ions and neutrals. Right: interaction functions for ionisation (+) and recombination (–).

of light. Because the code is non-relativistic, this is the maximum possible velocity. Three species were used for the calculation: electrons, protons, and hydrogen. The gas was allowed to cool according to equation (V.1), and below a temperature of 10^6 K, an average cooling curve for solar metalicity was applied, following Stone and Norman (1993). In this approximation, the cooling function for the neutrals, represented by hydrogen, are given by (compare page 19):

$$\Lambda_{\mathrm{eh}} = \frac{4.6 \times 10^{-16}}{\sqrt{T/\mathrm{K}}} \exp\left(\frac{-1.4 \times 10^5\,\mathrm{K}}{T}\right) \mathrm{erg\ cm^3\ s^{-1}}.$$

The cooling function for the ions, represented by the protons is complex, and given in Fig. V.1. The interaction functions due to ionisation (+) and recombination (–) are given by:

$$IF^+ = \frac{5.9 \times 10^{-11}\sqrt{T/\mathrm{K}}}{1 + \sqrt{T/10^5\,\mathrm{K}}} \exp\left(\frac{-1.6 \times 10^5\,\mathrm{K}}{T}\right) \mathrm{cm^3\ s^{-1}} \tag{V.3}$$

$$IF^- = \frac{8.0 \times 10^{-11}\,\mathrm{cm^3\ s^{-1}}}{\sqrt{T/3.1\,\mathrm{K}}(1 + \sqrt{T/3.1\,\mathrm{K}})^{0.25}(1 + \sqrt{T/7.0 \times 10^5\,\mathrm{K}})^{1.75}} \tag{V.4}$$

For the recombination, an updated version by Verner and Ferland (1996) was applied that slightly reduces the rate at high temperatures, compared to Stone and Norman (1993).
The external medium was initialised with $T_{\mathrm{ext}} = 10^4$ K, and $n_{\mathrm{ext}} = 1\,\mathrm{cm}^{-3}$. The temperature is not motivated by observations. Cooling is switched off in the calculation below 10^4 K. Therefore the external gas cools only, when it is first reached by the bow shock. This reduces the computational costs significantly. The propagation of the bow shock will not be influenced in any significant way,

since the cocoon is highly overpressured with respect to the external medium (compare chapter IV). Pressure equilibrium was applied, and the hydrodynamic parameters evaluate to $M = 85$, and $\eta = 10^{-4}$. The simulation was carried out in axisymmetry (2.5D), and the jet is resolved with 10 ppb. With that resolution, NIRVANA_C marginally resolves shocks in the jet beam and gets basic flow parameters right. Turbulence on small scales as well as details of the beam, especially of the head region, are unresolved (compare chapter III). The simulation was stopped when the thickness of the shell behind the bow shock shrinked below the resolution, which was clearly the case after a simulation time of 6 Ma. For comparison, a corresponding simulation without cooling can be found in chapter IV.

V.2 Results

The density of atomic and ionised hydrogen is shown in Fig. V.8 for the final time $t = 6$ Ma. Jet and cocoon behave in an almost identical way compared to the non-cooling simulation. The beam is strongly shocked, shortly (but clearly) behind the jet inlet. This pushes the beam (and consequently also the cocoon) to a temperature of $T \approx 10^{11-12}$ K. The backflow assembles in a turning vortex with a size approximately the length of the jet. Most of the mass accumulates into an almost spherical shell behind the bow shock. The maximum density there is 47 cm^{-3}, and the gas has cooled to an average temperature of 1.7×10^4 K in regions with density above 10 cm^{-3}, which still cover almost the whole shell surface. The mass accumulated in this shell is $6.19 \times 10^{10}\ \mathrm{M}_\odot$, 75 % of which are neutral. This gives an average neutral column for the shell of $N_{\mathrm{HI}} = 3.8 \times 10^{21}\ \mathrm{cm}^{-2}$. The amount of matter displaced by the shell is $6.32 \times 10^{10}\ \mathrm{M}_\odot$. It follows that 98 % of the mass are accumulated in the thin shell. Therefore 2 % of the mass or $1.4 \times 10^9\ \mathrm{M}_\odot$ were entrained into the cocoon. Due to the cooling, the shell fragments, disturbing the surface.

The emission due to bremsstrahlung and the Lyman α line is also shown in Fig. V.8. The Lyman α emission was computed according to the classical formula by Seaton (1959), which can also be found in Dopita and Sutherland (2002):

$$\begin{aligned}
\Lambda_{\mathrm{Ly}\,\alpha} &= 5.197 \times 10^{-14} \sqrt{\lambda} \left(0.4288 + 0.4 \ln \lambda + \frac{0.469}{\sqrt[3]{\lambda}} \right) h\nu_{\mathrm{Ly}\,\alpha} n_{\mathrm{e}} n_{\mathrm{p}} \,\frac{\mathrm{cm}^3}{\mathrm{s}} \\
\lambda &= \frac{13.6\,\mathrm{eV}}{k_{\mathrm{B}} T} \\
h\nu_{\mathrm{Ly}\,\alpha} &= 10.2\,\mathrm{eV}
\end{aligned}$$

The Lyman α emission is shown at two times, 3 Ma and 6 Ma. It is concentrated behind the bow shock. On the left plot, it is still spherical, whereas on the right plot, fragmentation has happened. At that time the bow shock has some hot regions, where the X-ray emission due to bremsstrahlung dominates, and some regions, where that process has already cooled the gas. Here, line emission can

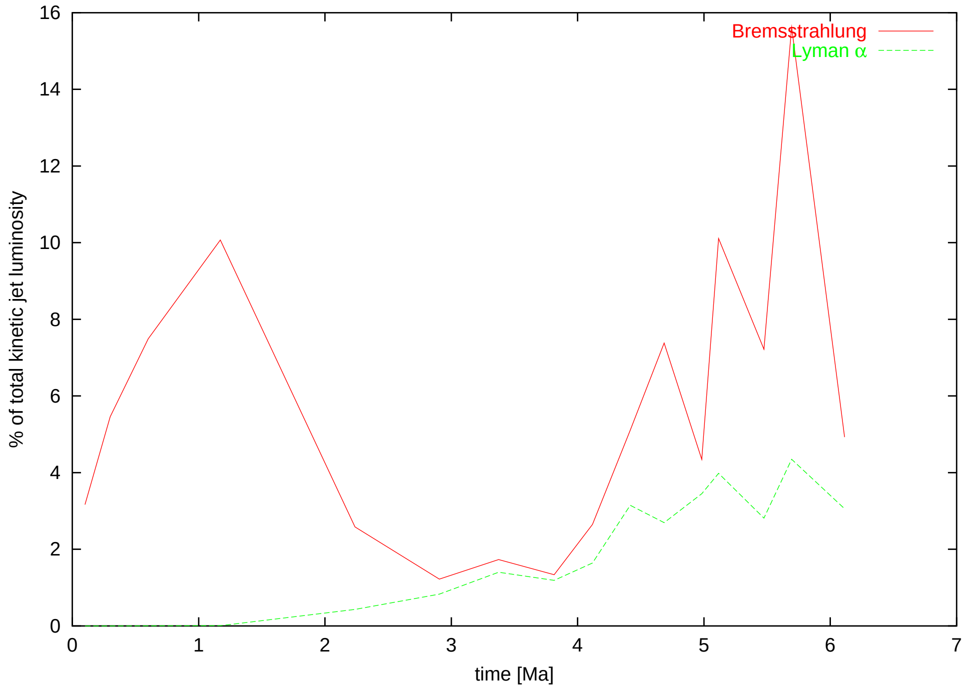

Figure V.2: *Total emitted power in bremsstrahlung and Lyman α over time.*

proceed. The integrated emission over time is shown in Fig. V.2. The first peak in the bremsstrahlung reflects the first cooling event. The whole bow shock cools down. Afterwards, most of the gas is too cool for X-ray emission, and starts to emit Lyman α, which at that time continuously grows. At $t = 3$ Ma, the emitted power from both processes is almost equal. After that time, fragmentation becomes important, and the bow shock shows regions in different states, some dominant in X-rays, some in Lyman α. The timescale for the decay of the

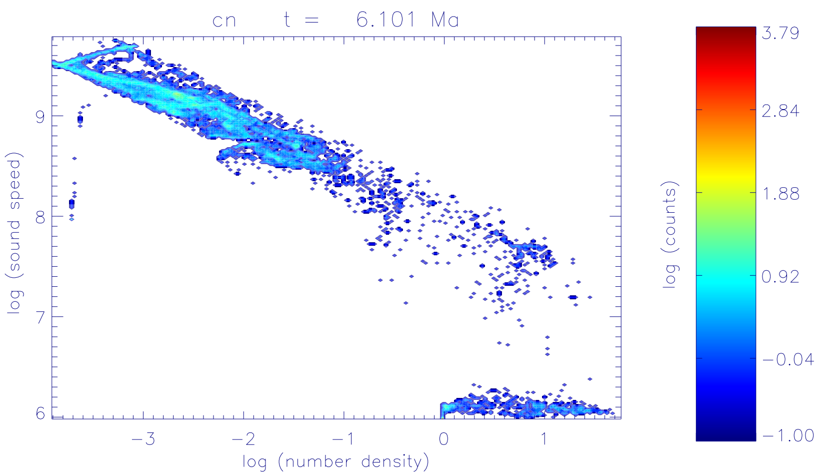

Figure V.3: *Sound speed over number density (cn) histogram for the final snapshot at $t = 6$ Ma. 10^{-1} was added to the counts, so that they can be shown logarithmically.*

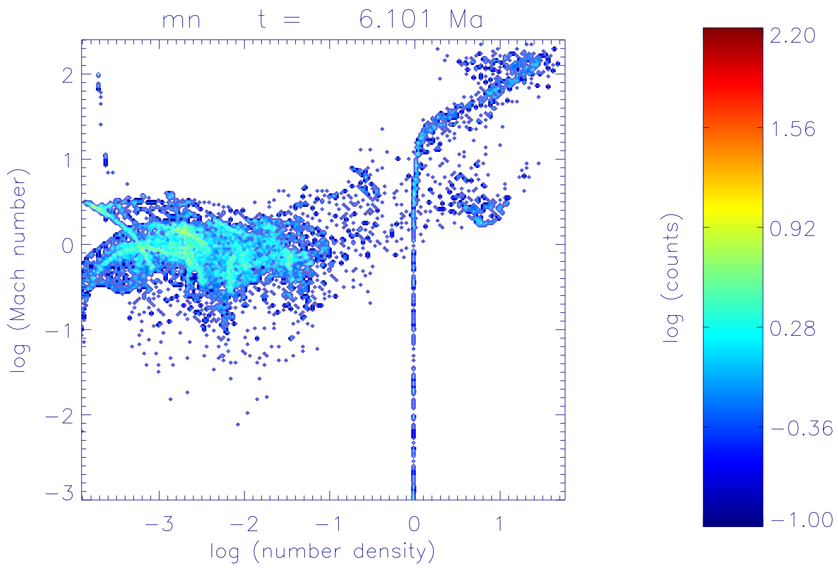

Figure V.4: *Mach number over number density (mn) histogram for the final snapshot at* $t = 6$ *Ma.* 10^{-1} *was added to the counts, so that they can be shown logarithmically.*

bremsstrahlung is shorter at late times. This corresponds to the fact that some of the most luminous X-ray regions (e.g. $R = 4.5$, $Z = 10$, $t = 6Ma$) are among the densest ones. Higher density gives faster cooling. The total Lyman

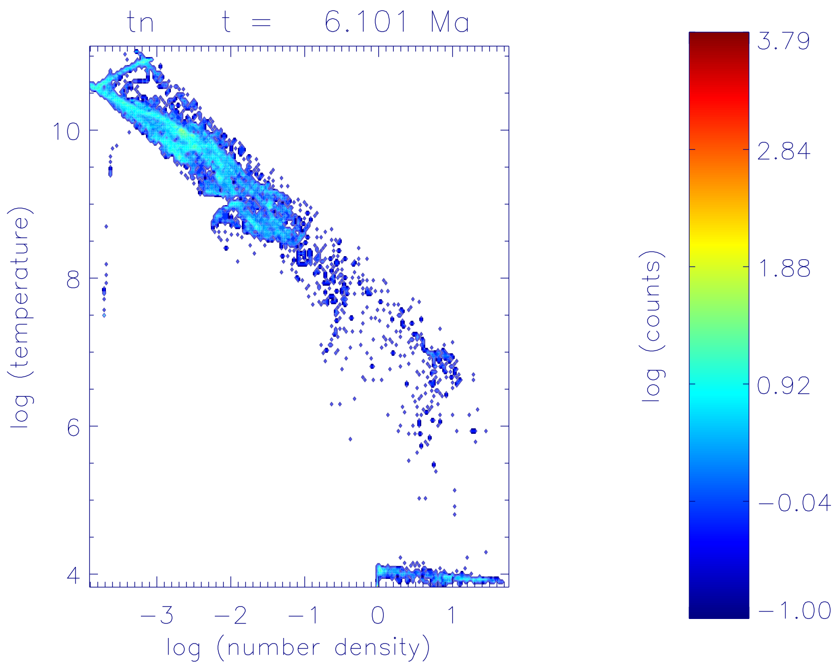

Figure V.5: *Temperature over number density (tn) histogram for the final snapshot at* $t = 6$ *Ma.* 10^{-1} *was added to the counts, so that they can be shown logarithmically.*

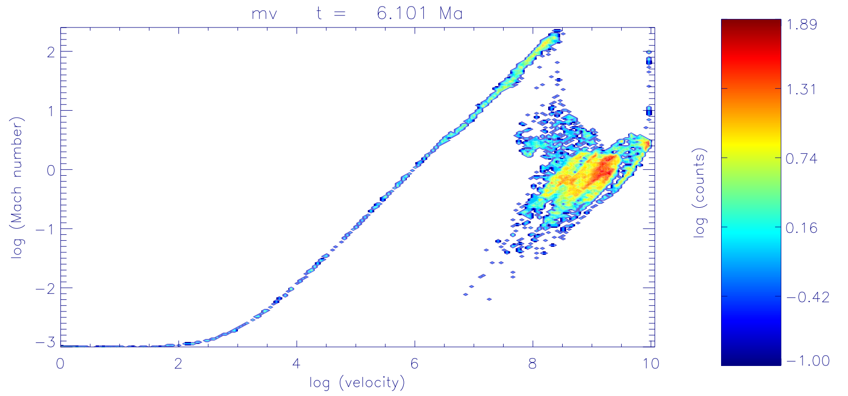

Figure V.6: *Mach number over velocity (mv) histogram for the final snapshot at* $t = 6$ *Ma.* 10^{-1} *was added to the counts, so that they can be shown logarithmically.*

α emission amounts to upto 4 %, bremsstrahlung varies between 2 % and 15 % of the kinetic jet luminosity.

Various histograms are shown in order to achieve a better understanding of the physics. The mn histogram (Fig. V.4) shows that there is a lot of material with Mach number around one. The lack of material with high Mach numbers and low density underlines the early shocking of the beam. When the external material gets into the bow shock, it first moves vertically upwards, to high Mach numbers. The spread in Mach numbers to the right of the $\log(n) = 0$ line reflects the different states and the fragmentation, which has happened to the bow shock. The tn histogram (Fig. V.5) shows that the hot gas ($10^6 - 10^8$ K) in the bow shock is still in pressure equilibrium with the rest of the cocoon,

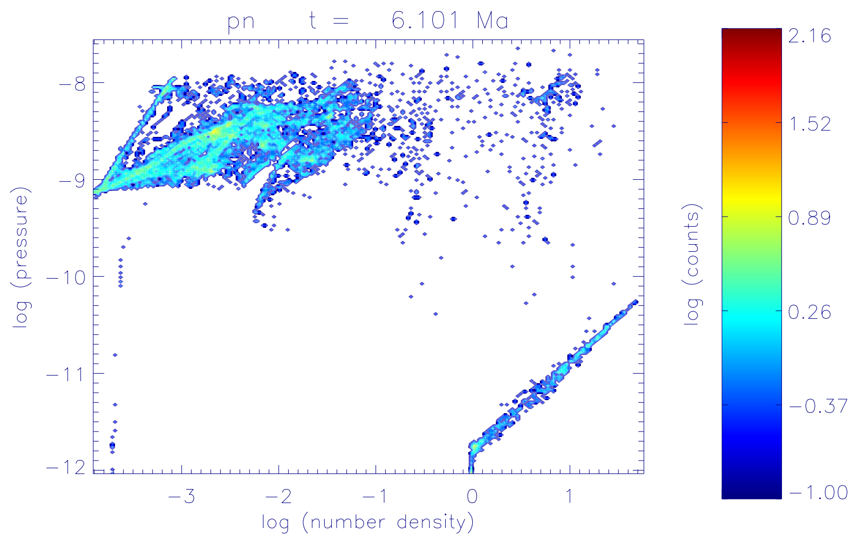

Figure V.7: *Pressure over number density (pn) histogram for the final snapshot at* $t = 6$ *Ma.* 10^{-1} *was added to the counts, so that they can be shown logarithmically.*

because it is located on the $T \propto n^{-1}$ line. But the cooled material no longer follows that law. Its pressure has dropped because of cooling, and the limited resolution prevents it from collapse. The pn histogram (Fig. V.7) shows that this part of the gas is already more than a factor of ten underpressured (compare Fig. IV.2). This is a serious limitation of this computation. It means that the fragments would be smaller than they appear to be. The shell would also be thinner in reality (see below). The sound speed (Fig. V.3) is not affected by that since regions more compressed are denser, and the temperature would be similar, since the gas can only cool to 10^4 K, where it already is in most of the regions affected. The cn histogram reflects primarily the proportionality of the sound speed to the square root of the temperature. The mv histogram (Fig. V.6) shows an interesting linear dependence of the Mach number on the velocity for the shocked external medium. All the other material clumps at high velocity and moderate Mach number.

V.3 Comparison to Observations

Because of the large neutral column, the cool material behind the bow shock is a good candidate for the absorber in HZRGs. The width of an absorption line caused by this absorber would be approximately the sound speed within it (Dyson et al., 1980), which is in our simulation about 55 km/s, on average (compare Fig. V.3). This is in remarkable agreement with observations (van Ojik et al., 1997). The material that is just heated by the shell emits Lyman α at a few percent of the kinetic jet luminosity. This is not far from the observed Lyman α luminosity. So, if the external material would keep a constant density out to the distance, where the jet is observed, the material behind the bow shock would contribute considerably to the total Lyman α luminosity. However, one could expect that the density, in reality, declines outwards. Then the luminosity would scale down with density, whereas the accumulated neutral mass would give a similar column. Therefore the bow shock could be dominating the emission inside of a core radius of the gas distribution, where the gas density declines slowly. Here, the surrounding unaffected gas could absorb the Lyman α. Farther out one could get still roughly the same absorption since the absorbing gas is now conserved and compressed in the bow shock, and entrained material in the cocoon could now be energised somehow, producing the main emission.

For $t > t_{\mathrm{cool}}$, it is justified to approximate the bow shock with an isothermal shock description. Following Steffen et al. (1997), one derives for the thickness of the spherical thin shell:

$$d = 27.7 \frac{(\bar{m}/m_{\mathrm{p}})(r_{\mathrm{bw}}/10\,\mathrm{kpc})(T/10^4\,\mathrm{K})}{(v_{\mathrm{bw}}/100\,\mathrm{km/s})^2}\ \mathrm{pc}. \tag{V.5}$$

Here, $\bar{m}/m_{\mathrm{p}}$ denotes the mean molecular weight per proton mass. The shell is again described by the blastwave equations given in appendix A. Here, this approximation is even better satisfied as in the non-cooling case, since cooling reduces the thickness of the shell considerably. The sound crossing time through this shell is about 5×10^5 yrs, which is longer than the cooling time (about 10^4 yrs, Sutherland and Dopita (1993)). Therefore, it is possible that the shell breaks up into individual subshells (Dyson et al., 1980). This could well correspond to the multiple associated absorption systems, often observed in HZRGs. There is of course the possibility, that also other absorption systems are around in individual systems. The observed absorbers are preferentially blue shifted, a natural feature of our model. But almost never, a velocity above 250 km/s is observed. Approximating the sideways expansion of the bow shock by the laws for the spherical shell (appendix A) also for some time after the jet head begins to shape it, one can calculate η, given the bubble size (> 12 kpc) at observation time. This yields $\eta = 2 \times 10^{-5}$, which means that the full range of currently known observations can be explained if the environmental density is ≈ 5 cm^{-3}. It is interesting to note here that very similar numbers have been found from quite different arguments for the environment of the radio galaxy 4C 41.17 (Bicknell et al., 2000). The model implies a low sound speed in the external medium $c_\mathrm{s} < 200$ km/s, which is consistent with the absence of an X-ray atmosphere in 1138-262 (Carilli et al., 2002), and a necessary consequence of such a high density environment.

The bubble interior looses an amount of internal energy via synchrotron radiation, which is not included in the simulation. This lowers the requirement for the external density (but compare chapter VI). Although the observed hydrogen mass in these systems barly exceeds $10^9\mathrm{M}_\odot$, it is likely that they contain significantly more mass. Given that HZRG host the most powerful quasars of the universe, we should expect black hole masses of the order $10^9\mathrm{M}_\odot$. The gas mass should be more than that. If the gas mass would be of the order $10^{11-12}\mathrm{M}_\odot$, as is suggested here, the gas to black hole mass ratio would be similar to the bulge to black hole mass ratio found at low redshift.

The shell is not only thermally, but also gravitationally unstable. The time, when the instability on the shell surface occurs for the first time is (Wünsch and Palouš, 2001), again for constant energy injection rate and for the parameters of our model:

$$t_\mathrm{i} = 24 \left(\frac{(c_\mathrm{s}/55\,\mathrm{km/s})^5}{(r/\mathrm{kpc})^2(\eta/10^{-4})(3v_\mathrm{J}/c)^3(n/\mathrm{cm}^{-3})^5} \right)^{1/8} \mathrm{Ma}. \tag{V.6}$$

Gravitational and thermal instability will support each other. The Jeans mass in the shell is $\approx 10^6 - 10^7 M_\odot$. Hence, the shell will form stars in globular clusters of that mass. Assuming an efficiency of 10%, the shell would form, roughly, 10^4 globular cluster systems. This is in remarkable agreement to what is found in nearby BCGs, like e.g. M87 (Harris et al., 1998): BCGs show an excess of globular cluster systems of about $10^4 - 10^5$ compared to non BCG ellipticals with comparable luminosity. Sometimes, two distinguished globular cluster populations are observed. Harris et al. (1998) consider various formation scenarios in detail and conclude that a kind of galactic wind must have driven out a large fraction of the galaxies gas, before it was able to form stars.

When the shell fragments, its covering factor decreases further and the absorption vanishes. This scenario could nicely explain, why no absorbers are observed for jet systems larger than 50 kpc. Afterwards the shell would become visible in the optical, due to the newly born stars, which will also increase the ionisation of the remaining parts of the absorbing shell. A bubble shaped star forming region like that can be found around the radio galaxy 1243+036 (van Ojik et al., 1996).

These associated absorption systems also seem to be observed in high redshift quasars (Baker, 1999, 2001; Baker et al., 2001). There, they have velocities of a few thousand km/s, consistent with the model, if one assumes that the line of sight in quasars is not far from the jet axis. In addition, this part of the shell could be accelerated by photoabsorption of photons from the quasar (Falle et al., 1981).

In the simulation, $\approx 10^9 M_\odot$ of shocked IGM are entrained into the cocoon. This number should not be taken too literally, because small scale turbulence could change that and high resolution studies are required to get this number accurate. Nevertheless, it is slightly more than the typically observed Lyman α emitting gas mass. Higher resolution would also be essential in order to determine the mixing properties and density of this gas. The big vortex, we observe in the cocoon is an ideal accelerator for the entrained gas. In the simulation, the gas is swept along, and accumulates mainly on the left-hand side and along and next to the jet beam. There it is spun up to a velocity of ≈ 1000 km/s. One could expect that at higher resolution, small scale Kelvin-Helmholtz instabilities will entrain mass at the boundary of the vortex, similar to the high resolution cases in chapter III. Given the high velocity of this propeller, it seems quite likely that emission line gas could be accelerated to the observed velocity of ≈ 1000 km/s. Some of these predictions are confirmed in chapter VII.

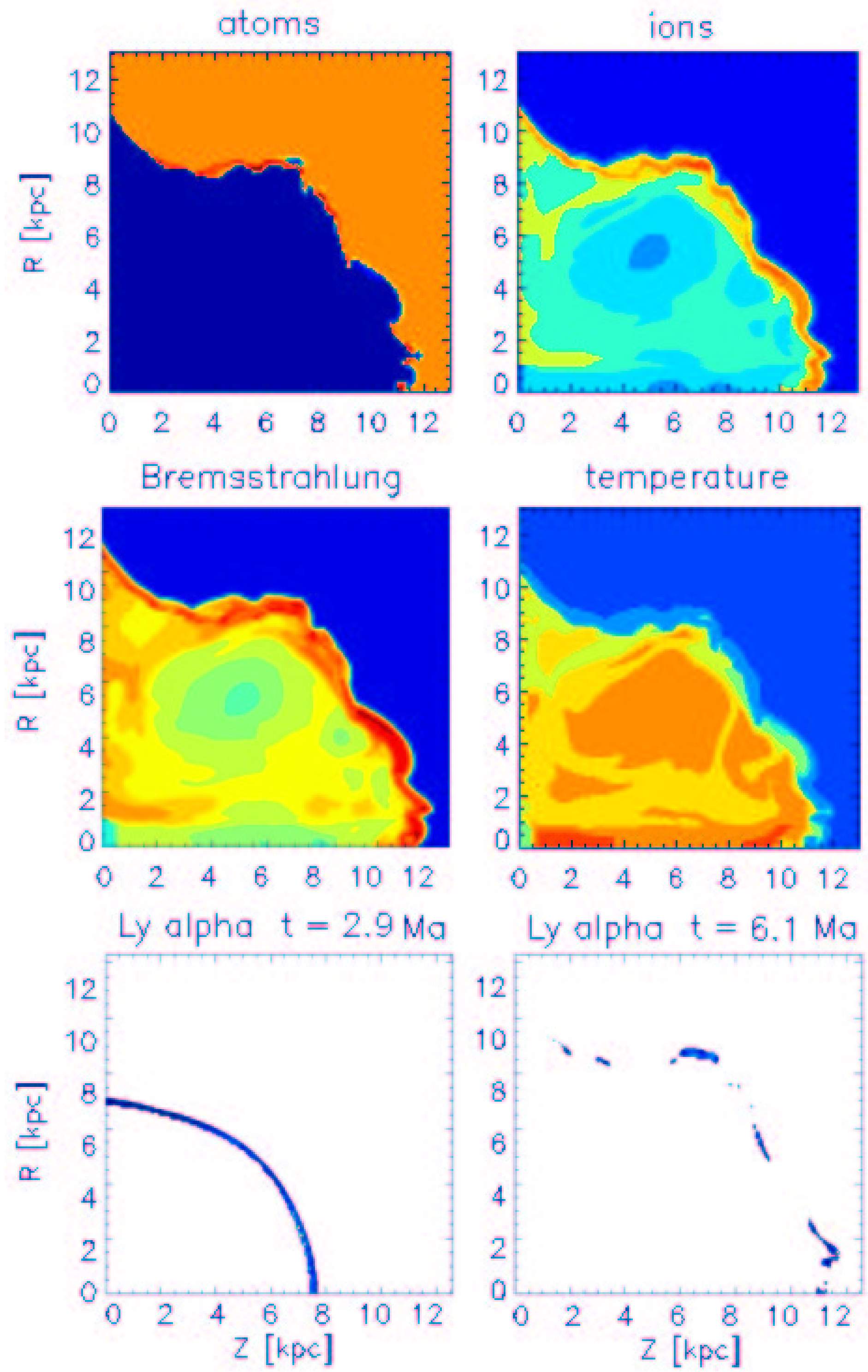

Figure V.8: *Densities of atoms and ions (upper plots), temperature and bremsstrahlung (middle row) for the final timestep of the simulation, which corresponds to 6.1 Ma. In the bottom plots, the Lyman α emission is shown, which is linearly plotted. For all the other plots, the colour codes represent logarithmic levels from dark blue (low) to red (high).*

Chapter VI

Bipolar 3D Simulation in Cylindrical Coordinates with King profile

In order to improve the understanding of what is really going on in HZRG, one has to adapt the conditions of the simulation as much as possible to estimated parameters of real sources. This should be a stepwise process, in order to understand, what the consequences of the individual changes are. In the present chapter, three new physical ingredients are introduced: first, the counter-jet, second a declining external density according to a King profile, and last the third dimension. The simulation was carried out with the same parameters as Clarke et al. (1997). They are based on the ROSAT data of the Cygnus A cluster gas and parameters, which were (sometimes only slightly) favoured in the review by Carilli and Barthel (1996). The simulation was started just when the analysis of the new Chandra data became available on the web. So, the new data was not taken into account for the simulation. From the theoretical point of view, this is not too bad, since now only one main physical ingredient is different in comparison to Clarke et al. (1997): the counter-jet. Clarke et al. (1997) had to use a low resolution for their 3D simulation. They resolved the jet radius, which is already assumed to be three times the observed radius, with 5 points radially, and 2.5 points axially in the vicinity of the axis. For the presented simulation thirty times more memory and a hundred times more CPU time (approximately three weeks) was used, on a faster machine. Even though, the resolution is still restricted by the available memory. In order to relax this problem a little bit, a cylindrical grid was applied. The boundary conditions in that case are quite difficult, but the problem could be solved (see below and section II.4), and the real jet radius could be used and resolved with 8 points in each direction.

VI.1 Simulation Setup

A cylindrical grid was used for the jet simulation (compare section II.4). The size of the computational domain was: $Z \in [-69 \text{ kpc}, 69 \text{ kpc}]$, $R \in [0, 57 \text{ kpc}]$ and $\phi \in [0, 2\pi]$. 2042, 805, and 57 grid points were used in the Z,R and ϕ directions, respectively (run A). For a study of the early behaviour, another simulation was carried out with one tenth the dimensions of run A, and 202, 83, and 60 grid points were applied (run B). With a jet radius of $r_\mathrm{j} = 0.55$ kpc, this gives a resolution of 8 ppb for run A and B. The resolution in ϕ direction scales linearly down from 16 (17) ppb on the jet boundary to 0.2 (2) ppb on the edge of the grid for run A (B). The grid was initialised with an isothermal King cluster atmosphere:

$$\rho(r) = \frac{\rho_0}{\left(1 + (\frac{r}{a})^2\right)^{3\beta/2}} \quad , \tag{VI.1}$$

where $r = \sqrt{R^2 + Z^2}$ denotes the spherical radius, $\rho_0 = 1.2 \times 10^{-25}$ g/cm^3 is the characteristic density, $\beta = 0.75$ and $a = 35$ kpc is the core radius. The initial distribution of the gas density is shown in Fig. VI.1. In order to break

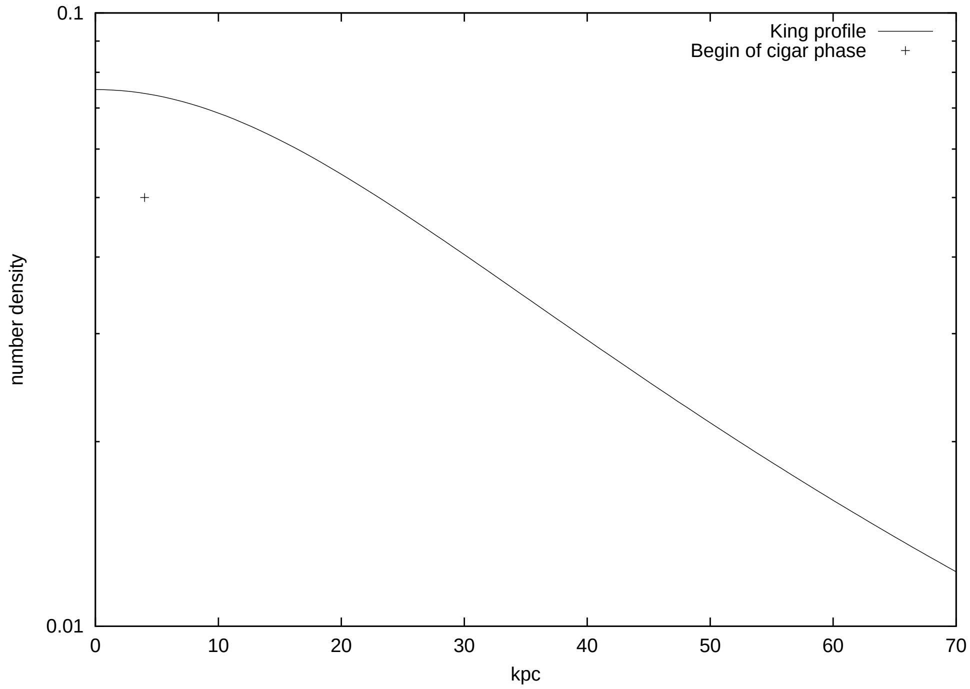

Figure VI.1: *Initial gas density distribution. The start of the cigar phase is described in the text.*

the bipolar and axial symmetry, this density profile was modified by random perturbations of the following kind:

1. With 10% probability the density was increased by a factor between 1 and 1.4.

2. With 5% probability the density was increased by a factor between 1 and 2, only if the cell was unmodified in the first process and the Z coordinate was positive.

The jet is injected in the middle of the grid in the region $Z \in [-0.55, 0.55 \text{ kpc}]$, $R \in [0, 0.55 \text{ kpc}]$, and $\phi \in [0, 2\pi]$. This region has the constant values: $\rho_{\text{jet}} = 6.68 \times 10^{-28}$ g/cm^3, $v_Z = \pm 0.4c$, where c denotes the speed of light. The plus sign applies for the positive Z region and the minus sign for the negative one. This gives a jet luminosity of $L_{\text{kin}} = 1.04 \times 10^{46}$ erg/s for both jets together. The pressure was set in order to match the external pressure at that position. This gives a slightly varying density contrast across the grid of $\eta = \rho_{\text{jet}}/\rho_{\text{ext}} \approx 7 \times 10^{-3}$ and an internal Mach number $M = 10$. The jacket of the injection cylinder is a further boundary. This boundary is open, so the material can leave the grid here into the central kiloparsec of the simulated radio galaxy, which is not attempted to model here. The temperature in the external medium is set to 3×10^7 K. The cooling time in the shocked cluster gas is approximately 100 Ma. The jet is expected to propagate through the whole volume in 10 Ma. So, cooling marginally influences the state of the gas. This was taken into account by diminishing the internal energy by the amount given by equation (V.1) in every timestep. Thus the calculation is not scalable anymore, formally. But given the smallness of the effect, scaling should be possible, in practice. Because the atmosphere is isothermal, the pressure varies in the same way as the density. In order to keep the system in hydrostatic equilibrium, the gradient of the dark matter potential was added to the source terms on the right-hand side of equation (II.3). The gravitational potential, necessary to prevent the King atmosphere from exploding is:

$$\Phi_{\text{DM}} = \frac{3\beta kT}{2\mu m_H} \log\left(1 + (r/a)^2\right) \tag{VI.2}$$

VI.2 Early Evolution

The early evolution (run B) of the simulated jet is shown in Fig. VI.2. The images show the formation of a bow shock and backflows, for both jets. [1] The pressure and density increase can be followed by the maximum values at the top of the individual colour bars. In that phase, the jet almost ignores the stochastic nature of the density. The bow shock has a round and regular shape, and besides the very first snapshot, the density varies smoothly along its surface. However, the evolution on the two sides is different. The jet on the left-hand side evolves faster: It produces a bigger bow shock, and a faster backflow at equal times. At $t = 0.06$ Ma, the two bow shocks are nearly joined together. As the later evolution will show, a single round bubble forms, soon after. [2]

[1] These pictures do not show the evolution of a small radio source.

[2] This is not self-evident. At higher density contrast two bubbles are discernible up to large jet lengths. In that case, the high pressure region at the meeting point of the bow shock seen in the later pictures in Fig. VI.2 could lead to the perpendicular bow shock like features,

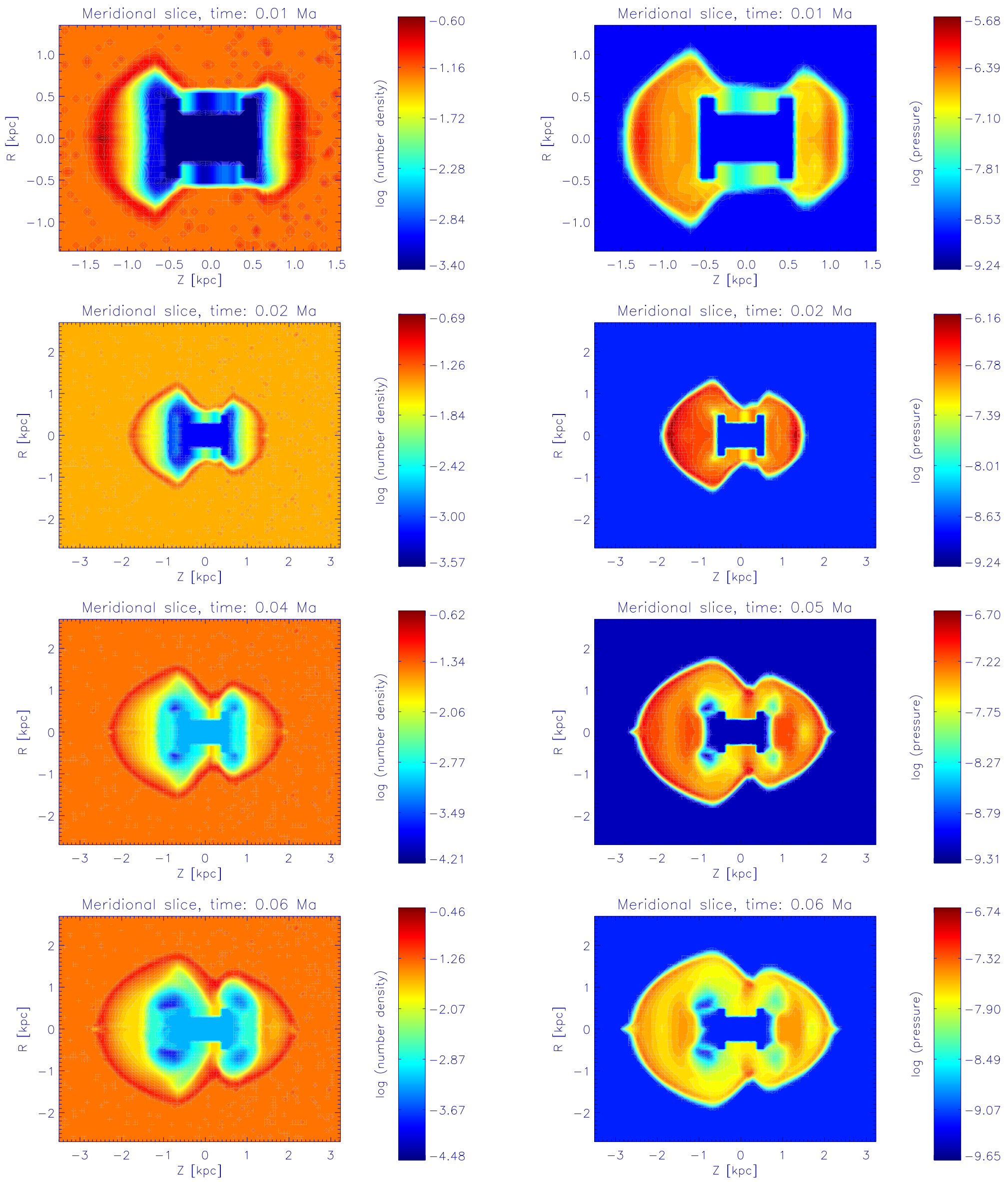

Figure VI.2: *Logarithmic colour representation of the very early evolution. Meridional slices at* $\phi = 0, \pi$, *joined at the axis, of number density (left) and pressure (right) are shown at four times, indicated on top of the individual pictures. The top row is magnified by a factor of two.*

The upper and lower halfs of the pictures fit quite good together. The only suspect phenomenon is the spike at the apex of the bow shock on both sides. This numerical artefact reminds us on the imperfect treatment of the axis. The effect is rather small, and sometimes even absent. This is a reassurance for the choice of boundary conditions on the axis (compare section II.4).

---

sometimes seen in HH objects e.g. on the famous FORS picture of HH 34, alleviating the need for a perpendicular rotation axis of binary stars.

VI.3 Long Term Evolution

A snapshot of several quantities at $t = 0.32$ Ma is shown in Fig. VI.3. The jet plasma takes the lowest density, and the highest temperature values. At that time, the evolution has just continued in the same way as in the early phase: the right-hand side, propagating into the on average denser medium, develops a broader cocoon, and is slower. The once separated bow shocks have united. The shape of the bow shock in that phase is oval, witnessing the blastwave phase. The bow shock shows two extensions in jet direction. Due to their later appearance, these parts of the bow shock will be called *cigar* like. The aspect ratio of the bow shock is nearly 2, thanks to the extensions, which contribute approximately 0.5 to the aspect ratio at that time. The temperature takes values of more then 10^{11} K in the jet beam and the cocoon. This is typical for a jet with velocity close to the speed of light and a bulk flow consisting of thermal matter, which can be figured out from standard shock jump conditions (e.g. Dopita and Sutherland, 2002): $T \approx 1.3 \times 10^{11} v^2$ K, where v is the velocity of the shock in units of 100 kpc/Ma. Relativistic shock jump conditions yield even higher temperatures.

The pressure plot shows a high pressure at shocks in the beam, especially on the axis. While this is in principal ok, the exact amount of the pressure could be influenced by the choice of the cylindrical coordinate system. The first shock in the beam is stronger on the left-hand side. This follows from the higher pressure there, but also from the higher inclination angle to the axis. Since the beams have identical conditions, why are the shocks not identical? The shocks in the beam are driven by whatever hits it. From the density plot, this seems to be the cocoon on the left-hand side, and the entrained cluster gas on the right-hand side. The backflows collide approximately at the center, forming a region of enhanced pressure. This region is asymmetric at the time shown here. Due to the stronger backflow from the right-hand side, the region has moved to the left. The higher pressure there drives a stronger shock into the beam. This explains, why the first shocks are different on both sides.

The stronger shock on the left-hand side causes the beam to widen, due to high pressure. On the right-hand side, less energy has been converted into heat, the beam stays narrow, and delivers more power to the terminal shock, where the pressure is consequently higher. The asymmetric, centrally enhanced pressure region pushes the entrained shocked cluster gas to the right, where it slips between beam and cocoon, thereby widening the right cocoon. These fingers of shocked cluster gas, reaching down to the very center of the computational domain, are present just like they are in the unipolar 2.5D simulations (e.g. Fig. V.8). They are generated in the following way: KH instabilities are excited at the boundary between cocoon and shocked external medium. The backflow advects those instabilities, while they are amplified. Hence, they are biggest in the symmetry plane. The material in the symmetry plane could in principal flow outward, creating bumps in the bow shock, or inward. The simulation clearly shows no sign of outward motion. Instead, the gas is transported

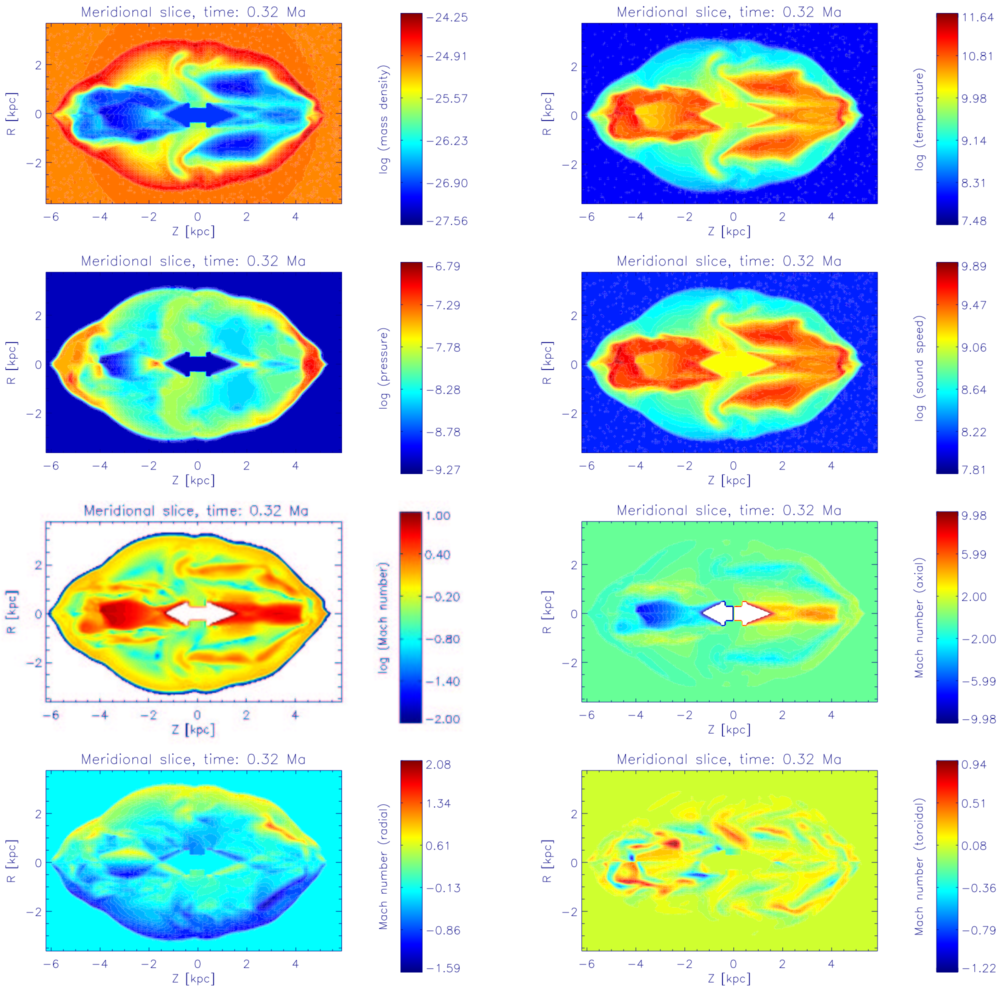

Figure VI.3: *Meridional slices for $\phi = 0/\pi$ at 0.32 Ma. The quantity plotted is indicated next to the colourbar. Upper (lower) colourbar values give maxima (minima) in the plotted region. The sound speed is given in cm/s.*

far down into the radio cocoon in geometrically thin fingers. Soon, their extension falls below the resolution limit of the simulation, and the gas mixes with radio plasma. However, in reality, the two phases will remain separate. The magnetic field of the radio plasma further supports the separation of the two phases. In principle, in that way new fuel could be channeled to the central source. However, the dynamics of the central kpc is beyond the scope of this work.

Usually, the cocoon is a region of low pressure and density, since the material that was shocked at the Mach disk has expanded. The low pressure region is much more prominent in the right cocoon, again indicating that the left cocoon is compressed by the displaced symmetry plane due to the stronger backflow from the right.

The plot of the total Mach number shows supersonic velocities all over the

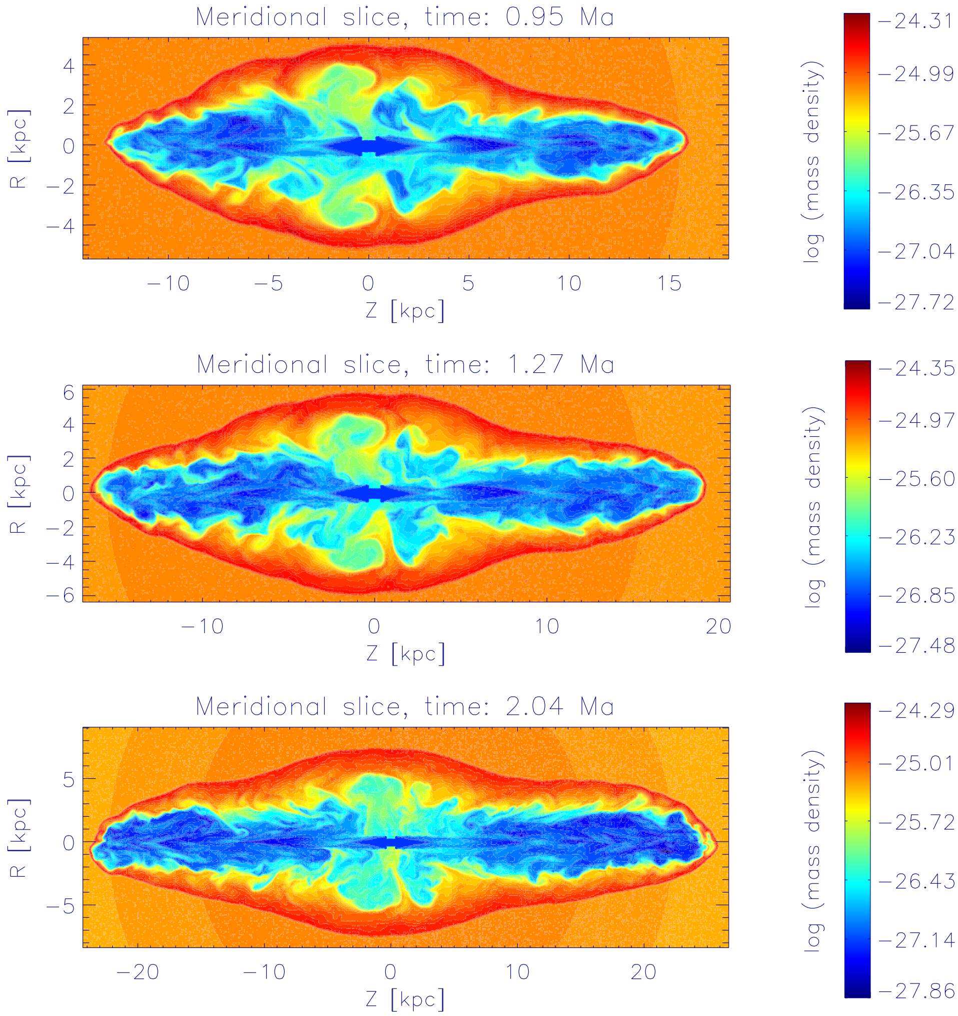

Figure VI.4: *Logarithmic density for different times. Notice that the jet now has propagated further to the right-hand side then to the left, contrary to the situation of Fig. VI.3. The jet develops a regular cigar shaped cocoon.*

bow shock, in the beam, and on the outer sides of the backflow. Interestingly, also the fingers of shocked external medium have a considerable Mach number. This is mainly due to the low sound speed of approximately 1 kpc/Ma, typical for the shocked external medium with temperatures of a few times 10^8 K. Where does the gas flow to? The fingers are not prominent in the plots of the axial or radial Mach number, but the upper right one of the fingers is a prominent feature in the plot of the toroidal Mach number ((R,Z)≈(0,1), red). The finger on the other side of the jet is more yellow, but rotates in the same direction. Therefore, the fingers mainly rotate. This is one of a few examples of large scale rotation. The jet beam is not dominated by rotational motions. For example, to the right of the first shock in the right jet, the toroidal Mach number shows blue

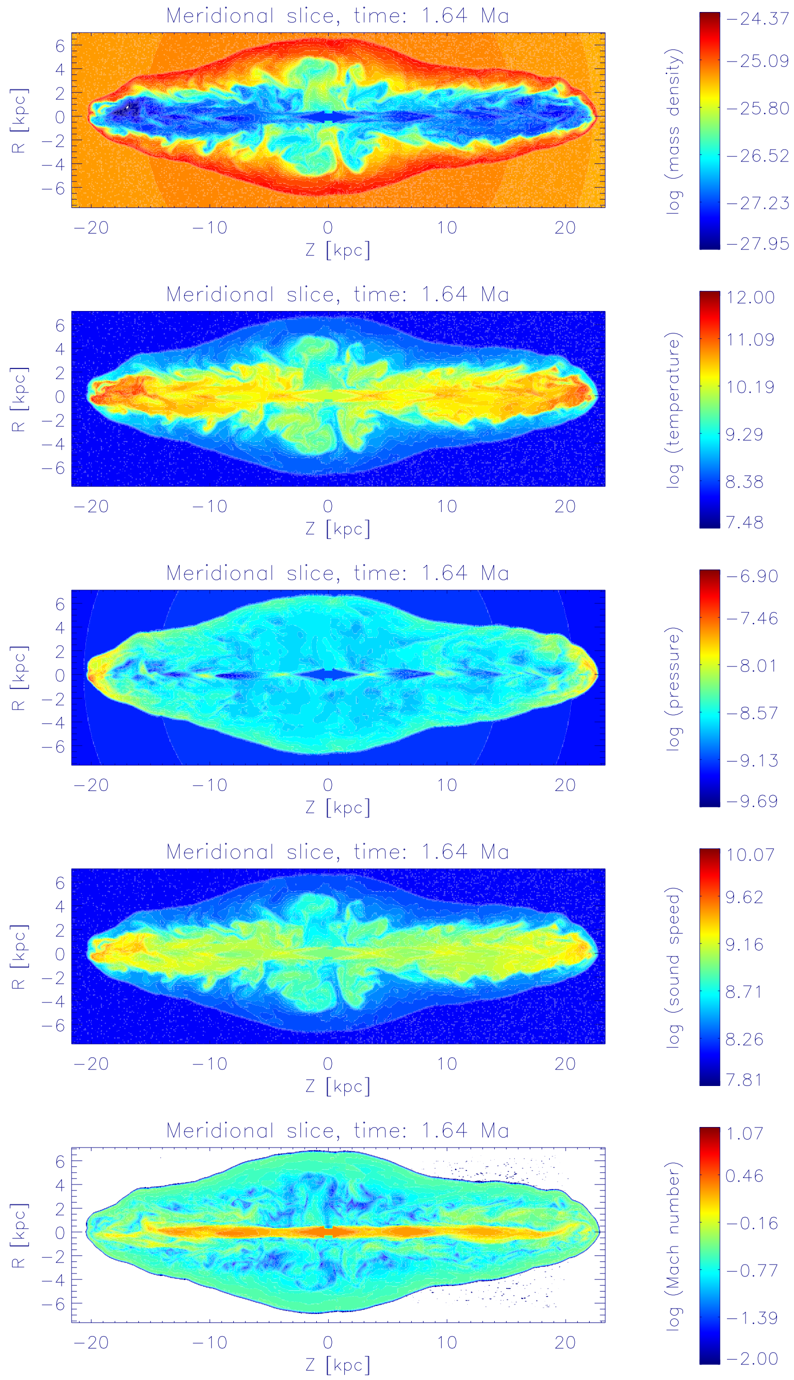

Figure VI.5: *The same as Fig. VI.3, but for* $t = 1.64$*. The Mach number for the three directions is plotted in Fig. VI.6.*

on one side, and red on the other, which indicates movement out of the plane of the paper, on both sides. The same is true for the regions near the hot spot on either side. Thus the jet beam, especially the head prefers wobbling around over

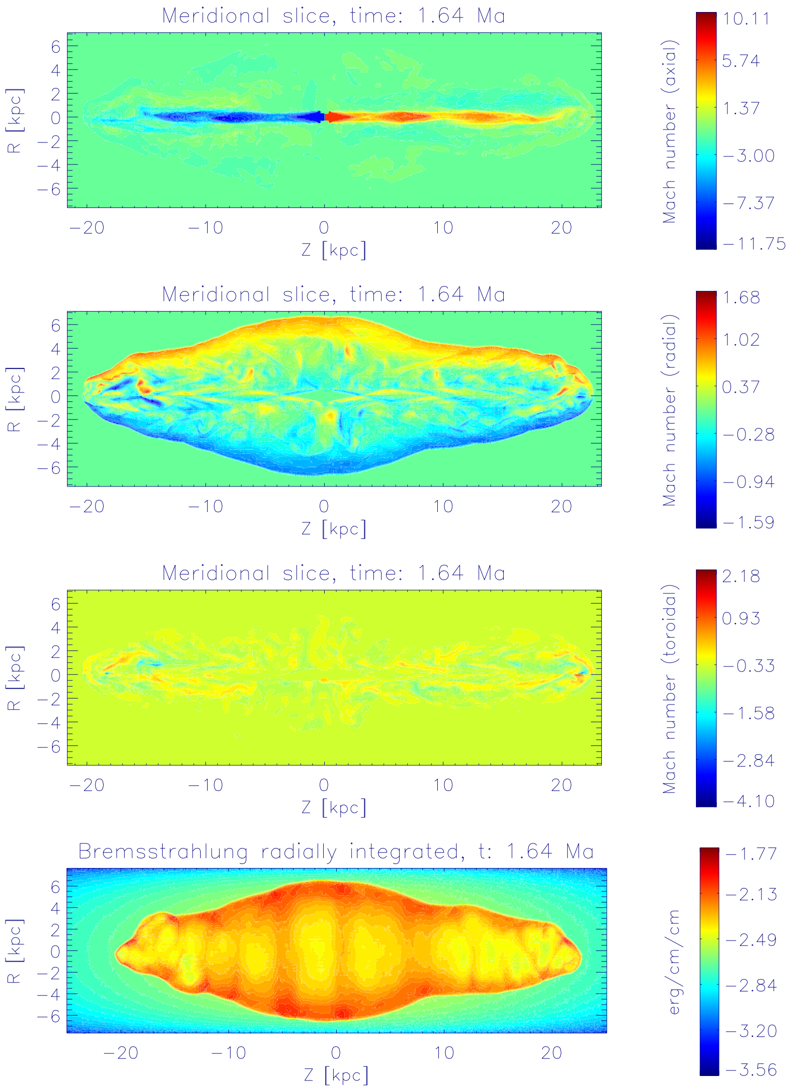

Figure VI.6: *Continuation of Fig. VI.5. The emission due to bremsstrahlung integrated along a radial line of sight (after conversion to Cartesian coordinates) is shown at the bottom. An X-ray cavity and a bright edge formed by the bow shock is evident.*

rotating. The radial Mach number is high in the bow shock region, but hardly exceeds one. High radial Mach numbers are also found at the oblique shocks in the beam, which underlines that they are in fact radial shock waves excited from outside, and advected with the beam. These shocks first move inward, cross at a certain point on the axis, and then move outward again, until they reach the beam boundary, where they are deflected inward, once more. The highest radial Mach number is achieved in the forward part of the cocoon on the right-hand side. This is responsible for the higher pressure in front of that region.

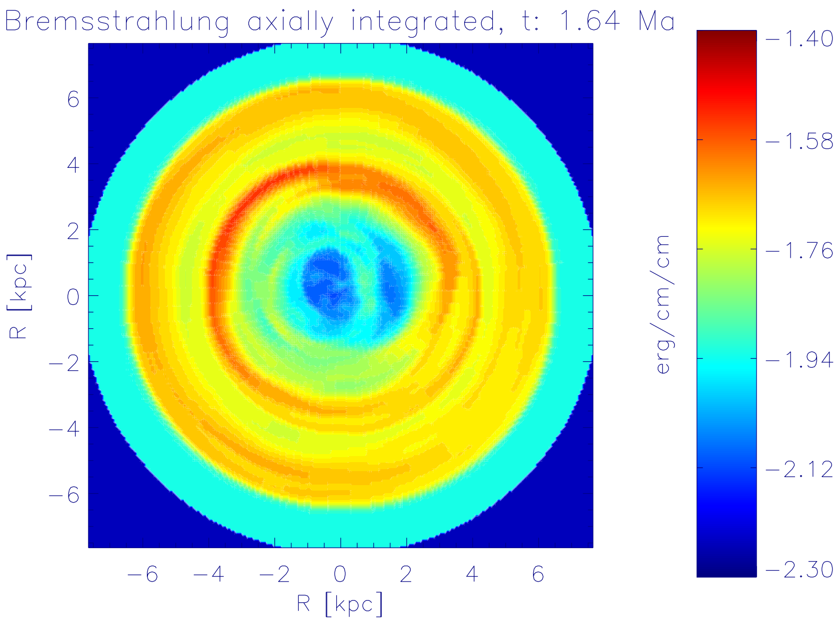

Figure VI.7: *Bremsstrahlung integrated along the axial direction at* $t = 1.64$ *Ma: The radio source has blown up an X-ray cavity.*

It has already been pointed out above that at the time the simulation is shown at in Fig. VI.3, the left jet converts more kinetic energy into heat than the jet on the right-hand side. At that time the tip of the jet has already advanced approximately 20 % further towards the left than towards the right. The difference of the average density is only 2.5 %, which cannot explain the fast propagation of the left jet. The position, the bow shock has reached at that time is indicated in the density profile (Fig. VI.1). The slight decrease in the density can hardly cause the fast acceleration with the discontinuous bow shock. One important result is therefore that the nonlinear dynamics amplifies the effect of the different density on both sides by more than a factor of ten. Probably, the faster development of the left backflow during the early evolution had first increased the pressure in the vicinity of the right beam. Unfortunately, snapshot times have to be fixed beforehand of the calculation, and no snapshot was made between the early propagation and 0.32 Ma. The situation at that time is unstable, and the later timesteps show that the right jet catches up, and outruns the left one not later than at t = 0.95 Ma (compare Fig. VI.4). The situation stays that way until the end of the simulation. On average, the right jet is approximately 10 % faster than the left one, at late times. This is in conflict with naive intuition, but readily explained, considering that the stronger backflow from the right jet shifts the central pressure enhancement to the left, where stronger oblique shocks are driven into the beam slowing the left jet down, as pointed out above.

The snapshot at t = 1.64 Ma is shown in detail in Figs. VI.5 and VI.6. Density and temperature plots show the usual picture of a hydrodynamic jet

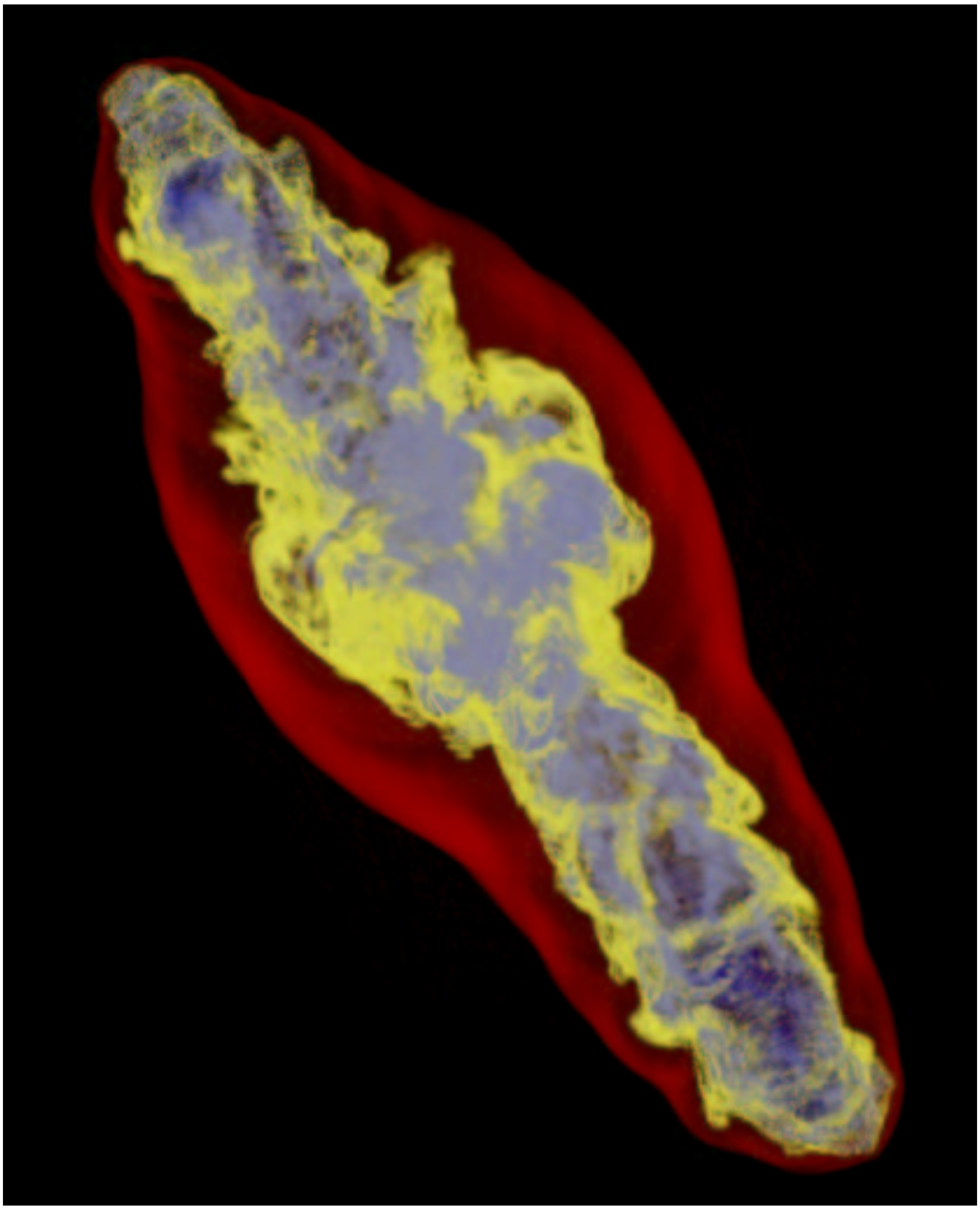

Figure VI.8: *Clipplane at t = 1.64 Ma: The cylindrical data has been mapped onto a Cartesian grid, volume rendered, and the upper half was cut off. Three windows of density values have been selected. One represents values achieved in the bow shock (red), one takes values achieved in the shocked external medium (yellow), and another one represents even lower density, which is representative for the cocoon (blue). Notice that yellow regions extend far into the radio cocoon, in central regions.*

simulation, consistent with FR II radio galaxies: The cocoon is now nicely placed around the jet beam. The aspect ratio of the bow shock is 3.6. The KH instabilities show up prominently. They still grow towards the center, and develop into long fingers at the innermost positions. The pressure shows a regular spacing of shock compressed and rarefaction zones in the beam. High

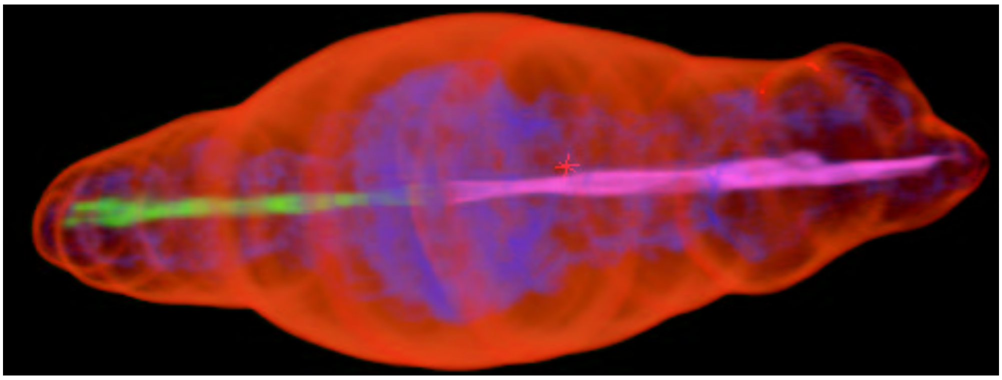

Figure VI.9: *Volume rendering for the snapshot at* $t = 1.64$ *Ma similar to Fig VI.8. A density window representing the bow shock was drawn in red. Velocity windows typical for the beams were highlightened in pink and green. An intermediate density region is shown in blue.*

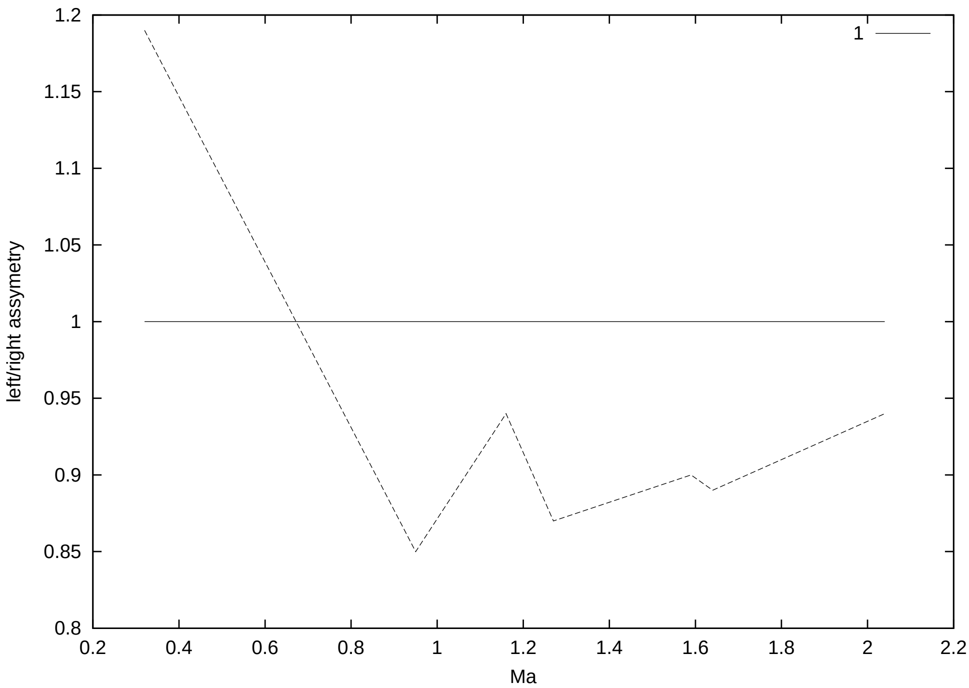

Figure VI.10: *Left to right armlength ratio over time. First the left jet is faster, then the right one.*

pressure regions are small and show up only at the end of the beams, where the Mach disk is located. The oblique shocks in the beam are now weaker than at $t = 0.34$ Ma. This follows from the smaller angle with the jet axis. The central region, with a diameter of roughly 10 kpc, is now dynamically calm. No large Mach numbers are observed there, and the pressure is approximately constant. The density takes intermediate values. This is now a relaxed region where jet plasma and shocked cluster gas are mixed. (Of course, mixing does not happen in nature, see above.) Interestingly, the toroidal Mach number has increased considerably. This is due to even larger wobbling of the beam.

For a better visualisation of the 3D properties, a ray tracer was applied. The commercial product volume graphics was used. For that purpose, the volume was mapped onto a Cartesian grid. With volume graphics, one can assign different opacities and colours to certain values of the desired quantity. In order to get a concise picture, one selects certain windows where the opacity is finite, and leaves the rest transparent. Different windows are assigned different colours. Usually, innermost structures are optically thick, outer ones translucent. Density sheets highlighting bow shock and some intermediate density material, and velocity pipes highlighting the beam, are shown in Fig. VI.9. One can see that the beam radius slightly decreases with distance from the center, and that the beam splits in the head region. Changing head flow directions have carved their signs onto the walls of the bow shock. They are visible as bumps. While both processes are well known from simulations in the literature (compare introduction), the exact nature of the process may be influenced by the boundary conditions on the axis. But since the calculation is limited by resolution, Newtonian nature of the code, and neglecting of magnetic fields anyway, this should be regarded as a great success of the cylindrical grid method. Another visualisation technique was applied for Fig. VI.8. Here, three density windows are shown, red again highlights the bow shock, yellow an intermediate density regime, which should be found in the shocked cluster gas, and blue a density range more typical for shocked jet plasma mixed with shocked cluster gas. The volume is cut in the middle, and the upper half is removed, similar to a baguette. One can see that higher density regions are embedded into lower ones. The central region is filled with a blue region, material, which is quite fuzzy and well transparent further out.

The emission due to bremsstrahlung was computed according to equation (V.1), mapped onto a Cartesian grid, and integrated radially (this means a Cartesian coordinate perpendicular to the jet axis) and axially. The result is shown in Fig. VI.6 (bottom) and Fig. VI.7, respectively. In the radially integrated picture, an artefact of the procedure is visible. Since the corners of the box, outside the embedded cylinder, were set to a constant low emissivity, the cluster atmosphere has lost its spherically symmetric shape. Along the line $R = 0$, the profile is correct. In both cases, so-called X-ray cavities are apparent. Where the jet has displaced the cluster gas, the X-ray emission due to bremsstrahlung is diminished. At the edges of the bow shock, an X-ray excess is visible. Fig. VI.7 shows the emission of a system, where the jet points towards the observer. Here a ring of enhanced X-ray emission can be seen with a very dominant X-ray cavity in the center. If such a cavity could be detected in observations depends on how good the quasar, which is dominant there, can be subtracted from the surface brightness profile. Around the ring a second low surface brightness region is found with a further ring of enhanced emission. The two rings arise from the two bow shock phases: At the time shown, the blastwave phase still has its bow shock further out than the one from the cigar phase. At later times, it can be expected that the cigar phase shock moves outwards, and merges with the part remaining from the blastwave phase. At earlier times, one would see only an outer ring from the blastwave phase. Interestingly, the ring is not uniform at all. Given the quite uniform cluster atmosphere of the simulation, one should rarely expect whole rings in nature, but rather segments.

The radially integrated emission (Fig. VI.6) also shows clear signs from both bow shock phases, blastwave and cigar phase. Furthermore, from that side one can identify the bumps in the cigar phase of the bow shock, which were caused by the wobbling of the jet head in different directions. There are some X-ray excesses within the cavity. Their shape is mainly that of a vertical line. These excesses are caused by the fingers produced by the KH instability. The two innermost lines correspond to the most prominent central fingers. While the simulation leaves no doubt that these features are produced at all, their shape is very uncertain given the small diameters of the fingers and their unphysical mixing with jet plasma especially in the central regions.

In all the plots in the long term evolution, the two bow shock phases are easily discernable. The inner bow shock structure is a remnant from the blastwave phase. In that phase, the radius of the bow shock should obey equation (A.8), i.e. $r \propto t^0.6$. For every hundredth timestep, the positive radial bow shock position for $\phi = 0$ and $Z = 0$ was saved, upto the final timestep 220200, corresponding to $t = 2.04$ Ma. These values are plotted over time in Fig. VI.11. The positions were fitted with a function of the type: $a + bt^c$. The fit was

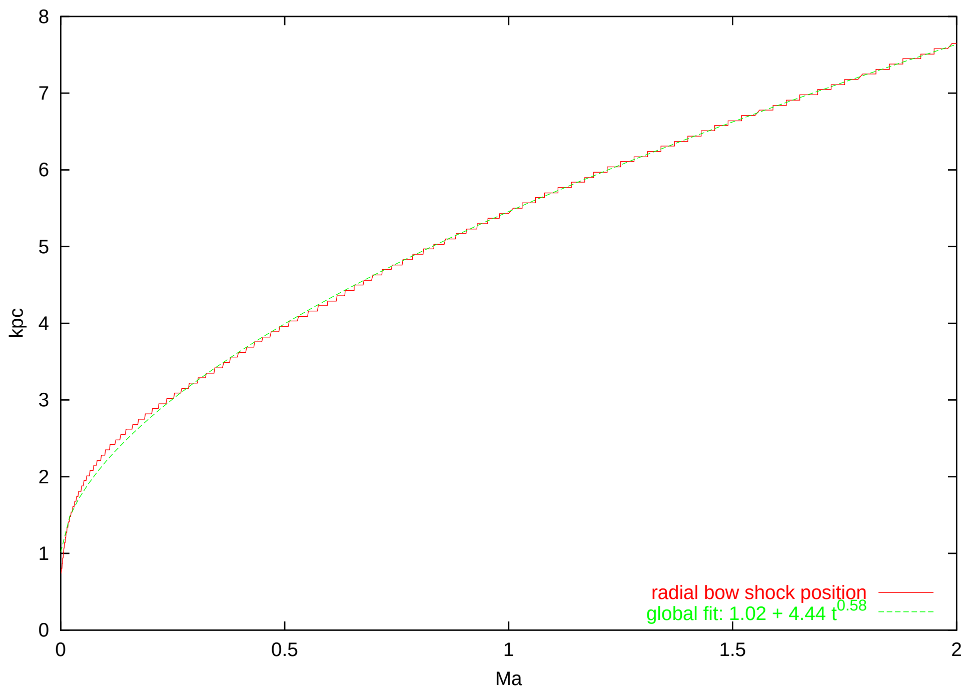

Figure VI.11: *Point, where the bow shock hits the line ($\phi = 0, Z = 0, R > 0$), with a globally fitting function.*

carried out globally, and separately for the early and the late evolution. The result is given in Table VI.3. The global fit gives an exponent c of 0.58, quite

Table VI.1: Fit parameters for the bow shock position

time range [Ma]	a	b	c
global	1.01557	4.44055	0.57641
[0:0.5]	0.413094	4.51655	0.380768
[1:2]	1.25306	4.21154	0.600992

close to the exponent analytically derived for the blastwave phase (0.6). The exponent is related to the assumption of constant thermal energy supply (compare equation A.4). Hence, an exponent lower than 0.6 means in principle, that on average the fraction of kinematic jet luminosity converted to heat decreases with time. However, the behaviour is quite different at late times compared to the early evolution. At late times, the exponent is astonishingly close to 0.6, whereas for the early evolution, c is close to 0.4, which is the value expected for the supernova case (initial energy input with no additional supply, compare A.6). This comes from the initial conditions of the simulation: in order to get a propagating jet, one has to start with a short propagating jet. The energy of that initial jet is quite high. It can be estimated by calculating the energy stored in the initial injection box: $E_0 \approx \pi R_\mathrm{j}^2 h \rho_\mathrm{j} v_\mathrm{j}^2$, where h is the height of the the cylindrical region. This amounts to approximately 10^{57} erg. The energy is also given by the parameter b, according to equation (A.6), and since the density is known:

$$E_0 = 2.35 \times 10^{80} \rho_0 b^5 \approx 10^{58}\,\mathrm{erg}. \tag{VI.3}$$

The difference of a factor of ten could be attributed to an increased heat production in the very early evolution, where the unphysical initial condition, which is always present in such simulations, relaxes into a regular jet structure. The normalised differences of the fits for the early and the late evolution are given in Fig VI.12. For the early phase fit, the deviation from the measured values is in the percent regime for the time between 0.01 Ma and 0.5 Ma. Prior to that the fit worsens. Looking at the contour plots for that time (Fig. VI.2), one recognises that the jet first develops a bow shock feature, before the beam propagates at all. Thus, at that time a hot thermal bubble develops with an infinite reservoir of energy. From Fig. VI.12, this phase should be finished by $t \approx 0.01$, which is in agreement with Fig. VI.2, where the jet is seen really to get started around that time. The anomalous initial behaviour is also responsible for the differing a parameter of the fits: Since the jet radius is 0.55 kpc, one should have expected the offset to be not too far from that value. The fit for the late evolution, adapted to $t = (1-2)$ Ma, is a good approximation down to $t = 0.5$ Ma. This indicates that at this point the constant energy injection begins to dominate over the startup energy. From the b parameter of the late evolution, one can calculate the jet luminosity, according to equation (A.8):

$$L_\mathrm{kin} = 2.23 \times 10^{67} \rho_0 b^5 \approx 3.75 \times 10^{45}\,\mathrm{erg}. \tag{VI.4}$$

Approximately 60 % of the kinetic jet luminosity are not converted into heat.

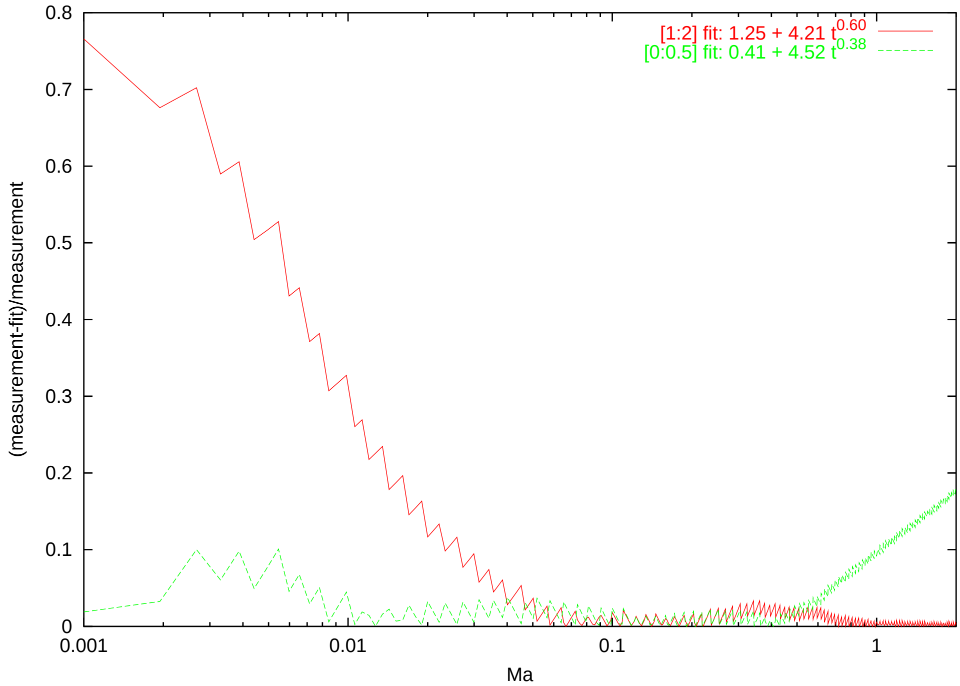

Figure VI.12: *Normalised deviation of fits on the measured points of Fig. VI.11 adapted to the regions [0:0.5] and [1:2].*

This energy is lost, mainly in shock regions due to numerical effects. (In chapter VII, the resolution is high enough so that an accurate energy measurement can be made.) While this is also the location, where a real jet will lose its energy, the amount is higher than what one would expect from synchrotron radiation. One should also expect that the exponent and the luminosity measured by the above method increase slightly in time due to the decreasing density profile, according to the analytic approximation. This effect was not yet seen in the simulation. This energy deficit could be responsible for the early start of the cigar phase: More pressure within the bubble would drive stronger oblique shocks into the beams, and impede their acceleration. The pressure within the bubble is given by:

$$p \propto \frac{L_{\mathrm{kin}} t}{V} \propto t^{-0.8},$$

where V is the volume of the bubble. So, at some certain time, the conditions for acceleration are fulfiled. From that time on, the jet creates additional volume with the newly formed cigar. Consequently, the pressure decreases further, which leads to weaker oblique shocks in the beam. Clearly, this is a runaway process. This explains, why the bow shock is not elongated smoothly, but shows a break. The acceleration is stopped, when the radial Mach number of the oblique shocks reaches unity, since disturbances have to travel at least with the speed of sound.

In reality, all the energy that is not radiated away, is available for blowing up the bubble. Hence, the bubble size is a direct indicator of the energy content, if the density is known. It was shown that any measurable deviation from the $r \propto t^{0.6}$ law is due to numerical problems in the early phase. Summarising, we have the following situation: When the jet starts, it produces a spherical bow shock. At that time it prints an identity card, containing date of birth, luminosity, and useful limits on almost any other interesting quantity. This information is transported outward with no loss of accuracy, as long as the $r \propto t^{0.6}$ law holds. The simulation shows that the law holds for the radial extention, which is the only dimension that is not affected by projection effects at all, even if the jet develops a considerable cigar, which is a clear deviation from the assumed symmetry. Cioffi and Blondin (1992) have pointed out that for a cylindrical cocoon, $r \propto t^{0.5}$. Hence,as long as the shock remains supersonic, the worst case that can ever happen is that the exponent falls to 0.5, if the symmetry of the system becomes dominantly cylindrical (of course greater galactic events like e.g. mergers are excluded from this statement). For a power law density decline with an exponent of two, it is shown in the appendix, that the exponent for the blast wave radius can increase up to one. However, with realistic core radii, the assumption of the $r \propto t^{0.6}$ law should be justified for most practical purposes. This kind of analysis has an enormous predictive power for every interesting quantity of any jet system, meeting the mentioned requirements, as will be demonstrated below.

VI.4 Comparison to Observations

VI.4.1 Cygnus A

The Chandra and VLA observations of Cygnus A are shown in Fig. I.3 and Fig. I.1, respectively. So far, there are not many radio galaxies, where the X-ray emission is so well observed as in Cygnus A. The X-ray emission clearly shows the cavity, and the bright rim of the bow shock, which was already predicted by Clarke et al. (1997). This picture shows many of the features dicussed so far, especially in the present chapter. VLBI observations point to a large inclination for Cygnus A (Krichbaum et al., 1998), greater than eighty degrees. Therefore a comparison to the contour plots of this work should be accurate. In the following, additional evidence will be given for an orientation of the jets perpendicular to the line of sight.

Since the bow shock is clearly detectable in the Chandra observation, one can measure the aspect ratio. Taking the diameters, it evaluates to 1.3. The aspect ratio is directly coupled to the density contrast (see chapter IV and Fig. IV.4). Hence, η should be in the range between 10^{-3} to 10^{-2}. With the simulation result from this chapter, an even better determination is possible. The observation shows that the bow shock is mainly in the blastwave phase. Only on the west side, the start of the cigar phase is visible. Consequently, the east side is completely in the blastwave phase, which gives more accurate η measurements. The aspect ratio of the left jet (using radii) alone is 1.2. Fig. IV.4 tells us immediately that η in Cygnus A is between 10^{-4} and 10^{-3}.

This is the effective η. If the bulk flow would be relativistic, η would be even lower by a factor Γ^2, where Γ is the bulk Lorentz factor.

From the dynamical point of view, the jet in Cygnus A, with the right-hand side just starting the cigar phase, is in a state slightly younger than the jet that is shown in Fig. VI.3. The time for that snapshot is 0.32 Ma and the bubble diameter is approximately 10 kpc. This is in strong contradiction to the estimated age for Cygnus A of ≈ 10 Ma and a source diameter of 158 kpc (Carilli and Barthel, 1996)! Hence, one or more of the parameters assumed for Cygnus A so far are wrong.

Could the difference of the extensions, from the core along the beam to the tip of the bow shock, between the left and right side be due to a relativistic inclination effect? If the inclination were as low as 45°, the far tip would be 112 kpc further away from the observer than the near tip. Light would need 0.36 Ma for that distance. From the derived η, the jet moves maximally at a few kpc/Ma, indicating that during the time in question, the jet could move approximately 1 kpc. But the tip of the right bow shock has advanced ≈ 20 kpc further than the left-hand one (assuming the inclination of 45°). Hence, the jet in Cygnus A is intrinsically asymmetric. If the jet really had an inclination of 45°, one should expect to see a ring-like structure from the small cigar of the right jet (compare Fig. VI.7). The fact that no sign of that is visible argues for a high inclination close to 90°. The western jet has advanced approximately 10 % further, than the other one. This is less than what is found in the simulation. As was pointed out above, this does not indicate different environmental densities on both sides, because the propagation speed is dominated by the dynamics within the bubble. Since the simulation shows that density differences are amplified, the smaller differences in Cygnus A compared to the simulation point to a very symmetric density profile, which is also confirmed by the measurements outside of the jet bubble (Smith et al., 2002). It seems unlikely that the start of the cigar phase is caused by a density drop at the current position of the bow shock, since in that case both sides should be affected. Therefore the mechanism should be quite similar to the one found in the simulation shown above.

The bow shock in Cygnus A has just left the blastwave phase. The results from the simulation above show that the blastwave equations are applicable for the radial expansion also for a considerable time after the beginning of the cigar phase. So, one can safely apply the blastwave equations from the appendix to the radial expansion in Cygnus A. The radial extension of the bow shock in Cygnus A is 61 kpc. The detailed analysis of the Chandra data show that the bow shock heats the cluster gas, which has a temperature of $T_0 = 5.8 \times 10^7$ K before the encounter, to $T_1 = 7 \times 10^7$ K. Standard shock jump conditions would determine the bow shock velocity to 2.3 kpc/Ma, for a strong shock. The sound speed behind the bow shock is given by $c_\mathrm{s} = 1.2 \times 10^{-4}\sqrt{T/\mathrm{K}}$ kpc/Ma. For the bow shock in Cygnus A, a sound speed of 1 kpc/Ma is derived, leading to a Mach number of 2.3. Therefore the bow shock can not be treated by the strong shock limit. From the equations for a hydrodynamic weak shock with considerable pre-shock pressure (e.g. Dopita and Sutherland, 2002), one can derive the following equation for the shock velocity v_s:

$$v_\mathrm{s} = \zeta\sqrt{\frac{k_\mathrm{B}T_0}{6\mu m_\mathrm{H}}} \tag{VI.5}$$

$$= 0.204\sqrt{T_0/5.8\times 10^7\mathrm{K}}\zeta\mathrm{kpc/Ma} \tag{VI.6}$$

$$\zeta = \sqrt{(11T_1/T_0-4)+\sqrt{(11T_1/T_0-4)^2-48T_1/T_0}}. \tag{VI.7}$$

μ is the number of particles per proton, which is two for a completely ionised medium. For the given values of the temperature jump, one can figure out $v_\mathrm{s} = 1.35$ kpc/Ma. The main source of error for this number is the shock temperature, which can be regarded as an uncertainty of the function ζ. ζ is shown in Fig. VI.13. A lower limit for ζ is $\sqrt{8}$ for a vanishing temperature

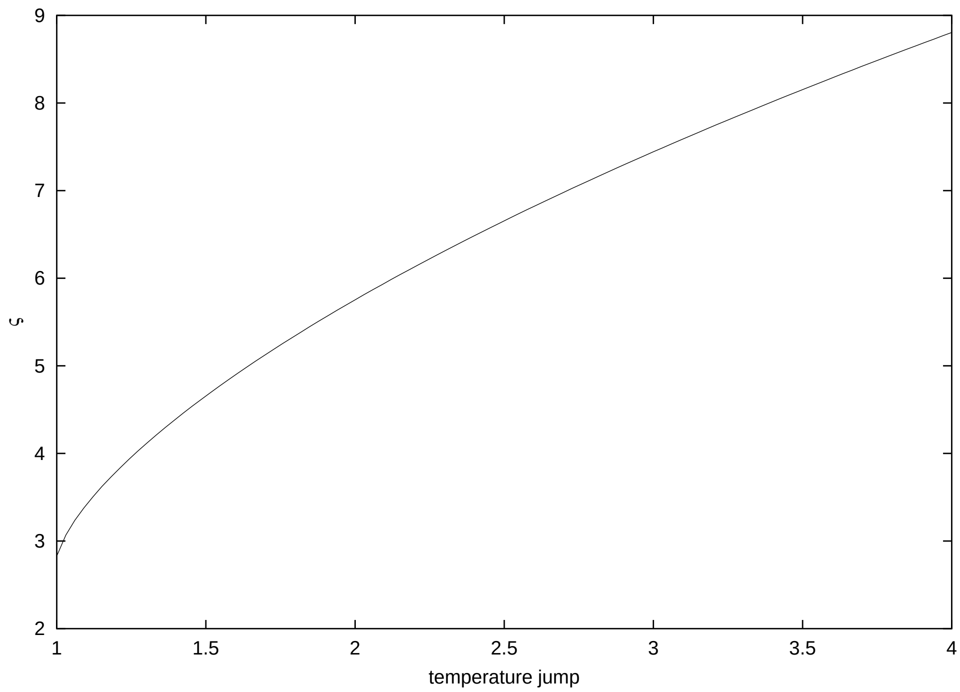

Figure VI.13: *The function ζ over the temperature jump T_1/T_0*

jump ($T_1/T_0 = 1$). However, this is inconsistent with the data in Cygnus A since there is a temperature jump, and the shock velocity has to be at least the speed of sound. Therefore 1 kpc/Ma is the lower limit for v_s. The observations limit the temperature jump to $T_1/T_0 < 4$, which leads to $\zeta < 8.805$, and an upper bound for the bow shock velocity of $v_\mathrm{s} = 1.8$ kpc/Ma Inserting radius and velocity into equation A.9 gives a relation for average density and kinetic jet luminosity:

$$L_\mathrm{kin} = \left\{\begin{array}{c} 22.5 \\ 9.49 \\ 3.86 \end{array}\right\} \times 10^{72}\frac{\rho_0}{\mathrm{g\,cm^{-3}}}\,\mathrm{erg/s}, \tag{VI.8}$$

where the upper (lower) number is for the upper (lower) limit for the velocity.

The measured electron density at the location of the bow shock is $\approx 0.01\,\mathrm{cm}^{-3}$, rising inwards to $\approx 0.03\,\mathrm{cm}^{-3}$ at a distance of 54 kpc from the core (Smith et al., 2002). How the density distribution was before the encounter with the bow shock, cannot be measured, and inside of 54 kpc no data points exist. However, the profile is not expected to steepen by much in the interior. Therefore, an average number density of $\approx 0.05 \pm 0.02\mathrm{cm}^{-3}$ is probably reasonable. The conclusion is that the average kinetic jet luminosity in Cygnus A is:

$$L_{\mathrm{kin}} = \left\{ \begin{array}{c} 26.3 \\ 7.94 \\ 1.94 \end{array} \right\} \times 10^{46} \mathrm{erg/s}. \tag{VI.9}$$

The upper and lower numbers are for the extreme values for both, density and velocity. The total radio power of the source is (Carilli and Barthel, 1996): $L_{\mathrm{radio}} = 1.2 \times 10^{45}$ erg/s. The observed radio emission is therefore between 0.5 % and 6 % of the total kinetic jet luminosity. Hence, the radiation losses are negligible for the dynamics, which is a necessary requirement for the treatment in this section.

The age of the jet can be computed easily from equation (A.10). It follows:

$$t = \left\{ \begin{array}{c} 20 \\ 27 \\ 37 \end{array} \right\} \mathrm{Ma}, \tag{VI.10}$$

where the prefered value, the upper and lower bounds for the jet velocity have been applied. The maximum synchrotron age for Cygnus A is 6 Ma. This is in clear conflict with the derived values of this chapter, and it can be safely concluded that the synchrotron age in Cygnus A has nothing to do with the true age of the jet. Therefore, the synchrotron electrons have to be reaccelerated in the cocoon, or the magnetic field has to be considerably below the equipartition values. Evidence for reacceleration has also been found in other sources (Alexander, 1987).

Concerning the shape of the radio cocoon in Cygnus A, there is also a clear conflict with the simulation results: The elongated cocoon structure wrapped cylindrically around the beam is reached in the simulation only long after the cigar phase has started. Beforehand, the cocoon fills a spherical volume. In Cygnus A, the left-hand side has not yet developed a cigar. Hence, according to the simulation the cocoon should have a spherical shape. Cygnus A is well observed down to the lowest radio frequencies, and it has been found that the cocoon has the same cylindrical structure down to the core (Carilli et al., 1991). An explanation for the observed cocoon shape could be that the jet cocoon is indeed not dominated by magnetic fields, and that the resolution of the simulation was not yet enough to get the correct cocoon behaviour. A resolution study in that density regime is with present computers impossible in 3D. The 2D high resolution study in chapter VII gives a hint how the simulation of this chapter may look at higher resolution. The results in that chapter give cocoon shapes more compatible with the observation. Hence, it is not impossible that the dynamics in the Cygnus A jet is not dominated by magnetic fields. Magnetic fields are well-known for their ability to confine jet cocoons (compare introduction). Carilli and Barthel (1996) point out that an ad hoc model, using magnetic fields in the cocoon of 17μG, three times below equipartition, implying a synchrotron age of 30 Ma gives agreement with the available data. Kaiser and Alexander (1999) fit the radio spectra applying their semi-analytic hydrodynamic model with a kinetic jet luminosity of $L_{\mathrm{kin}} = 4 \times 10^{46}$ erg/s, and a source age of 29 Ma. That luminosity is in the favoured part of the allowed values in the model presented here. For the favoured X-ray data, a source age of 27 Ma was derived. The agreement of the models is really convincing, and gives support to the idea that the magnetic field in the cocoon is indeed 17μG. The radio cocoon in Cygnus A has a width of approximately 32 kpc. If the field was predominantly toroidal it would be 64 times higher in the jet beam. Poloidal fields would be amplified according to the volume difference, which gives a factor of 64^2. This leads to fields between 1 and 70 mG for the jet beam. The magnetic field in the jet is an important constraint on the central engine. Camenzind (1993) points out that due to the Eddington limit, a rotator of mass M_{H} can produce magnetic fields in the jet up to

$$B < 0.7\sqrt{\frac{M_{\mathrm{H}}}{10^8 M_\odot}}\left(\frac{\mathrm{kpc}}{R_{\mathrm{j}}}\right)\mathrm{mG}$$

Therefore, one has to postulate a rotator of at least $10^9 M_\odot$ at the center of Cygnus A. Since this rotator has to be stable for about 30 Ma, this can only be a black hole with the present knowledge of astrophysical objects. However, central black hole masses rarely exceed $10^{10} M_\odot$. Therefore, the field in the jet beam should not amount to more than 10 mG.

The parameters can be constrained further, using the relativistic equations for the density contrast and the jet luminosity. Scheck et al. (2002) point out that in the case of a relativistic jet, η in equation (I.2) has to be replaced by

$$\eta_{\mathrm{R}} = \frac{\rho_{\mathrm{j}} h_{\mathrm{j}} \Gamma^2}{\rho_0 h_0}. \tag{VI.11}$$

Γ is the bulk Lorentz factor, and h denotes the relativistic enthalpy, which is a measure for the heat content. They also give the luminosity that can be extracted from the beam:

$$L_{\mathrm{kin}} = 2\pi R_{\mathrm{j}}^2 \Gamma (h_{\mathrm{j}}\Gamma - 1)\left(\rho_{\mathrm{j}} c^2 + \frac{B^2}{8\pi}\right)\beta_{\mathrm{j}} c, \tag{VI.12}$$

which was extended to include the magnetic field B. Dividing these two equations by one another, and using $h_0 = 1$ leads to:

$$\frac{L_{\mathrm{kin}}}{\pi R_{\mathrm{j}}^2 \rho_0 \left(\eta_R + \frac{B^2\Gamma^2}{8\pi\rho_0 c^2 h_{\mathrm{j}}}\right) c^3} = \beta_{\mathrm{j}}\left(1 - \frac{1}{h_{\mathrm{j}}\Gamma}\right) \equiv \chi \tag{VI.13}$$

The theory of relativity requires the right hand side of equation (VI.13) to take only values below one. For a highly relativistic jet, it would approach one.

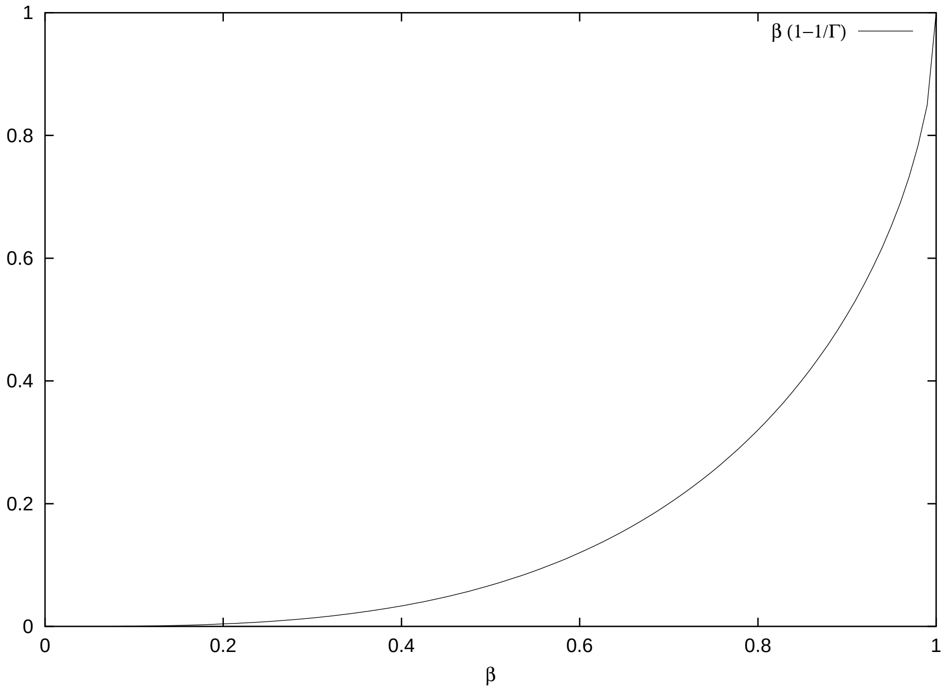

Figure VI.14: *Right hand side of equation (VI.13) (χ) over β.*

The function is plotted in Fig. VI.14. With the measured factor $L_{\rm kin}/\rho_0$ (see above), one arrives at the constraint:

$$\eta_{\rm R} + \frac{B^2\Gamma^2 h_{\rm j}}{8\pi\rho_0 c^2} > 0.02\left(\frac{L_{\rm kin}/\rho_0}{10^{73}\,{\rm erg\,cm^3\,g^{-1}\,s^{-1}}}\right)\left(\frac{0.55\,{\rm kpc}}{R_{\rm j}}\right)^2 \tag{VI.14}$$

Clarke et al. (1997) have argued that the true jet radius should be three to four times the observed jet radius in order to have a stable beam for the observed distance. With that radius, equation (VI.14) would be satisfied without need for a magnetic field. If the true beam radius would be the observed radius the magnetic field would dominate over $\eta_{\rm R}$ by a factor of at least 10. Since Cygnus A was studied extensively, and no sign of a broader beam could be found, in the following it will be assumed that the observed beam radius is really the true beam radius. Hence, $\eta_{\rm R}$ in equation (VI.14) will be neglected. With that assumptions one can easily compute the bulk Lorentz factor:

$$\Gamma = 4.6\left(\frac{n_0}{0.03\,{\rm cm^{-3}}}\frac{1}{\chi h_{\rm j}}\right)^{1/2}\frac{1\,{\rm mG}}{B} \tag{VI.15}$$

Assuming the highest possible magnetic field (10 mG), one determines a hard lower limit of the jet velocity to $v_{\rm j} = 0.6c$, but it is probably higher. Using these results, one evaluates the jet density to:

$$\rho_{\rm j} \;=\; \chi\eta_{\rm R}\rho_0/\Gamma^2$$

$$\rho_{\mathrm{j}} = 2.16 \times 10^{-30} \left(\frac{\eta_{\mathrm{R}}}{10^{-3}}\right) \left(\frac{10^{73}\,\mathrm{erg\,cm^3\,g^{-1}\,s^{-1}}}{L_{\mathrm{kin}}/\rho_0}\right) \left(\frac{R_{\mathrm{j}}}{0.55\,\mathrm{kpc}}\right)^2 \times \left(\frac{B}{1\,\mathrm{mG}}\right)^2 h_{\mathrm{j}}\chi\,\mathrm{g\,cm^{-3}}.$$

Using the extreme values, one can restrict the beam density to $\rho_{\mathrm{j}} \in [5 \times 10^{-33}, 6 \times 10^{-28}]$.

Beam temperatures are typically between 10^{12} and 10^{13} K, which is not only found in the Newtonian calculation of this work but also for relativistic jets (Scheck et al., 2002). The typical value for the dynamically important parameter $\tilde{\beta} \equiv 8\pi p/B^2$, where p is the pressure, and B the magnetic field, evaluates to:

$$\tilde{\beta} = 0.05 \left(\frac{T}{5 \times 10^{12}\,\mathrm{K}}\right) \left(\frac{10^{73}\,\mathrm{erg\,cm^3\,g^{-1}\,s^{-1}}}{L_{\mathrm{kin}}/\rho_0}\right) \left(\frac{R_{\mathrm{j}}}{0.55\,\mathrm{kpc}}\right)^2 \left(\frac{\eta_{\mathrm{R}}}{10^{-3}}\right) h_{\mathrm{j}}\chi \left(\frac{m_{\mathrm{p}}}{m}\right),$$

where m is the electron or proton mass for a positronic or protonic jet, respectively. Therefore, if the jet in Cygnus A were an electron-proton jet, it would be magnetically dominated. For an electron-positron jet, $\tilde{\beta} = 92$. For a magnetic field to have significant effect on the jet dynamics, $\tilde{\beta}$ has to be below 10 (e.g. Lind et al., 1989). Hence, an electron positron jet would have negligible magnetic fields. In that case, the magnetohydrodynamic approximation would be no longer justified (compare section II.1). If the jet beam could somehow be proved to carry dynamically significant magnetic fields or not, it would be possible to discern an electron-proton from an electron-positron jet. At this point, the first alternative is preferable, because stability in this source is a critical issue. Dynamically significant magnetic fields favour stability.

Clarke et al. (1997) have argued that the density contrast should be as low as 10^{-6}, in order to explain the large cocoon width. With the present knowledge, the argument can no longer be held. Since before the present work jets were only known in the cigar phase, the argument refered to that phase. With the new Chandra data showing that the left jet is in the newly discovered blastwave phase, the argument is reversed: Now we need something to confine the cocoon, no additional low density contrast effects to widen it! The parameters derived for Cygnus A from the present model, together with an estimate taking also the other mentioned models into account are given in Table VI.2.

Why does the model fail?

With the literature parameters for Cygnus A, the hydrodynamic model predicts long cigars for the time at which the source is observed, which are not seen. An exact theory relating the onset of the cigar phase to some basic parameters could not be derived so far. However, the relevant parameters for the bubble expansion are kinetic jet luminosity and external density. The kinetic luminosity in the model was 1×10^{46} erg/s. A true luminosity of at least twice this value was derived. However, increasing the luminosity could turn the system in

Table VI.2: Parameters for Cygnus A

Quantity	derived value	best guess
kinetic jet luminosity (L_{kin})	$(8\pm^{18}_{6}) \times 10^{46}$ erg/s	$(7 \pm 4) \times 10^{46}$ erg/s
density contrast (η_{R})	$10^{-3.5\pm0.5}$	10^{-3}
dynamic age	$(27\pm^{10}_{7})$ Ma	(28 ± 2) Ma
jet velocity (v_{j})	$> 0.6c$	$> 0.9c$
bulk Lorentz factor	$1.3 < \Gamma < 10.6$	5
jet density ($\log(\rho_{\mathrm{j}}$ / g cm^{-3}))	-29.8 ± 2.5	-30
radio luminosity fraction ($L_{\mathrm{rad}}/L_{\mathrm{kin}}$)	(3.25 ± 2.75) %	(4 ± 2) %
magnetic field in the jet	1-10 mG	$1 - 3$ mG
$\tilde{\beta} = 8\pi p/B^2$	$\approx 10^{0\pm2}$	0.1
jet constituents		electrons & protons

the wrong direction, since also the jet thrust would be increased, and the cigar would probably be created even earlier. An alternative seems to be a different density distribution. In chapter VII it is shown that for a more centrally concentrated profile, a lower density contrast and a higher jet luminosity, the cigar start radius could be considerably larger (although not as large as in Cygnus A). However, the situation is inconclusive. Understanding of this feature is likely to constrain the parameters of Cygnus A even more.

VI.4.2 Abell 2052

An important prediction of the model presented above is that in some sources, where the inclination is low, a second X-ray ring should be visible, if the central quasar light could be subtracted properly. Astonishingly, such secondary rings have been detected in Abell 2052 and Messier 87.

Blanton et al. (2001) have recently imaged the central region of the cluster Abell 2052 at $z = 0.03$ with Chandra. There, the powerful radio galaxy 3C 317 is located. The X-ray image shows two rings of enhanced emission. This is exactly, what is predicted by the above model, if the cigar has already been started for a while (compare Fig. VI.7). Hence, the prediction is confirmed by the observation. With the interpretation for the X-ray rings at hand, one could derive a lot of parameters for the source in a similar way like in Cygnus A. Since the space here is limited, only the most interesting aspects will be discussed. From the ratio of the elliptical axis, the inclination of the system is easily computed. Measurement with a simple ruler placed by eye on the published image resulted in an inclination of 37° for both rings, also consistent with the shift of their centers against each other. The agreement of this number is further evidence for this interpretation of the X-ray structure. This is consistent with the fact that the outer ring is broader at the expected location, and narrower at

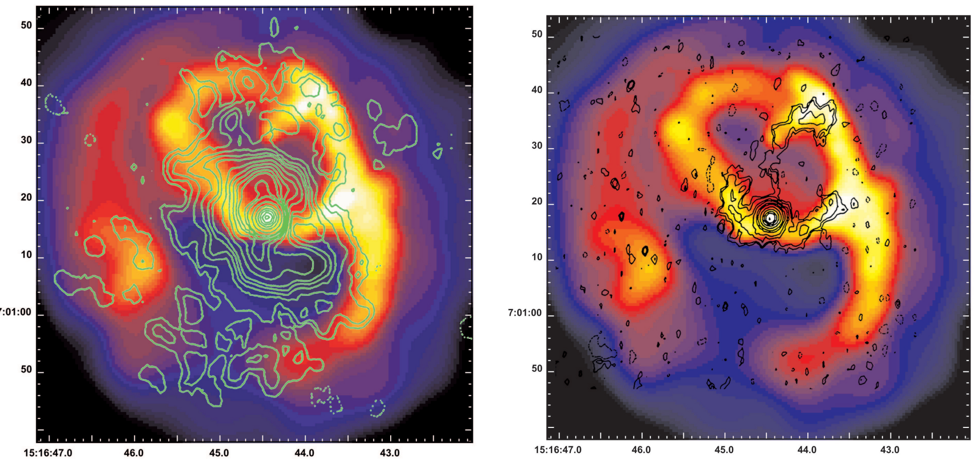

(a) (b)

Figure VI.15: **a**: *X-ray image of the center of the cluster Abell 2052 where the radio source 3C317 is located. The countours are the 6cm radio emission.* **b**: *The same as b with H α and [N II] contours. Images from Blanton et al. (2001).*

the right places with 90° separation from the broad locations, further confirming the above interpretation. The term *outer ring* is used here for the outer ring in the observation. In reality, the material of the inner ring can extend to larger spherical radii than that of the outer one. At the redshift $z = 0.3$ for the source, one arcsecond corresponds to 0.8 kpc, again for a Hubble constant of 65 km/s/Mpc. The diameter of the outer ring is 65 arcsec, and that of the inner one is 35 arcsec. This corresponds to 52 and 28 kpc, respectively. Since the structure is cylindrically symmetric, and no projection effects apply, these are the true radii for the two phases of the bow shock. Since the inner ring is not broadened, at the angle, where the outer one is, the cigar cannot be very elongated. Although detailed analysis of how the cigar looks at different sizes for different inclination angles was not performed so far, it is clear that the length of the cigar will not greatly exceed its width, leading to total true maximum source diameter of 80 kpc. Hence, the light travel time through the system is of the order 0.3 Ma. If the advance speed of the jet head would be similar to Cygnus A, it would move less than a kpc during that time. The sideways expansion would be even less. Therefore, if the system was symmetric, a third X-ray ring should be well visible with a diameter of the order 25 kpc. The conclusion is again, like in Cygnus A that the system is asymmetric (if there cannot be found a clever way, how the emission from the third ring could be absorbed). If Cygnus A could be observed with a similar inclination like 3C317, it would show two rings with approximate diameters of 120 and 40 kpc, respectively. There is a factor of two between the ring radii ratios, but the absolute size of the smaller ring is even greater in Cygnus A. The inner ring is not part of the self similar evolution of the bow shock. This is evident, since there is no such ring in the early evolution. Hence, every inner ring starts at a certain point in the jet evolution with radius zero, expanding with typically low Mach numbers. Since the Mach number is determined by the temperature, which is quite similar in low redshift clusters, comparisons should be made with absolute sizes of the inner rings. Therefore, the conclusion that 3C317 has just started one of its cigars, and is intrinsically very similar to Cygnus A is further supported. Evidence for the low Mach numbers for the expansion of the inner ring comes from the fact, that the inner ring is traced by the emission lines of Hα and [N II]. This shows that they are shock excited. As Blanton et al. (2001) point out, a Mach number below six has to be concluded. Besides at the ring, there is one interesting emission line region extending from the upper edge of the outer ring, which coincides with that of the inner ring at that location, down to the very center of the source with decreasing width. This is very similar to what was observed in the simulation, where the fingers of the KH instability were also shown to be strongest in the center of the grid. Note that for reliable determination of this result in the simulation, the full computation of both jets is critical, since otherwise the artificial boundary conditions on the side of the jet inlet dominate the dynamics in the symmetry plane. This can be regarded as evidence for the hypothesis from chapter V, derived by a comparison of the masses that entrainment of shocked external gas at the cocoon boundary can produce emission line regions.

VI.4.3 Messier 87

M87 was also recently observed with Chandra. The published data (Marshall et al., 2002; Young et al., 2002) show similar rings like in 3C317. Also, they are traced well by the emission line regions of Hα and [N II], (Jester, private communication, and Young et al. (2002)). The analysis of that data was still in progress at the time of writing. Therefore the results are preliminary. Apart from the large ring, witnessing the blastwave phase also in M87, the jet beam is surrounded by two small rings (piecewise not visible). They all seem to be elongated in the same direction. The elliptical axis ratios yield an inclination of 17° for the outer ring and 26° for the better identifiable of the inner rings. The X-ray morphology in M87 is quite disturbed, probably due to the earlier activity in the system, which also seems to have happened in different directions (Klein, 1999). The inner rings are better visible, and therefore the 26° should be the better estimate. However, this is not yet the full story. The direction of shortening (position angle (PA) $\approx 250°$) is not identical to the jet direction (PA $= 291°$, Klein, 1999). The conclusion is that the jet currently does not point in the direction where it pointed to when the rings were created. The jet could be deflected somehow, but given the arc-like radio morphology downstream of knot A, it seems likely that the jet is precessing on a cone with opening angle of at least 40°. This is also a fine explanation for the shift of the two inner X-ray rings against each other. Assuming that the rings were created half a precession period ago would give a position angle of the cone of 270°. M87 has radio lobes on three different scales (Owen, 1999). Interestingly, this is exactly what Klein (1999) has determined for the intermediate age radio lobe.

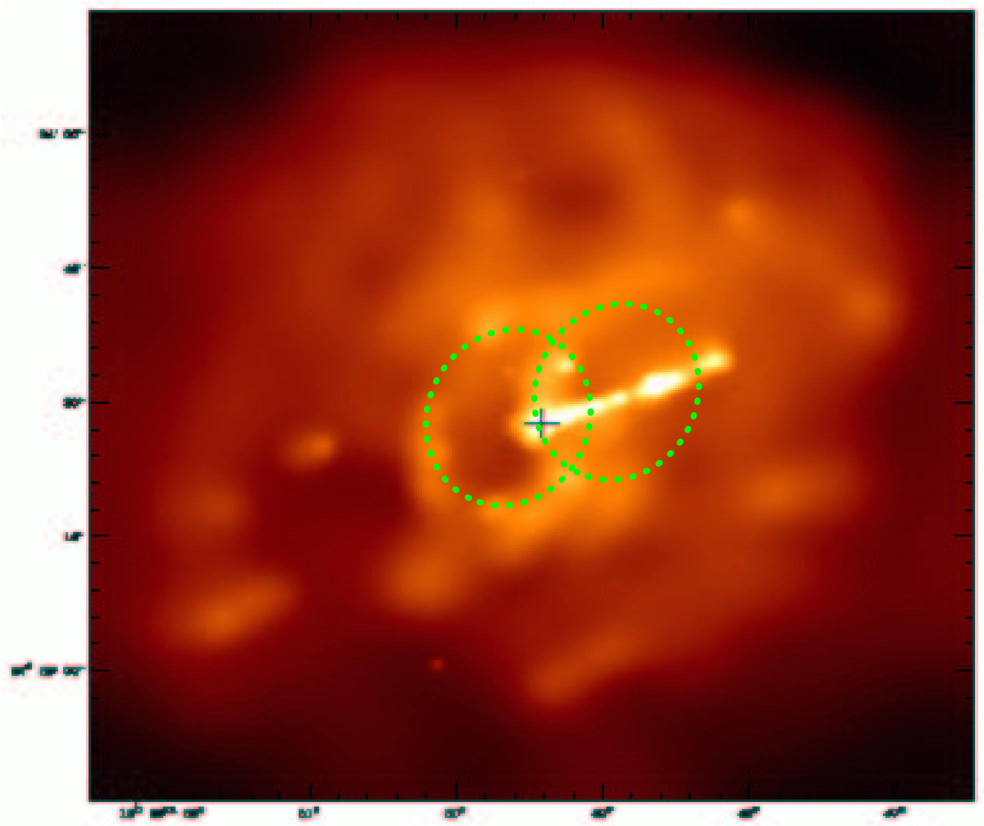

Figure VI.16: *X-ray image of the central arcminutes in M87. The jet is the bright straight line. The core is at the position of the black cross. The inner rings within the X-ray cavity are indicated by green dots. Picture adopted from Young et al. (2002)*

Therefore, an easy explanation for the innermost and the intermediate radio lobe would be, that the jet once pointed to PA = 170°, and somehow later – probably after a break in the activity – started to precess around this axis. If the jet is now at the extreme position in the cone of opening angle 40°, then its total inclination is 32°. It is interesting to estimate the precession frequency: The deprojected distance to knot A is approximately 2 kpc. The relativistic jet material needs about 6000 years for this distance. Since no bending is observed on that way, the precession has to be less that roughly one degree during that time. This gives a minimum precession period of 2 Ma. On the other hand, the jet is assumed to be about 1 Ma old, although this age is considered quite uncertain (Bicknell and Begelman, 1999). During that time the jet has to do at least half a precession period. Since the inner radio lobe is asymmetric, it has probably just done that and no more. This limits the period to not much more than 2 Ma. Adopting this as fiducial value, one can think about the origin for this precession. Camenzind (1997) gives several possible causes for black hole precession, two of which are of interest here: For a gas ring with mass M_{R} at a radius of R gravitational radii around a black hole with mass M_{H} will cause a precession period of:

$$P_{\mathrm{R}} \approx 1\mathrm{Ma}\frac{10^6 M_\odot}{M_{\mathrm{R}}}\left(\frac{M_{\mathrm{H}}}{10^8 M_\odot}\right)^2\left(\frac{R}{10^4 M_{\mathrm{H}}}\right)^{5/2}$$

For M87 a gas ring of $\approx 10^{11} M_\odot$ would be needed at parsec scale, which seems unrealistic. The other possibility is the coupling of the spin from a secondary black hole to its orbital angular momentum with respect to the primary one, which is sometimes refered to as Lense-Thirring effect. From the jet properties, one can determine an accretion rate for the outflow producing central object (Camenzind, 1999), which equals $10^{-3}\dot{M}_{\mathrm{Edd}}$, where $\dot{M}_{\mathrm{Edd}}$ is the Eddington limit for the accretion rate of the big black hole with $3 \times 10^9 M_\odot$. A companion black hole should have at least $m_{\mathrm{H}} \approx 3 \times 10^6 M_\odot$. In that case, the precession period is given by:

$$P_{\mathrm{LT}} = 2\left(\frac{P_{\mathrm{b}}}{9.3\mathrm{a}}\right)^{5/3}\left(\frac{m_{\mathrm{H}}}{3 \times 10^6 M_\odot}\right)\left(\frac{M_{\mathrm{H}}}{3 \times 10^9 M_\odot}\right)^{-1/3} Ma,$$

where P_{b} is the orbital period of the system. The gravitational radius for a $3 \times 10^9 M_\odot$ black hole in M87 is $r_{\mathrm{G}} = 4 \times 10^{14}$ cm. A period of 2 Ma would be produced by a secondary black hole at a distance of 214 $r_{\mathrm{G}} \approx 0.03$ pc. The merger time due to gravitational radiation losses for such a binary system is:

$$t_\infty = 17\left(\frac{R}{0.03\,\mathrm{pc}}\right)^4\left(\frac{M_{\mathrm{H}}}{3 \times 10^9 M_\odot}\right)^2\left(\frac{m_{\mathrm{H}}}{3 \times 10^6 M_\odot}\right) Ma.$$

A ten times bigger secondary black hole would lower the collapse timescale by a factor of forty, which is too short, given the fact that the precession is already going on for ≈ 1 Ma. If the primary black hole had a considerable angular momentum, their distance could be larger. However, the black hole spins are unknown. The latter alternative has an important advantage: It can explain the radio lobe history of M87. The following scenario is possible: 60 Ma ago, the binary separation was large. Consequently, an accretion disk was around the big black hole, producing an outflow in the direction PA $\approx 20°$. Then 20 Ma ago, the secondary black hole moved close enough to draw the accretion onto it. Now, the outflow was directed along the spin axis of the small black hole with PA $\approx 170°$. Having moved further inwards, the outflow started again 1 Ma ago, but the separation was already close enough for the Lense-Thirring effect. Since other processes cannot account for such changes in the outflow behaviour, while it is a natural consequence of the latter, one should regard this as evidence for the Lens-Thirring effect in M87. To the knowledge of the author, this is only the second case, where evidence for a Lense-Thirring effect is present.

Hence, also in M87, blastwave and cigar phase are identifiable, and the procedure demonstrated above for Cygnus A can be equally applied to that object.

Chapter VII

Bipolar Jets in 2D with Cooling

Interesting results were obtained in the simulation with substantial cooling, as well as in the one with bipolar injection. But important questions were left un-answered. One of those is the mixing, especially in the central region of the cocoon, which is the region where the emission line gas is expected. This can only be studied by a high resolution simulation. Another point was the onset of the cigar phase. Here, the energetics is followed in detail, which should provide a clue. As the comparison with observation of low redshift sources showed, a low density contrast is essential for an understanding of the shocked external medium. So, the parameters of the previous chapters were kept as guidelines for a new simulation. This simulation is now carried out in 2.5D, in order to free computational resources for cooling, resolution, and scale. The cooling process was also modified for this simulation. Since it turned out that the full cooling machinery is so CPU consuming that resolution problems are the consequence, a compromise was made, with the application of the average cooling curve for a zero metal plasma without photoionisation processes, as described by Sutherland and Dopita (1993). This approach cannot give accurate number densities for individual ions, which have now to be calculated using the collisional ionisation equilibrium, but it is still a useful approximation, if one restricts the interest to thermal and dynamical properties of the gas. In order to maximise the effects of cooling and the decreasing density distribution, a King profile with high central density and small core radius is applied. This may not produce a good prediction for any individual source, but should optimise the gain of understanding because effects will be amplified. Two runs were performed. One with emphasis on the resolution, and one with low resolution, with a long propagation distance.

VII.1 Simulation Setup

The simulations were carried out in axisymmetry on a uniform grid, spanning 120 kpc in the axial and 25 kpc in the radial direction. The jets were injected into a King cluster atmosphere (VI.1), with core radius 15 kpc and $\beta = 1$. With a probability of 10 %, the density was increased by a random factor between 1 and 1.4. No further inhomogeneity was added, since the simulation from chapter VI already showed that the dynamics within the shell develops in such a violent manner that the jets loose their symmetry without putting in large scale differences in the external medium. A passive tracer field was added. In order to study the locations of material from the left jet, the right jet, and the external medium separately, the tracer was set -1, 0 and 1, respectively. The resolution

Table VII.1: Simulation Parameters

	run A	run B
central density n_0	10 cm^{-3}	10 cm^{-3}
King exponent β	1	1
density contrast η	10^{-4}	10^{-4}
jet velocity v_j	$c/3$	$c/2$
jet Mach number M_j	10	90
jet radius R_j	0.5 kpc	0.5 kpc
kinetic luminosity L_j	1.2×10^{46} erg/s	4.0×10^{46} erg/s
resolution	5 ppb	40 ppb

was 5 ppb for the first run (A), and 40 ppb for the second one (B), where a beam radius of 0.5 kpc was applied. The runs also differ in the jet velocity, which is $c/3$ for the low resolution jet, and $c/2$ for the highly resolved one. The latter increase in jet velocity makes sure that in run A there is always less energy around than in run B, which would otherwise also be the case for most of the time, since the energy dissipation due to numerical diffusion is higher in run A. For run A, the pressure equilibrium condition was dropped, and the Mach number was set to 10, which was reached in run B behind the first shock approximately. Two jets are injected in the middle of the grid in antipodal directions, within the same cylindrical box of length $2R_\mathrm{j}$ as in chapter VI. The cooling was carried out applying the zero metals, zero field non-equilibrium cooling curve from Sutherland and Dopita (1993). This gives a fiducial lower limit to the true cooling, which may be modified by an unknown and differing amount of metals in real sources. For the evaluation of the cooling function, the ionisation is calculated in each timestep according to collisional ionisation equilibrium. This again underestimates the true abundance of coolers. In contrast to the cluster atmosphere from chapter VI, the temperature was set to 10^4 K, anywhere. This may not be realistic, but saves computational resources. Because, the cooling function is set to zero below 10^4 K, the external medium can be kept in equilibrium without introducing additional heat sources like e.g. accreting or virialised dark matter haloes or background radiation. These sources may be real, but it is beyond the scope of this work to find out the redshift dependent temperature of the background. Since the bow shock remained supersonic at any time in chapter VI the temperature of the background will not significantly influence the result, as long as it does not largely exceed 10^7 K. The main difference between the two runs remains the resolution, propagation distance, and a slight energy deficit in run A. A summary of the parameters is given in Table VII.1.

VII.2 Run B: High Resolution

VII.2.1 Energy distribution

Coloured contour plots from the results from run B are shown at three different times in Fig. VII.8, Fig. VII.9, and Fig. VII.10. The results will be first discussed, following the energy development. Let us first calculate the approximate energy in the different parts of the system. The internal energy of the undisturbed external medium is given by:

$$E_{\mathrm{int}}^{\mathrm{ext}} = \frac{3}{2}\int_V n k_{\mathrm{B}} T \, dV = 6\pi n_0 k_{\mathrm{B}} T a^3 \left[\ln\left((r/a) + \sqrt{1+(r/a)^2} \right) - \frac{r/a}{\sqrt{1+(r/a)^2}} \right].$$

For an order of magnitude estimate, it suffices to approximate the cylindrical computation volume by a sphere with radius of half the Z-axis. The result is:

$$E_{\mathrm{int}}^{\mathrm{ext}} \approx 2.8 \times 10^{58}\,\mathrm{erg}.$$

The jet beam itself would contain $\approx 2 \times 10^{60}$ erg, if it were extended all over the grid. The average head propagation speed is about 1.7 kpc/Ma per jet. Therefore, the kinetic energy stored in the jet is:

$$E_{\mathrm{kin}}^{\mathrm{jet}} \approx 4 \times 10^{58}\mathrm{erg}\left(\frac{t}{\mathrm{Ma}}\right).$$

Since the jet is supersonic, the internal energy is always less then the kinetic energy in the beam. The kinetic energy of the shocked external medium is given by equation A.5. For a homogeneous medium without cooling losses, which is the approximate situation at the beginning of the simulation, it follows:

$$E_{\mathrm{kin}}^{\mathrm{shell}} = \frac{3}{10} L_{\mathrm{kin}} t \approx 4 \times 10^{59}\mathrm{erg}\left(\frac{t}{\mathrm{Ma}}\right).$$

In cylindrical coordinates, a spherical shell contains more radial than axial kinetic energy, because of the bigger volume for the radially moving material which is located at larger cylindrical radii. Nearly everything else is stored in thermal energy of shocked gas from the jet and the external medium:

$$E_{\mathrm{int}} \approx 8 \times 10^{59}\mathrm{erg}\left(\frac{t}{\mathrm{Ma}}\right).$$

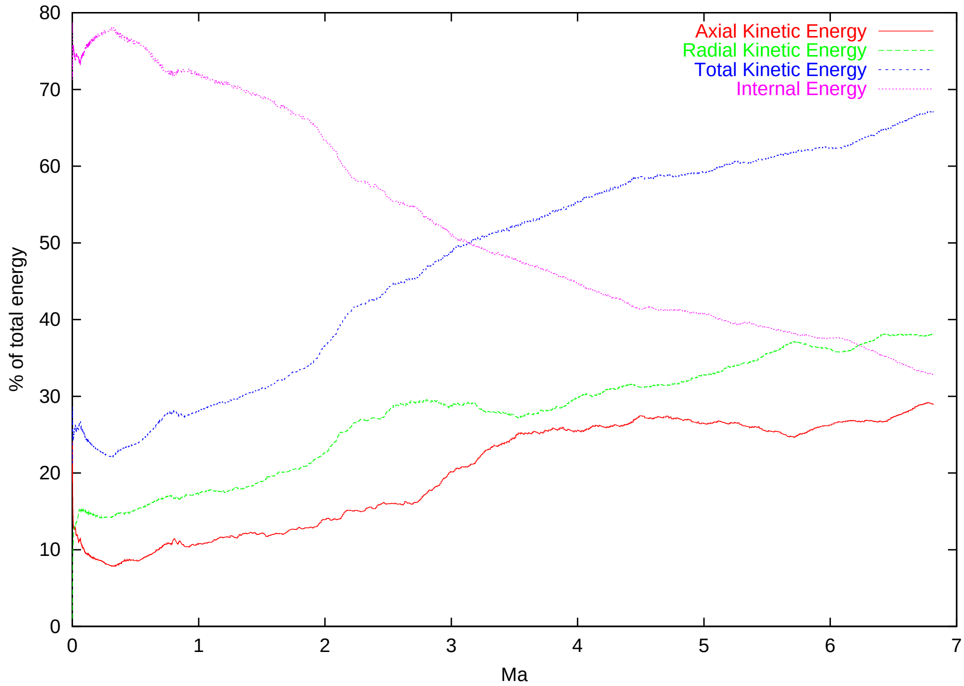

Figure VII.1: *Energy fractions over time for run B.*

How fast kinetic energy of shocked gas is converted into internal energy depends on the resolution of the simulation. It is evident from this consideration that the energy of the unshocked external medium is completely negligible. In the jet beam, a few percent of the total energy is stored. The bubble stores about ten times as much in kinetic energy and again twice as much is in the thermal energy within its belly. This is the approximate situation at $t \approx 1$ Ma, when the initial conditions have relaxed into a realistic jet. Fig. VII.1 shows that the fraction of kinetic energy begins its rise before $t = 1$ Ma. The rise is monotonic and quite drastic: At the end of the simulation ($t \approx 7$ Ma), nearly 70 % of the energy is kinetic, contrary to the starting situation, where 70 % is in the thermal energy. This tendency can be understood with the help of equation (A.5), which gives the kinetic energy fraction for power law density distributions and varying energy supply. According to that equation, a kinetic energy fraction of 70 % is reached for a density distribution declining with an exponent of 2.85 (compare Fig. VII.3). At the end of the simulation, the bow shock had advanced approximately 12 kpc in both directions. At that position, the King profile decreases with a local exponent of ≈ -1.2. So, the simulation shows the same tendency, but the effect is stronger than in the approximate analytic treatment. This can be understood as an effect of cooling: Up to $t = 2$ Ma, the kinetic energy fraction, $\approx 1/3$ at that time, is in agreement with equation (A.5), since the local King index is ≈ -0.5. Now cooling comes in its most effective phase, and most of the shocked external gas collapses to densities up to $2000\,\mathrm{cm}^{-3}$ and temperatures of in the range of 10,000 degrees. The material is compressed to a small region behind the bow shock, at $t \approx 3$ Ma. For the energy budget,

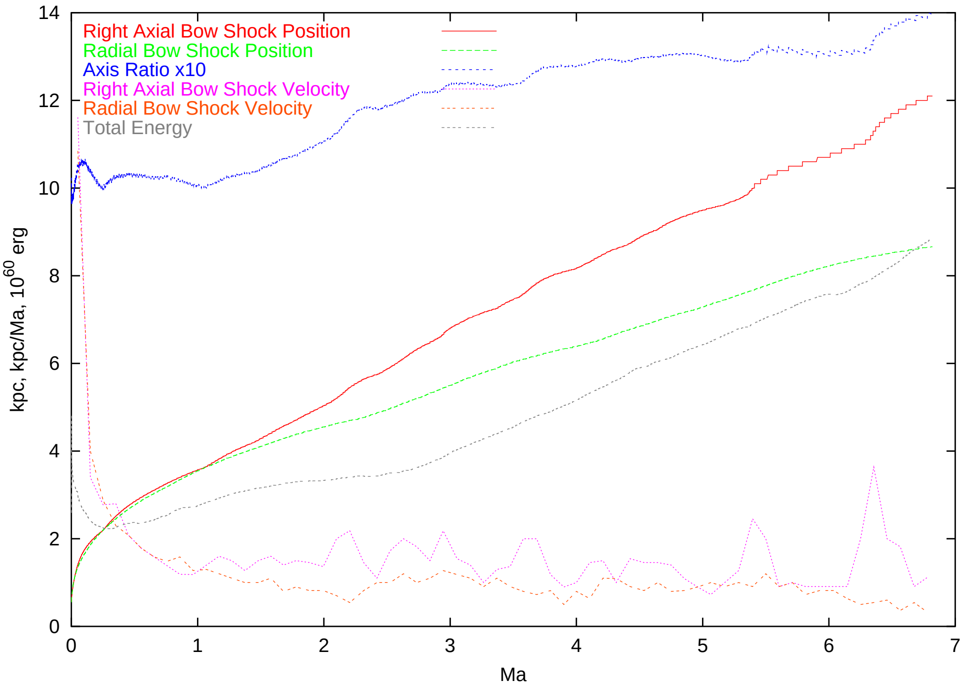

Figure VII.2: *Bow shock properties and total energy over time for run B. The values were determined every hundredth timestep, which corresponds to approximately 1000 years. For the computation of the bow shock velocities, the average over time intervals of 0.1 Ma was computed.*

this means a strong dip in internal energy, which even produces a decrease in the total energy (compare Fig. VII.2). Equation (A.5) predicts a higher kinetic energy fraction the lower the energy supply exponent. The corresponding excess in kinetic energy is evident after $t = 2$ Ma. The kinetic energy is gained totally in the radial direction. This is due to the fact, that the shocked external gas was compressed by the ram pressure of the jet head in the axial direction, anyway. Effectively, the cooling keeps some of the shocked gas at larger cylindrical radii, where it stays at the velocity of the bow shock. The increase in axial kinetic energy between $t = 2$ Ma and $t = 3$ Ma is caused by the bow shock building an extension in the radial directions (Fig. VII.9). This is a part of the bow shock that has not yet collapsed due to cooling. Between $t = 3$ Ma and $t = 6$ Ma, the total energy (Fig. VII.2) increases with the maximum possible rate of the kinetic jet luminosity. This shows that in this phase, much less gas cools than before. This is an effect of the lower density and mainly propagation velocity, which has decreased by a factor of 10 since the birth of the jet at that time. At these times, one has to expect complicated "microphysics" below the resolution limit, like self gravity, and rapid star formation.

The system seems to notice one special point. This point is at the position, where the radial kinetic energy equals to the thermal energy. Here, at $t \approx 6$ Ma, the two lines in Fig. VII.1 are just about to cross, when the radial kinetic energy turns sharply around, now decreasing parallel to the thermal energy. Then,

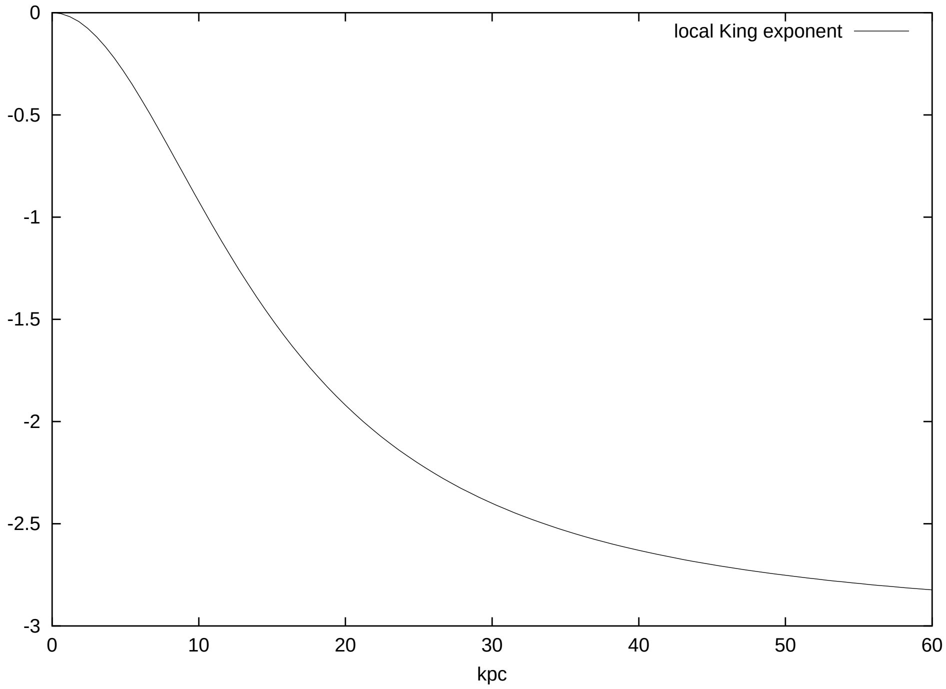

Figure VII.3: *Exponent of a local power law approximation to the King profile used for the external density distribution*

both curves make a sharp bend and finally cross. The bends in the radial kinetic energy are accompanied by bends in the axial kinetic energy curve in opposite directions. This shows a strong coherence of the system, which is not understood in detail. Nevertheless, at the same time two significant increases in the axial bow shock velocity can be observed (Fig. VII.2). These bumps could be the signs of an oscillation with increasing amplitude, leading finally to the start of a cigar phase. The colour contour plots for that era show a small extension of the bow shock near the jet head (Fig. VII.10). However, when exactly a cigar phase starts remains an open question.

VII.2.2 Morphology

Fig. VII.8 shows the jet in the early phase, where cooling has slightly affected the post bow shock gas. It is interesting to compare that picture to the lower resolution unipolar, and the 3D simulations. For similar density contrast, they showed, that the cocoon forms one big vortex for most of the time, with entrainment of shocked external material in fingers growing on their journey towards the left-hand boundary. This behaviour has been confirmed in the 3D simulation (chapter VI). The high resolution available here refines the picture. Although the jet cocoon still fills most of the space within the bubble, it is not filled in the same way everywhere. There is a large region around the plane of symmetry, which shows very strong mixing. The tracers for both jets show little amount of material there. Instead, the shocked jet plasma is concentrated in a lobe-shaped region around the head. The dynamic range of the tracers is not equal. For the left jet, the right jet, and the external medium, the tracer was set to -1, 0, and 1 respectively. For the right jet, the tracer values between $[-10^{-3}; 10^{-3}]$ were selected and squared, so that the lowest values in the plots show the highest fraction of jet material. Therefore, the right jet tracer shows only the regions with the purest jet material. Nevertheless, the right jet cocoon is in a very different state compared to the left cocoon. The left one dissolves into small vortices, wheres the right one transports the KH instabilities along its surface building one large finger at its left, that extends down to the center of the source (compare page 73). The fact that these two modes arise in the same simulation at the same time demonstrates, that the cocoon switches between them on small causes. Probably, the cause is the stochastic difference in the external medium.

At $t = 3$ Ma (Fig. VII.9), both cocoons show regions of very pure jet material only around the head regions, and more and more mixing and filaments towards the center. However, on the right side, where the prominent finger was before, the tracer takes still the higher values. Hence, there is a stronger mixing on the left side. The bow shock has now mostly collapsed to a thin sheet. Only the region in vicinity to the jet head keeps a significant width and temperature. Up to that phase, the bow shock can be regarded as an entity, capable of forming a large scale absorption system. Already, the first signs of fragmentation show up.

Fragmentation has considerably changed the picture of the bow shock at $t = 6.76$ Ma. Figure VII.10 also shows much more details than the low resolution simulation (compare Fig. V.8). Several regions are compressed by a factor of approximately 1000 to almost $10^4\,\mathrm{cm}^{-3}$. A typical collapsed region is magnified in figure VII.4. The pictures show that the filaments are not only sheet-like, but the sheets contain also very condensed points that are only extended in the ϕ direction. It is very likely, that these structures would be point-like in a 3D simulation. In the middle of figure VII.4, at $(R, Z) \approx (5.6, -7.6)$, the temperature has dropped to ≈ 3000 K over a region with a diameter of 0.2 kpc. This region is surrounded by a ring of very high density. Since the cooling is switched off below 10^4 K, this low temperature could only be reached by adiabatic expansion. The region is in principle well resolved with approximately 16 points. The high density clumps have a typical mass of $10^6\,M_\odot$. This is similar to their Jeans mass, which is also not much bigger in the adiabatically expanded regions. Therefore, self-gravity becomes most important for the detailed physics of the bow shock, which will become a star forming region. This confirms the result from chapter V. Some of the entrained shocked external material has managed to form dense clumps of gas. In principle, there should be many smaller clumps of that kind throughout the cocoon. However that material could not be resolved anymore and has mixed with the shocked jet plasma. These clumps represent sites of line emission or star formation. The cocoon width at the final time is approximately $10R_\mathrm{j}$. Large cocoons of that size or even larger are required by observation. However, they should have cylindrical shape. The distribution of the right jet tracer has approximately

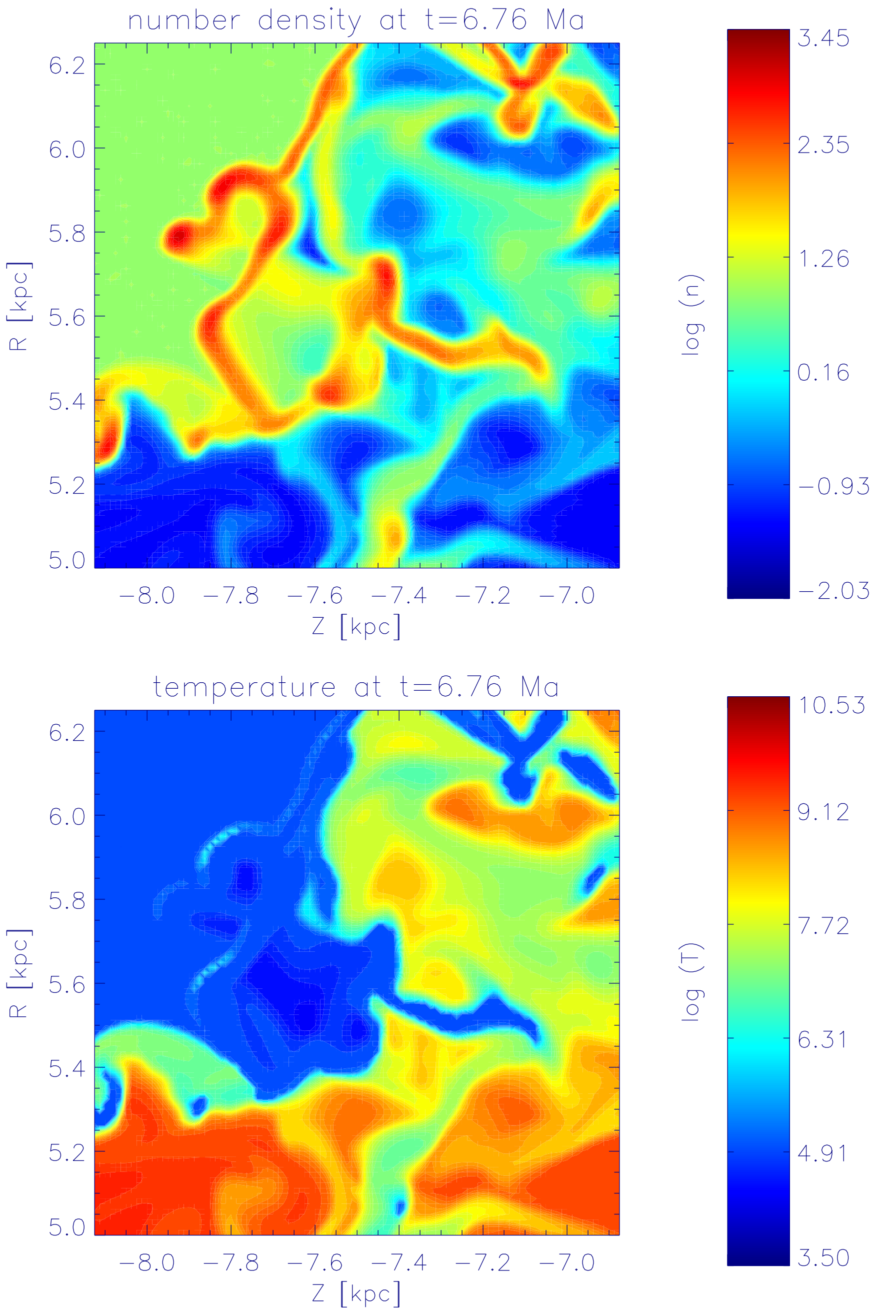

Figure VII.4: *Magnification of a fragmented region in the bow shock area.*

cylindrical shape with two vortices above. However, since only the full simulation with magnetic field and a description of the relativistic electron population could give a realistic impression of how such a cocoon would look like in the observation, the jet tracers should be only regarded as a first approximation to the morphology of the radio emission. The shape of the cocoon may still be different at higher resolution (compare Fig. III.3). However, especially the distribution the right jet tracer suggests that cocoon shapes might be explainable without the aid of dynamically significant fields there, as suggested by the results from section VI.4.1.

VII.2.3 Bow shock advancement

Figure VII.2 shows the position and current velocity of the bow shock in the radial and the positive axial direction. Since the central injection cylinder has a height of two jet radii, the bow shock starts at nearly the same position for both directions. Due to the increase in kinetic energy (see above) the bow shock accelerates. However, the average radial expansion still can be reasonably approximated by a $r \propto t^{0.6}$ law, after $t = 2$ Ma. For a determination of the errors, the bow shock is now "observed". Its basic parameters can be recalculated from the velocity and position of the radial bow shock, which would be the observed parameters: At $t = 6.76$ Ma, the bow shock has advanced for 8.6 kpc in the radial direction, and has a velocity of 0.8 kpc/Ma. Using formula (A.10), one recalculates the age of the jet to $t = 6.45$ Ma. This underestimates the true age by approximately 5 %. Assuming that the jet were propagating into a homogeneous medium, with a density found outside of its bow shock ($\approx 6\,\mathrm{cm}^{-3}$ in this case) gives according to equation (A.9): $L_{\mathrm{kin}} = 3.7 \times 10^{46}$erg. This is an underestimate of the true kinetic jet luminosity by 8 %. Hence, the combined effects of the declining density and cooling only marginally affects the derived parameters, which are lower limits to the true parameters. Given the other measurement errors (compare section VI.4.1), this should be negligible in many cases.

VII.2.4 State of the gas

The pn- and Tn-histograms are shown in Fig. VII.5. For $t = 1.39$ Ma, the pn-histogram can hardly discerned from the corresponding one in Fig. IV.2. This confirms the small effect of cooling at that time claimed above. At $t = 3$ Ma, the isothermal branch from the bow shock is quite prominent, indicating that much of the bow shock has cooled down at that phase. The sound speed in the cool clumps is about 0.03 kpc/Ma, which makes the final phase of the collapse slow. At the final time, some material has been compressed upto pressure equilibrium, which shows that the low pressure in the bow shock at $t = 3$ Ma is at least partly due to material that had not enough time to get compressed. In some regions the resolution may limit the compression. The overall pressure decreases with time. The effect is that at $t = 6.76$ Ma the densest regions are in pressure equilibrium with the jet cocoon. The cooled material changes its state adiabatically to lower and higher temperature, around the isothermal line (see above). The mixing in the cocoon can be followed nicely on those graphs: While at $t = 1.39$ Ma, the material is uniformly distributed along the isobar line, it clusters around log (p)=-8, log (n)=-1.5, at the final time. At all times, the vertical lines connecting the initial condition for the jet (left line) and the

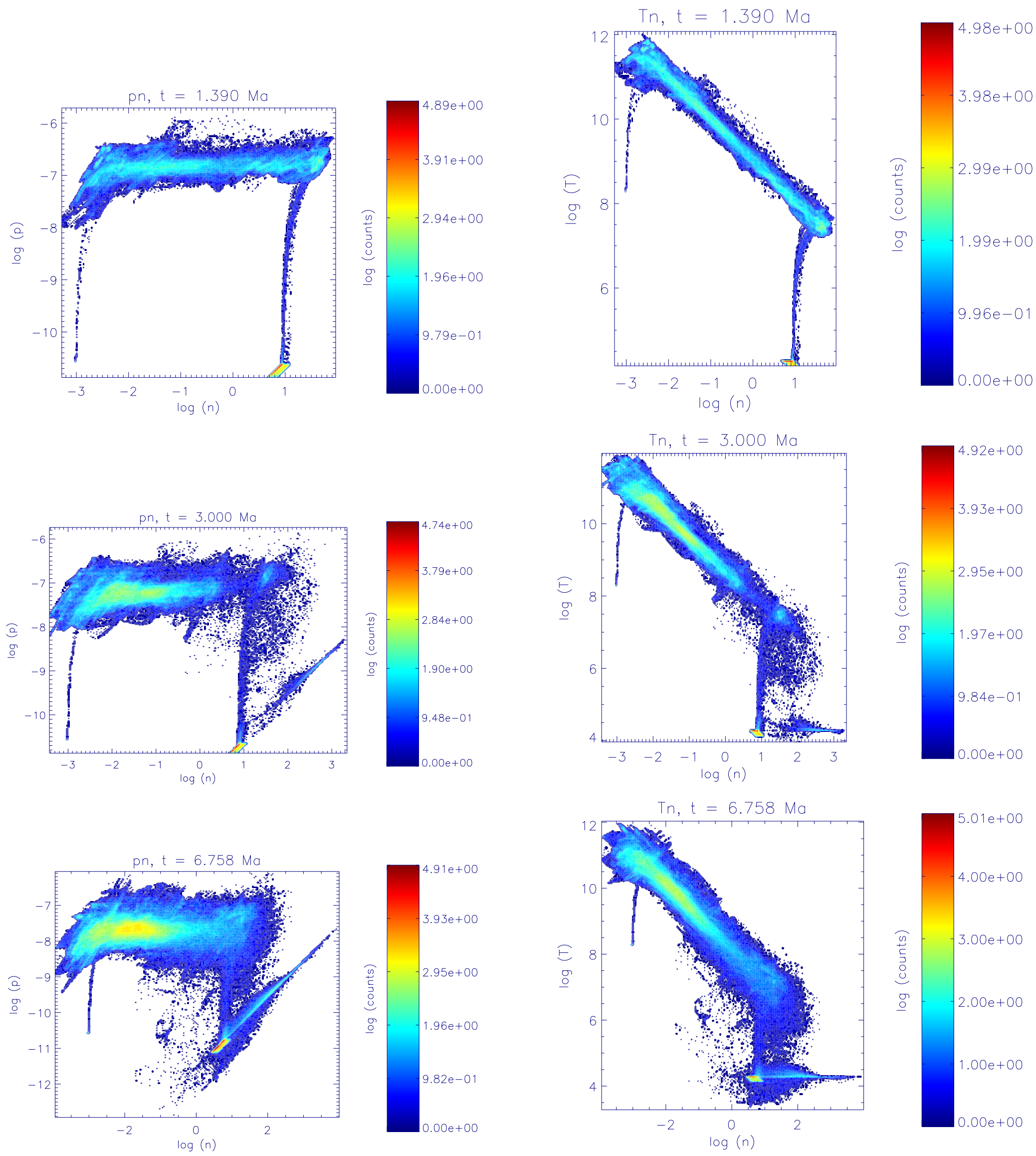

Figure VII.5: *Gas state histograms for t=1.39 Ma, t=3.00 Ma, and t=6.76 Ma for run B.*

external material (right line) to the isobar line are densely occupied (compare Fig. V.7). This proves that the bow shock was adequately resolved for the times shown.

VII.3 Run A: Long Term Evolution

This run was performed at low resolution, which may give misleading results for jet and cocoon. Especially, the radiative behaviour of the bow shock is not

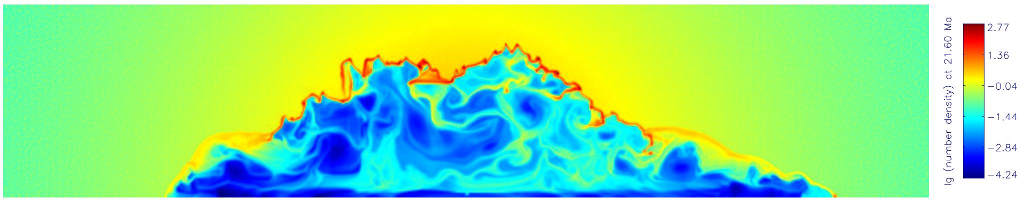

Figure VII.6: *Number density for the final timestep of run A. The full grid is shown.*

resolved. Besides one important detail: the information that it is indeed in the radiative phase. Figure VII.6 shows the density distribution for the final timestep of the simulation, which corresponds to 21.6 Ma. Like in the 3D simulation, the bow shock has started a cigar phase at each end of the jet. This phase is now not only distinct by the sharp bend in the bow shock shape, but also in the cooling properties. Here, the cigars behave like newly created bow shocks in less dense material further out. Consequently, they did not enter a radiative phase yet. Therefore the density distribution shows lower values and no fragmentation in the cigar phase, whereas the bow shock part from the blastwave phase shows these signs clearly.

VII.4 Conclusions

The propagation of the bow shock in the blastwave phase can be partly understood with the aid of the analytic approximation, even in a decreasing density distribution and with substantial cooling. Determination of the basic quantities after the prescription of chapter VI still gives an accuracy of better than ten percent. The bow shock – well-resolved, although there may be some regions where the compression is limited by resolution – is observed to fragment into filaments and clumps of $\approx 10^6 M_\odot$, which is similar to the Jeans mass there. The fragmentation is on a smaller scale as in the low resolution simulation from chapter V. Therefore, line emitting regions have no more to be expected to be clearly separated from X-ray gas. Also, adiabatic expansion of several regions in the bow shock is observed, which can cool some locations down to 1000 K. Some fingers of entrained external material are observed to form cool clumps. This confirms the predictions from chapter V, although there should be many smaller clumps within the cocoon. They are probably still below the resolution limit. The timescale for this process to happen is the cooling timescale of the post bow shock gas. This timescale is approximately 1 Ma for the parameters chosen here, and increases linearly with the density in the external medium. The clumping in fragments of the order of the Jeans mass is evidence for jet induced star formation in this simulation. The jet cocoons dissolve towards the center into filaments, which is sometimes also seen in observations (e.g. in Cygnus A, Carilli and Barthel, 1996). This suggests that jet cocoon dynamics may not be dominated by magnetic fields. However, this can change in a higher resolution simulation. When the cigar phase occurs, which now has been the case for different simulation parameters, it is observed in this simulation to form an adiabatic bow shock, whereas the inner bow shock can be radiative.

VII.5 Comparison to Observations: PKS 1138-262 at z = 2.16

PKS 1138-262 was extensively studied (e.g. Pentericci et al., 1997, 1998, 2000; Kurk et al., 2000, 2001a; Carilli et al., 2002). The observations show that it is the central member in a forming galaxy cluster. It has a spectacular bend in the radio morphology, which is also a peak in the Lyman α emission, proving the close interaction between these components. This object was recently imaged with Chandra. Although the large redshift of the source reduces the image quality considerably compared to Cygnus A, Carilli et al. (2002) claim that the extended emission elongated in the direction of the jet most likely originates from gas heated by the jet's bow shock. However, the properties of this gas could determine only with great uncertainties (a factor of 20 for the temperature). Carilli et al. (2002) estimate a number density of $n = 0.05\,\mathrm{cm}^{-3}$, and a temperature of 6×10^7 K in the bow shock. The bow shock's width perpendicular to the jet seems to be small far from the core, but may be broader in the center. The shape is hard to be determined because of the low number of counts, and the large contamination from the core. This is consistent with a cigar phase on the side of the undisturbed hotspot. On that side, the Lyman α emission ceases long before the hot spot (Pentericci et al., 1997). The line emission could come from cooled material behind the inner bow shock, or entrained material. In the optical, one can see several clumps within the emission line gas (Pentericci et al., 1998). They could correspond to star forming regions, since the optical emission corresponds to the UV range at $z = 2.16$. Similar clumpy morphology was found in the simulation (compare above). The emission line region has a diameter of roughly 50 kpc. If the emission line gas is indeed produced in the suggested way, this will be the scale of the inner bow shock diameter. Also the cooling timescale (equation V.2) has to be sufficient to produce the cool material. Combining equation (V.2) with the radial bow shock propagation law (equation A.10), yields a source age of 15 Ma, an external density of $0.8\,\mathrm{cm}^{-3}$, and a luminosity of 8×10^{46} erg/s, if one applies a typical radial bow shock velocity of 1 kpc/Ma, similar to Cygnus A. The radio luminosity between 0.1 and 1 GHz of 1.8×10^{45} erg/s (Carilli et al., 2002) would be 2 % of that luminosity. This is in the range of allowed values for Cygnus A. The numbers emerging from this analysis are quite reasonable. This indicates that the underlying model could be correct. A prediction of the model is the radial bow shock velocity, and the age of the source. They can be tested with spectral aging methods, which should give lower values, and measurement of the temperature jump at the bow shock. Also predicted is the external density at a radius of ≈ 25 kpc of $0.8\,\mathrm{cm}^{-3}$. If the density would decrease like r^{-2}, this would be consistent with the value of $0.05\,\mathrm{cm}^{-3}$ at 100 kpc (Carilli et al., 2002).

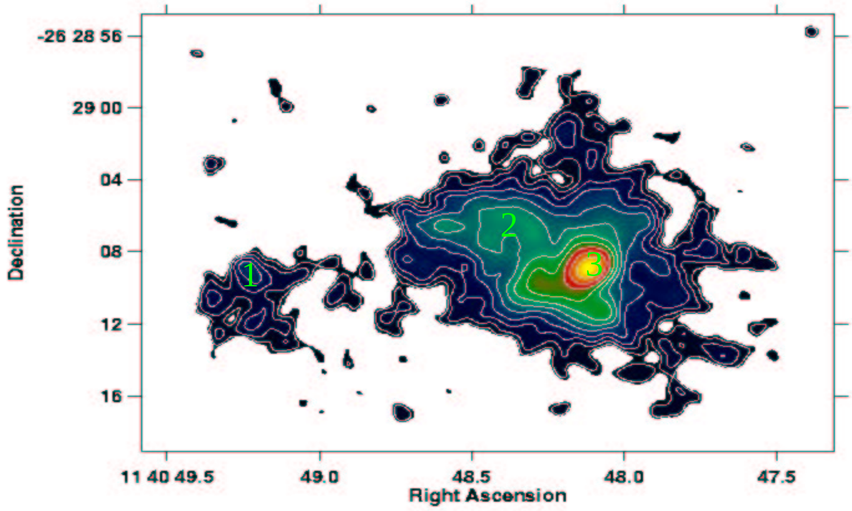

Figure VII.7: *Lyman α halo of the radio galaxy 1138-262 at $z = 2.16$. The core is in the region labeled with 2. The left jet is straight and terminates at a hot spot in region 1. The right jet has a prominent bend in region 3 where the Lyman α is brightest. Courtesy: Laura Pentericci*

The data are not conclusive, yet it would be most interesting to have better observational data at hand so that this model could be confirmed or falsified.

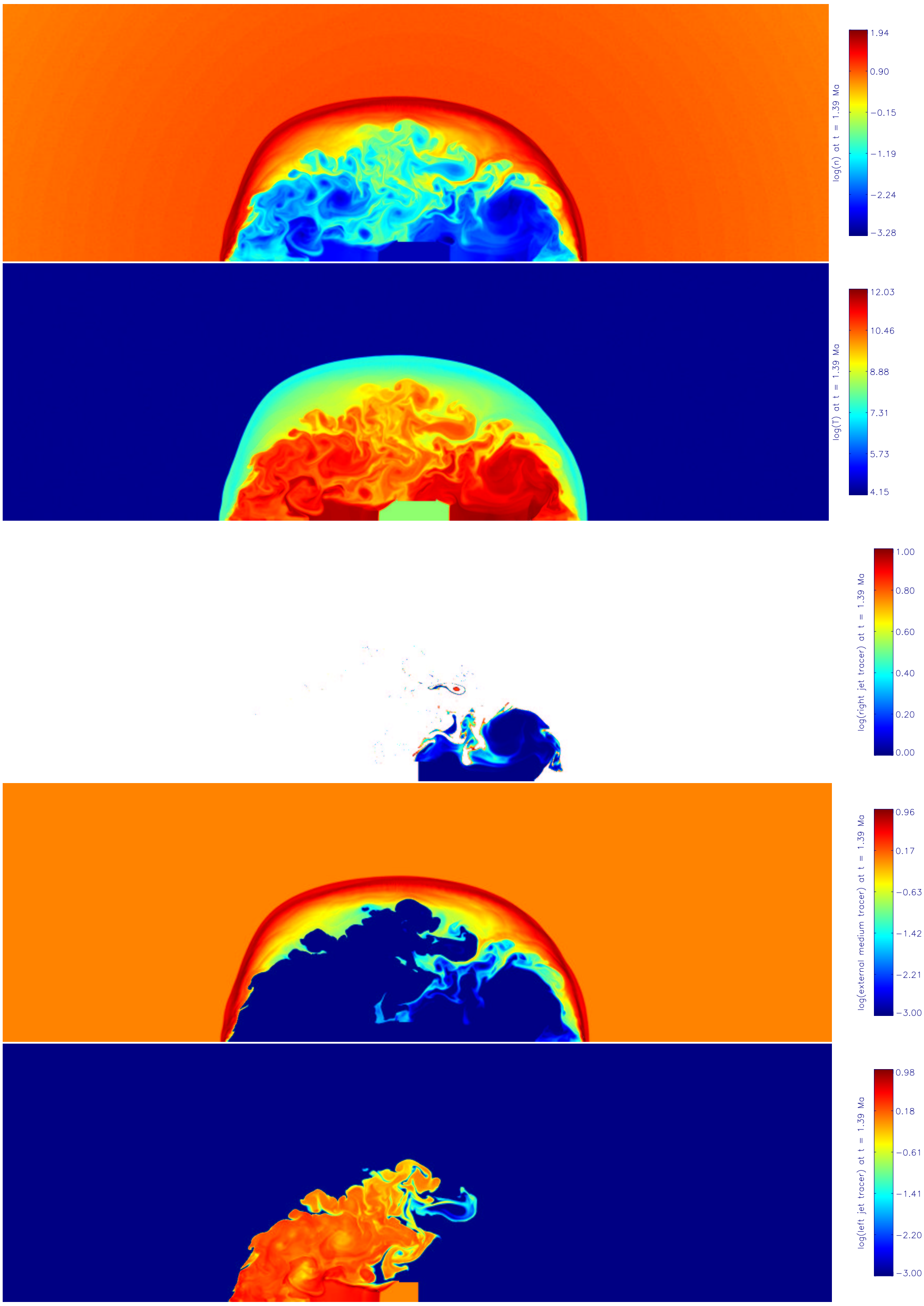

Figure VII.8: *From top to bottom: number density, temperature, tracer around zero showing the material from the right jet, positive tracer displaying the external medium, and negative applicable for the left jet at t=1.39 Ma for run B. The scale of the pictures is* $-10\,\mathrm{kpc} < Z < 10\,\mathrm{kpc}$, $0 < R < 6.2\,\mathrm{kpc}$.

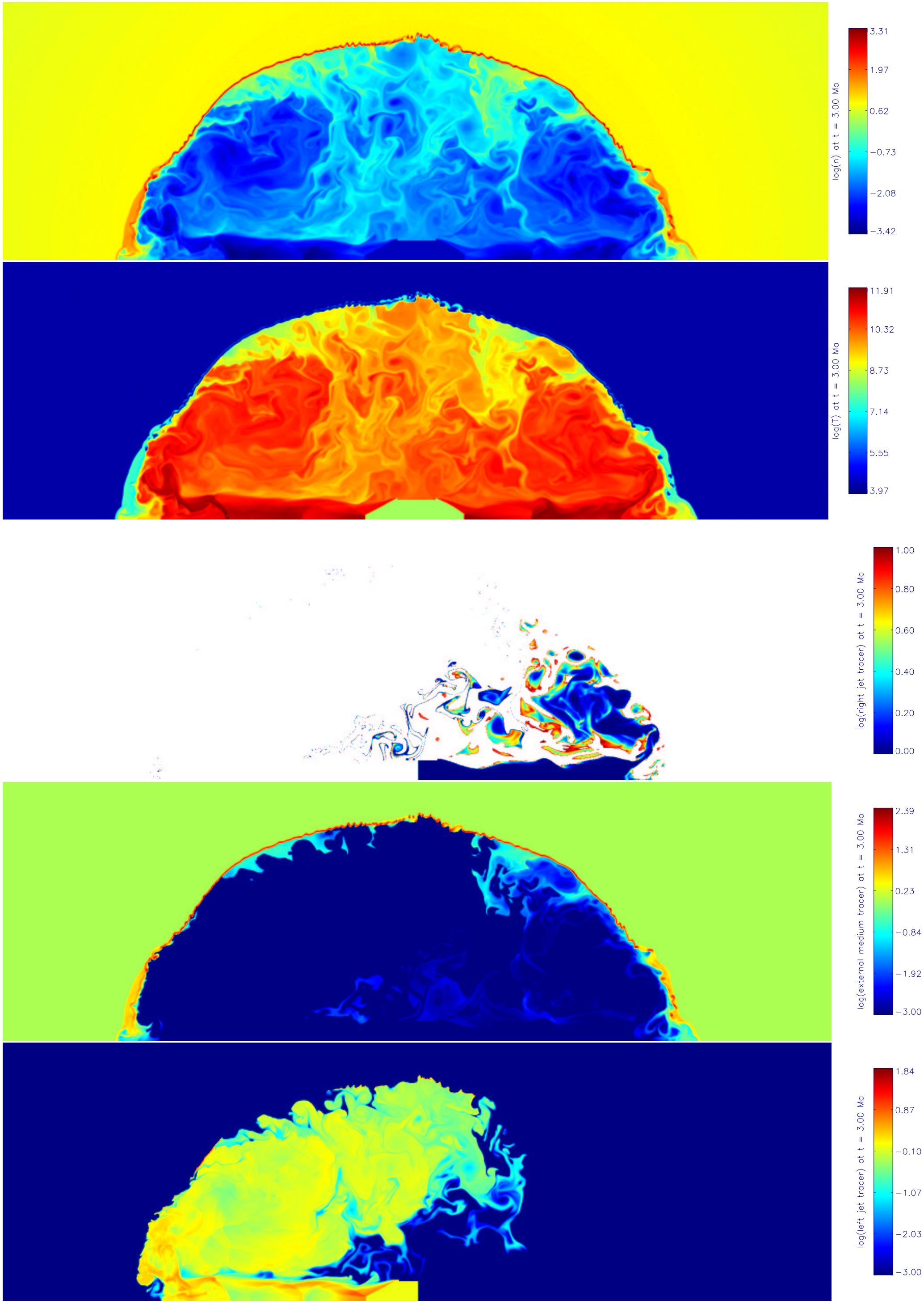

Figure VII.9: *The same as Fig. VII.8 for t=3.00 Ma. The scale of the pictures is* $-10\,\mathrm{kpc} < Z < 10\,\mathrm{kpc}$, $0 < R < 6.2\,\mathrm{kpc}$.

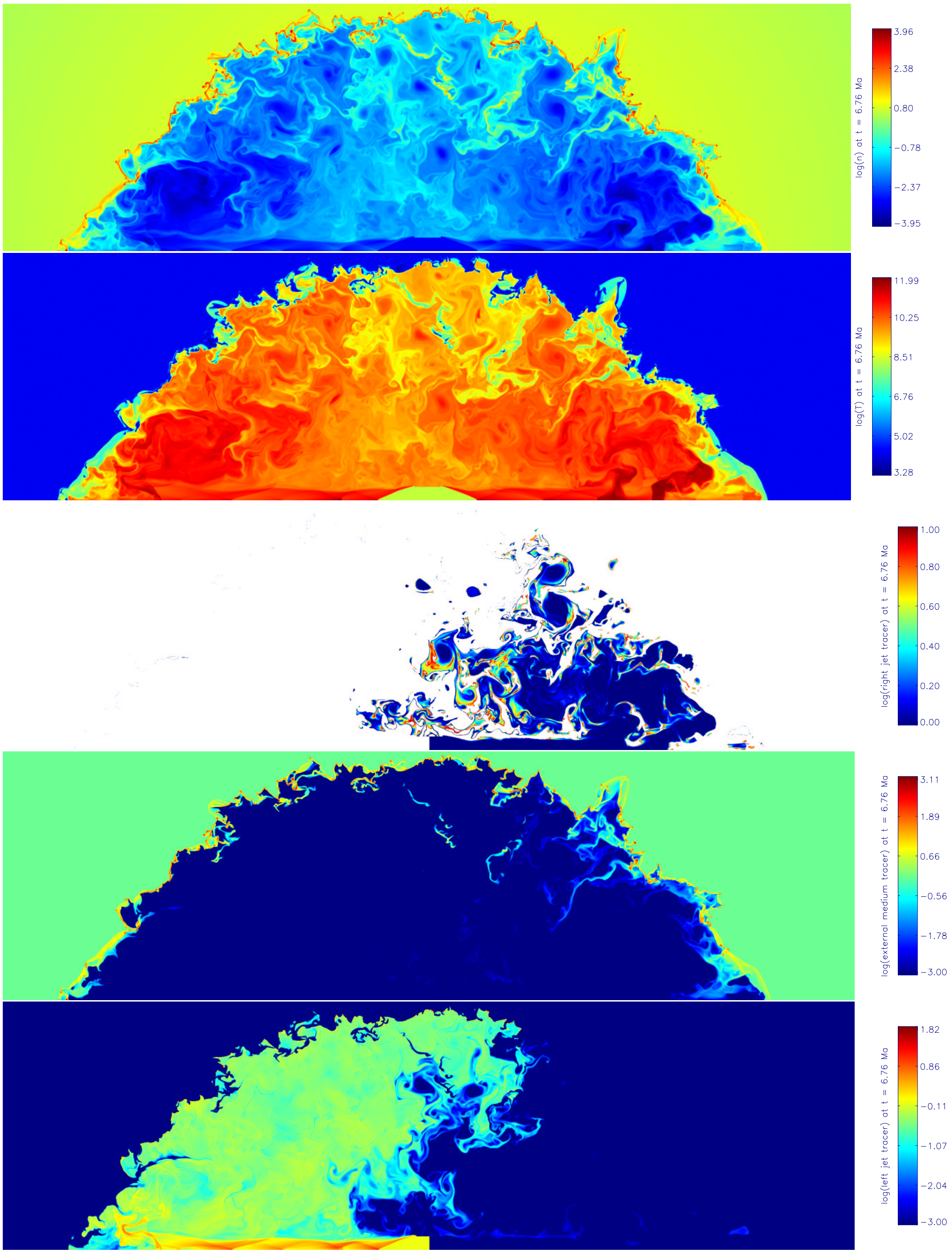

Figure VII.10: *The same as Fig. VII.8 for t=6.76 Ma. The scale of the pictures is* $-15\,\mathrm{kpc} < Z < 15\,\mathrm{kpc}$, $0 < R < 8.7\,\mathrm{kpc}$.

Chapter VIII

Summary & Outlook

The starting point for this thesis was the suspected high density environment in high redshift radio galaxies. The 3D magnetohydrodynamics code NIRVANA_C was applied for modelling the interaction of extragalactic jets with such a dense environment. The code was validated by comparison to two other codes, and found to represent important structures well and with medium efficiency. Estimating the essential parameters of a jet in such an environment, it was found that the density contrast between jet and external medium could be considerably lower than previously thought, down to $\eta = 10^{-5}$. Since jet simulations are rare in this regime, and are absent below $\eta = 10^{-3}$, a parameter study was carried out. As expected, the cocoons broaden with decreasing η. Between $\eta = 10^{-2}$ and $\eta = 10^{-3}$ the cocoons make a transition and get detached from the beam with a tendency to form one single large vortex. This transition is nearly independent of the Mach number, mainly because low η hydrodynamic jets transform most of their kinetic energy into thermal energy at strong internal shocks. In general, the details of the cocoon structure could not be sufficiently resolved, which was shown in a resolution study for one special parameter set. However, the overall size, which is similar to the total source size, should be a definite prediction of those models. If somehow a low density contrast can be estimated in a particular jet source, a broad cocoon should be found. Otherwise, the assumptions of the models are not correct, and presumably the magnetic field is strong enough in such sources to keep the cocoon around the jet. The density contrast was found to be tightly coupled to the aspect ratio of the bow shock, after the initial phase. In that context, an early phase in the bow shock propagation was discovered. In this phase, the bow shock is spherically symmetric. It was shown by detailed comparison to a 3D numerical model that the analytic blastwave solution, modified due to constant energy injection, is able to describe the bow shock propagation with very high accuracy (chapter VI). The description is still accurate for the radial expansion of the bow shock, when the jet head already shapes the shock. The accuracy was shown to be still on the 5 % level for a decreasing external density, and considerable cooling losses of the shocked external medium (chapter VII). Quite often in the simulations, the bow shock showed a sudden transition producing a cigar like extension in beam flow direction, accompanied by a considerable acceleration of the head propagation velocity. It was shown that the onset of this cigar phase is modulated by the cocoon pressure, which regulates the strength of oblique shocks in the beam. It could also be shown, that the cocoon pressure decreases more strongly the steeper the external density decrease. Hence, a cigar start at the core radius of a galaxy or cluster would be favoured. However, other radii are not precluded, and an exact theory predicting the outbreak radius could not be found.

With this results at hand, several low redshift sources could be found where the bow shock clearly stated that the density contrast was also low in that systems. Therefore, a hydrodynamic 3D model was computed, with the literature parameters of Cygnus A. The model clearly deviated from the observation, indicating that the so far believed parameters are partly wrong. The jet velocity is higher and the density lower than previously thought. The model constraints the basic source parameters tightly, including the black hole mass in the center. Where available, other estimates were confirmed. The resulting X-ray emission of the numerical model was integrated in jet direction and perpendicular to it. In the first case, an X-ray cavity was found, which was already predicted by Clarke et al. (1997). Axially integrated, the X-ray cavity is even more evident. The first bow shock, from the blastwave phase, makes a big ring in projection. The cigar like extensions produce a second ring inside the first one. These two rings could be clearly identified in the radio source 3C317, and they were used to determine the inclination of the jet to 37°. Two inner rings were found in published X-ray data of M87. These were interpreted as small cigar extensions on opposite sides of the bow shock. The shortening axis of those rings was found to coincide with one another, but not with the jet axis. Precession on a cone with opening angle of 40° and a period of ≈ 2 Ma was proposed as an explanation. It is argued, that the precession should be caused by the Lense-Thirring effect on the spin axis of a secondary black hole, orbiting the primary one in a distance of at least 0.03 pc, which is currently the real jet origin. This model can nicely explain the three different radio lobe systems in M87.

Since the two phases turned out to be vital for an understanding of some low and intermediate redshift sources, it was attempted to simulate a jet with cooling up to the distance where the cigar phase starts. This was possible only for a low resolution model. The high resolution model showed, that cocoon shapes of hydrodynamic low η jets transform in the right direction at higher resolution, to be compatible with observations: The extended regions appear smaller because of the violent mixing with other material. The bow shock behaviour was observed to confirm and refine the results from a lower resolution run with a more detailed description of the cooling. It gets compressed up to high densities, and fragments into filaments and clumps radiating X-rays and emission lines. The high resolution simulation also showed that the non-linear Kelvin-Helmholtz instability can create emission line regions within the cocoon by entrainment of shocked external medium. This process produces the largest emission line regions in the central region, which is also found in observations. In the low resolution large scale simulation, the bow shock was radiative in the central part and nearly adiabatic for the cigar phase part. If this is the case in a real source depends on the steepness of the density decline. However, where the situation is like that, emission line regions in the center are again favoured. The bow shock cools rapidly down to $\approx 10^4$ K, where it is predominantly neutral. Since the radial bow shock velocity is now considerably slowed down, there is not much emission in that phase, and the bow shock can absorb emission from within the cocoon. For this process to explain the observed absorbers in high redshifted radio galaxies, an environmental density of $\approx 5\,\mathrm{cm}^{-3}$ is needed in the inner parts of those objects. Such high density regions would be absorbers themselves, leading to a separate class of absorbers, with low velocities relative to the emission peak. This describes the observations well. The cooled region forms clumps of $10^6 M_\odot$ close to the Jeans mass. It is therefore likely, that the bow shock produces stars rapidly in approximately 10^4 globular clusters. The present day brightest cluster ellipticals, which are believed to be the aged successors of the most powerful high redshift radio galaxies, show such an unusual excess of globular clusters.

In this thesis, many testable predictions were made. Therefore, the next step in this field should be observational tests, preferably X-ray observations of shocked cluster gas. The most outstanding theoretical question is the determination of the cigar phase start. What is the limiting η for this process to occur? How have the exact conditions to be? Parameter studies can help answering these questions. The properties of the magnetic field that are needed if it was to collimate the cocoon has to be worked out. For an understanding of the jet bending in high redshift sources, 3D simulations at low η are required. A detailed understanding of the emission line structure, can be achieved only by computation of the radiation transfer. This is a complex task even if it is not done together with hydrodynamics.

Appendix A

The Thin Spherical Shell

The solution for the spherically symmetric thin shell to the hydrodynamic equations was found by Sedov (1959). According to his solution, an amount of energy $E(t)$ released at the origin at $t = 0$ drives a blastwave into the external medium, where the density $\rho_0(r/a_c)^\kappa$ is allowed to decline according to a power law. The approximation is that all of the mass $M\,(= V(r(t))\rho_0)$ is concentrated in a thin shell with radius $r(t)$ and velocity $v(t)$. Neglecting the external pressure, the conservation equations for mass and momentum are:

$$\frac{\partial}{\partial t}(M) = S\rho_0 v \tag{A.1}$$

$$\frac{\partial}{\partial t}(Mv) = SP, \tag{A.2}$$

where $S = 4\pi r^2$ is the surface of the shell. The pressure is given by the energy input, $P = 2(E(t) - Mv^2/2)/3V$. Here $E(t)$ and ρ_0, which enters into the shell mass $M = \int_0^r 4\pi r\prime^2 \rho_0 (r\prime/a_c)^\kappa dr\prime$, are input parameters to be specified. $V = \frac{4\pi}{3} r^3$ is the volume occupied by the shell. This ansatz can easily be put together into the following differential equation for the radius r:

$$r^{\kappa+5}\left((\kappa+4)\left(\frac{\dot r}{r}\right)^2 + \frac{\ddot r}{r}\right) = \frac{a_c^\kappa(\kappa+3)E(t)}{2\pi\rho_0}, \tag{A.3}$$

where $\dot r = v$ denotes the derivation of r with respect to time t. Equation (A.3) can be solved with a power law ansatz, $r = a\,t^b$, if the energy is also given as a power law, $E(t) = c\,t^d$. The result is:

$$r = \left(\frac{a_c^\kappa(\kappa+3)(\kappa+5)c\,t^{d+2}}{2\pi\rho_0(d+2)(d+1)}\right)^{\frac{1}{\kappa+5}} \tag{A.4}$$

The energy E in such a system is divided among thermal and kinetic. The kinetic energy is given by:

$$E_{\text{kin}} = \frac{d+2}{(d+1)(\kappa+5)} ct^d \tag{A.5}$$

This shows that the most effective thermodynamic engine of this type works with $d = 0$, i.e. instantaneous energy release (40 % for homogenous density, $\kappa = 0$). In the jet case ($d = 1$), the kinetic energy of the shell amounts still to 30 %. The kinetic energy fraction can be quite large in a declining density distribution. For $\kappa = -3$, which may be found in an asymptotic King profile, the jet blown bubble engine works at 75 % efficiency, keeping the expanding shell at constant pace. Of course, this can not be found in nature, strictly speaking, since power laws with negative exponent diverge at $r = 0$. However, the simulation shows a quite similar behaviour to the simple analysis presented here in regions with similar exponents, and thus it provides a useful basis for understanding.

The following discussion is carried out for a homogeneous external medium ($\kappa = 0$). For a supernova remnant one would now have to insert $d = 0$ and $c = E_0$ for an instantaneous energy release. This gives:

$$r = \left(\frac{15E_0}{4\pi\rho_0}\right)^{1/5} t^{2/5} \tag{A.6}$$

$$v = \sqrt{\frac{3E_0}{5\pi\rho_0}}\, r^{-3/2}. \tag{A.7}$$

For the jet blown bubble, it follows with $d = 1$ and $c = L$:

$$r = \left(\frac{5L}{4\pi\rho_0}\right)^{1/5} t^{3/5} \tag{A.8}$$

$$v = 3\left(\frac{L}{100\pi\rho_0}\right)^{1/3} r^{-2/3}. \tag{A.9}$$

Eliminating L/ρ_0 leads to:

$$r = \frac{5}{3} v t \tag{A.10}$$

Using the formula for the non-relativistic jet luminosity, $L = \pi R_\mathrm{j}^2 \rho_\mathrm{j} v_\mathrm{j}^3$, one can derive the following equation:

$$\left(\frac{\rho_\mathrm{j}}{\rho_\mathrm{bw}}\right)\left(\frac{R_\mathrm{j}}{r_\mathrm{bw}}\right)^2\left(\frac{v_\mathrm{j}}{v_\mathrm{bw}}\right)^3 = \frac{100}{27} \approx 3.7 \tag{A.11}$$

Here the index bw denotes the blastwave quantities. One can now calculate the bubble radius r_c, at which the jet begins to shape the bow shock. This can happen only if the the velocity of the jet head, given by equation (I.1) becomes equal to the blastwave velocity v_bw. The result is:

$$\frac{r_\mathrm{c}}{R_\mathrm{j}} = \sqrt{\frac{27}{100}\frac{1}{\sqrt{\eta}}\left(\frac{1+\sqrt{\epsilon\eta}}{\sqrt{\epsilon}}\right)^3} \approx 0.52\,\eta^{-1/4}\epsilon^{-3/4}, \tag{A.12}$$

where the last approximation is valid for low η. In the blastwave phase, the jet propagates with higher efficiency. Hence, one could ask if, for a given luminosity, external density, and propagation distance R, one could determine a maximum

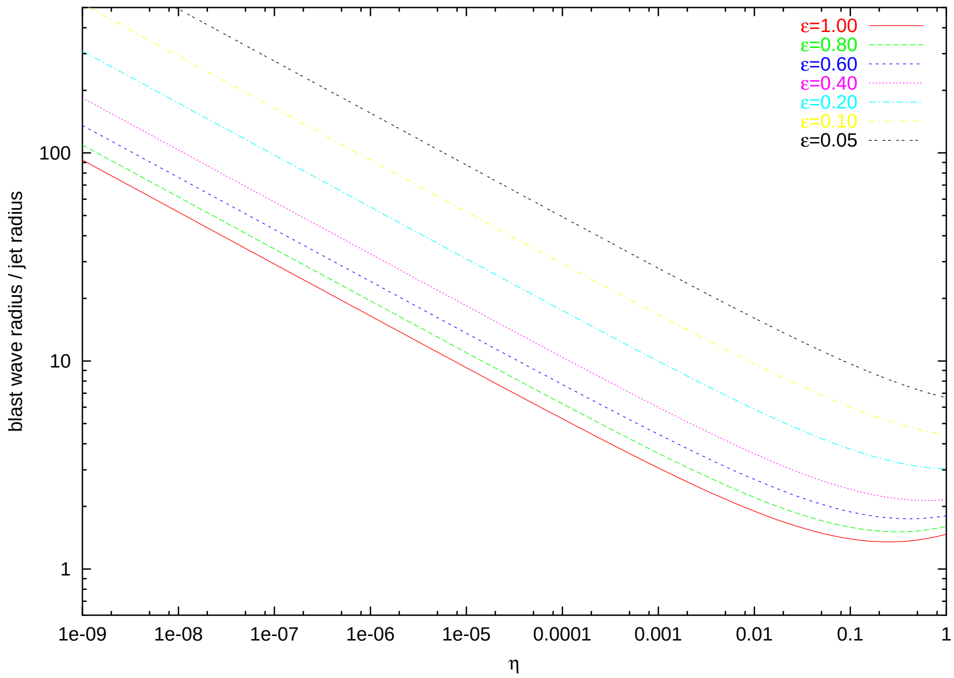

Figure A.1: *Radius $r_{\mathrm{burst}}/R_{\mathrm{j}}$ at which the jet can first shape the bow shock, over η for different values of ϵ.*

age of the jet:
Let us assume that a jet on its way out to distance R is in the blastwave phase up to the critical distance given by equation (A.12). The time needed for this distance (t_1) can then be calculated according to equation (A.8). The time for the other part of the way can be calculated with the constant velocity given by equation (I.2). The sum of these times is:

$$\Theta = \frac{R_{\mathrm{j}}}{v_{\mathrm{j}}}\left(1+\sqrt{\epsilon\eta}\right)\eta^{-1/2}\epsilon^{-1/2}\left(\frac{R}{R_{\mathrm{j}}} - \frac{3}{25}\sqrt{3}\eta^{-1/4}\epsilon^{-3/4}\left(1+\sqrt{\epsilon\eta}\right)^{3/2}\right) \quad \text{(A.13)}$$

In the limit of low density contrast, equation (A.13) can be approximated by

$$\Theta = \frac{R_{\mathrm{j}}}{v_{\mathrm{j}}}\eta^{-1/2}\epsilon^{-1/2}\left(\frac{R}{R_{\mathrm{j}}} - 0.21\eta^{-1/4}\epsilon^{-3/4}\right). \quad \text{(A.14)}$$

Θ is shown in Fig. A.2. Clearly Θ has one maximum at $\eta_{\mathrm{max}} = \left(\frac{243}{2500}\right)^2 \epsilon^{-3}(R/R_{\mathrm{j}})^{-4}$. The maximum Θ is:

$$\Theta_{\mathrm{max}} = \frac{2500}{729}\epsilon\frac{R_{\mathrm{j}}}{v_{\mathrm{j}}}\left(\frac{R}{R_{\mathrm{j}}}\right)^3. \quad \text{(A.15)}$$

Now, one can substitute the jet luminosity. ϵ and the jet radius cancel out, and it follows:

$$\Theta_{\mathrm{max}} = \left(\frac{2500\pi\rho_0 R^5}{6561L}\right)^{1/3} \approx 1.06\left(\frac{\rho_0 R^5}{L}\right)^{1/3} \quad \text{(A.16)}$$

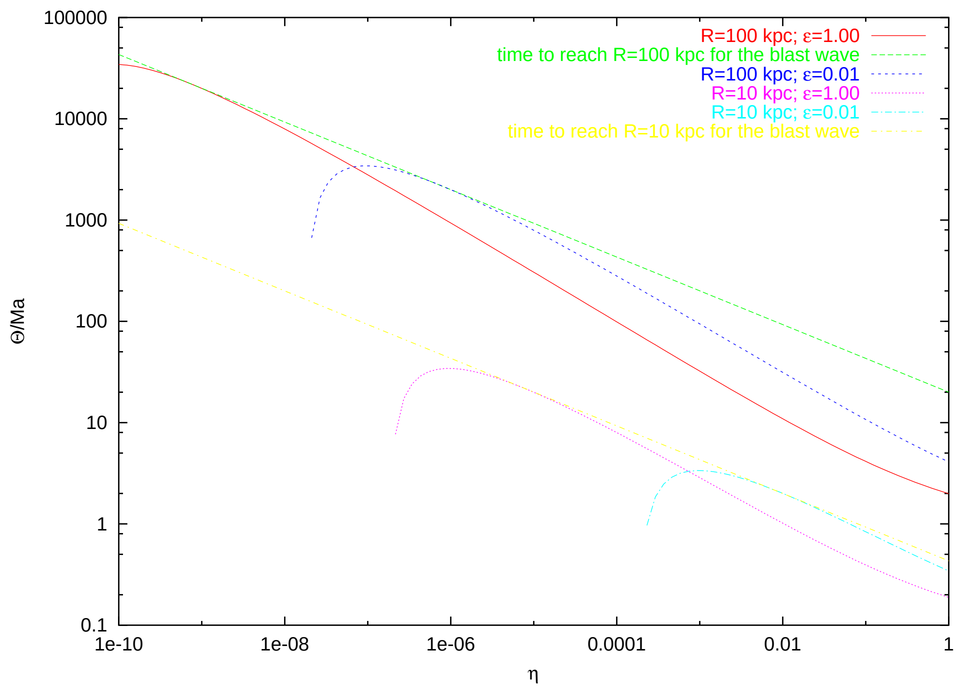

Figure A.2: *Propagation time Θ over η for different values of R and ϵ. For demonstration purposes, the jet velocity was set to 100 kpc/Ma, and the jet radius to 1 kpc. Also shown is the time for the jet to reach distance R if it was in the blastwave phase, always. This is an upper limit to the true propagation time, and replaces the other curves left of the tangent point. The unrealistically high times in this plot are caused by the arbitrary variation of L in proportion to η.*

But unfortunately, it turns out that $\eta_{\max}$ is already beyond the range of allowed η. Figuring out the critical radius for $\eta_{\max}$ results in: $r_c(\eta = \eta_{\max}) = 1.7R$. This reveals that the maximum was artificially produced by a negative t_2. Hence for a determination of the maximum propagation time, one can safely assume the jet not to have left the bubble phase, yet. Therefore the bubble equation gives an upper limit for the age of the jet:

$$\Theta_{\max} = \left(\frac{4\pi\rho_0 R^5}{5L}\right)^{1/3} \approx 1.36\left(\frac{\rho_0 R^5}{L}\right)^{1/3}. \tag{A.17}$$

L in equation (A.17) has, of course, to be the luminosity which really serves to blow up the bubble, subtracting radiation losses. Since the radio luminosity of a jet is typically less than half the total luminosity, it would produce fiducial upper limits for $\Theta_{\max}$.

Appendix B

Publications

The material presented in this thesis has been published in part in the following essays.

B.1 Contributions

On the resolution in astrophysical jet simulations, Martin Krause & Max Camenzind, in: Emission Lines from Jet Flows, poster proceedings of a conference held on November 13-17, 2000 in Isla Mujeres, Mexico, eds: P. Velazquez & R. Gonzalez, Instituto de Astronomia, UNAM, Ap. Postal 70-247, CP: 04510, Mexico D.F., p. 22

Could multiple activity cycles provide a clue to the emission line profiles of HZRGs?, Martin Krause & Max Camenzind, in: Emission Lines from Jet Flows, poster proceedings of a conference held on November 13-17, 2000 in Isla Mujeres, Mexico, eds: P. Velazquez & R. Gonzalez, Instituto de Astronomia, UNAM, Ap. Postal 70-247, CP: 04510, Mexico D.F., p. 25

B.2 Refereed Articles

Reliability of astrophysical jet simulations in 2D – On inter-code reliability and numerical convergence Martin Krause & Max Camenzind, 2001, A&A 380, 789-804

A 3D Hydrodynamic Simulation for the Cygnus A Jet as a Prototype for High Redshift Radio Galaxies, Martin Krause & Max Camenzind, in: High Performance Computing in Science and Engineering '01 – Transactions of the High Performance Computing Center Stuttgart (HLRS) 2001, eds: E. Krause & W. Jäger, Springer, 2002

Absorbers and Globular Cluster Formation in Powerful High Redshift Radio Galaxies, Martin Krause, A&A, in press.

Appendix C

Shortcuts

Journals	
A&A	Astronomy & Astrophysics, EDP Sciences
AJ	The Astronomical Journal, American Astronomical Society
ApJ	The Astrophysical Journal, American Astronomical Society
MNRAS	Monthly Notices of the Royal Astronomical Society
The messenger	European Southern Observatory

Abbreviations	
AGN	active galactic nucleus
ELL	emission line lobes
FLOPS	floating point operations per second
GFLOPS	10^9 floating point operations per second
HZRG	high redshift radio galaxy ($z > 2$)
IGM	inter-galactic matter
KH	Kelvin-Helmholtz
MHD	magnetohydrodynamic(s)
pn	pressure versus number density
ppb	points per beam radius
RT	Rayleigh-Taylor
2D	two-dimensional
3D	three-dimensional

Mathematical Symbols	
A	area
c	speed of light
M	Mach number
$M_\odot$	solar mass, 1.989×10^{33} g
n	number density
p	pressure
R_{j}	jet radius
v	velocity
T	temperature
Z	metalicity
z	redshift
β	v/c
Γ	$1/\sqrt{1-\beta^2}$
γ	adiabatic exponent
ϵ	jet beam to head area ratio
η	jet/ambient density ratio
κ	jet/ambient pressure ratio
ρ	density

Bibliography

P. Alexander. A study of spectral ageing in the radio galaxy 3C234 and its implications. *MNRAS*, 225:27–42, March 1987.

M. A. Aloy, J. M. Ibáñez, J. M. Martí, J.-L. Gómez, and E. Müller. High-Resolution Three-dimensional Simulations of Relativistic Jets. *ApJ Letter*, 523:L125–L128, October 1999.

S. Appl. Instabilities in transmagnetosonic jets. *A&A*, 314:995–1002, October 1996.

S. Appl and M. Camenzind. The stability of current-carrying jets. *A&A*, 256: 354–370, March 1992.

C. N. Arnold and W. D. Arnett. Three-dimensional structure and dynamics of a supersonic jet. *ApJ Letter*, 305:L57–L60, June 1986.

W. Baade and R. Minkowski. Identification of the Radio Sources in Cassiopeia, Cygnus A, and Puppis A. *ApJ*, 119:206+, January 1954.

J. C. Baker. Lyman-α absorption: links between CSS quasars and high-redshift radio galaxies. In *The Most Distant Radio Galaxies*, pages 447+, 1999.

J. C. Baker. Associated absorption and radio source growth. In *Mass Outflow in AGN: New Perspectives, ASP Conf Series, eds. D.M. Crenshaw, S.B. Kraemer, I.M. George*, July 2001.

J. C. Baker, R. W. Hunstead, R. M. Athreya, P. D. Barthel, E. de Silva, M. D. Lehnert, and R. D. E. Saunders. Associated absorption in radio quasars. I. C IV absorption and the growth of radio sources. In *Accepted by ApJ.*, pages 12141+, December 2001.

S. A. Baum and P. J. McCarthy. Emission-Line Properties of 3CR Radio Galaxies. III. Origins and Implications of the Velocity Fields. *AJ*, 119:2634–2644, June 2000.

M. C. Begelman and D. F. Cioffi. Overpressured cocoons in extragalactic radio sources. *ApJ Letter*, 345:L21–L24, October 1989.

P. N. Best. The cluster environments of the z˜1 3CR radio galaxies. *MNRAS*, 317:720–736, September 2000.

G. V. Bicknell and M. C. Begelman. Theory of the M 87 Jet. In *The radio galaxy Messier 87 : proceedings of a workshop held at Ringberg Castle, Tegernsee, Germany, 15-19 September 1997 / Hermann-Josef Röser, Klaus Meisenheimer, eds. Berlin ; New York : Springer, 1999. (Lecture notes in physics, 530, ISSN0075-8450)., p.235*, pages 235+, 1999.

G. V. Bicknell, R. S. Sutherland, W. J. M. van Breugel, M. A. Dopita, A. Dey, and G. K. Miley. Jet-induced Emission-Line Nebulosity and Star Formation in the High-Redshift Radio Galaxy 4C 41.17. *ApJ*, 540:678–686, September 2000.

L. Binette, J. D. Kurk, M. Villar-Martín, and H. J. A. Röttgering. A vestige low metallicity gas shell surrounding the radio galaxy 0943-242 at z=2.92. *A&A*, 356:23–32, April 2000.

E. L. Blanton, C. L. Sarazin, B. R. McNamara, and M. W. Wise. Chandra Observation of the Radio Source/X-Ray Gas Interaction in the Cooling Flow Cluster Abell 2052. *ApJ Letter*, 558:L15–L18, September 2001.

K. M. Blundell and S. Rawlings. The inevitable youthfulness of known high-redshift radio galaxies. *Nature*, 399:330–332, May 1999.

G. Bodo, S. Massaglia, A. Ferrari, and E. Trussoni. Kelvin-Helmholtz instability of hydrodynamic supersonic jets. *A&A*, 283:655–676, March 1994.

G. Bodo, S. Massaglia, P. Rossi, R. Rosner, A. Malagoli, and A. Ferrari. The long-term evolution and mixing properties of high Mach number hydrodynamic jets. *A&A*, 303:281+, November 1995.

G. Bodo, P. Rossi, S. Massaglia, A. Ferrari, A. Malagoli, and R. Rosner. Three-dimensional simulations of jets. *A&A*, 333:1117–1129, May 1998.

S. Britzen, A. Witzel, T. P. Krichbaum, R. M. Campbell, S. J. Wagner, and S. J. Qian. Three-year VLBI monitoring of PKS 0420-014. *A&A*, 360:65–75, August 2000.

M. Camenzind. Formation of Jets in Extragalactic Radio Sources. In *Jets in Extragalactic Radio Sources, Proceedings of a Workshop Held at Ringberg Castle, Tegernsee, FRG, September 22-28, 1991. Edited by H.-J. R&oouml;ser and K. Meisenheimer. Springer-Verlag Berlin Heidelberg New York. Also Lecture Notes in Physics, volume 421, 1993, p.109*, pages 109+, 1993.

M. Camenzind. *Les noyaux actifs de galaxies.* Galaxies de Seyfert, QSO, quasars, lacertides et radiogalaxies, XVIII, 218 pp.. Springer-Verlag Berlin Heidelberg New York. Also Lecture Notes in Physics, volume 46, 1997.

M. Camenzind. On Disks and Jet(s) in the Defunct Quasar M87. In *The radio galaxy Messier 87 : proceedings of a workshop held at Ringberg Castle, Tegernsee, Germany, 15-19 September 1997 / Hermann-Josef Röser, Klaus Meisenheimer, eds. Berlin ; New York : Springer, 1999. (Lecture notes in physics, 530, ISSN0075-8450).*, 1999.

C. L. Carilli and P. D. Barthel. Cygnus A. *A&AReview*, 7:1–54, 1996.

C. L. Carilli, D. E. Harris, L. Pentericci, H. J. A. Röttgering, G. K. Miley, J. D. Kurk, and W. van Breugel. The X-ray - radio alignment in the z = 2.2 radio galaxy PKS 1138-262. *ApJ*, 2002.

C. L. Carilli, G. Miley, H. J. A. Röttgering, J. Kurk, L. Pentericci, D. E. Harris, F. Bertoldi, K. M. Menten, and W. van Breugel. High-Redshift Radio Galaxies: Beacons to Biased Hierarchical Galaxy Formation Within Large-Scale Structure. In *Gas and Galaxy Evolution, ASP Conference Proceedings, Vol. 240. Edited by John E. Hibbard, Michael Rupen, and Jacqueline H. van Gorkom. San Francisco: Astronomical Society of the Pacific, ISBN: 1-58381-077-3, 2001, p. 101*, pages 101+, 2001.

C. L. Carilli, R. A. Perley, J. W. Dreher, and J. P. Leahy. Multifrequency radio observations of Cygnus A - Spectral aging in powerful radio galaxies. *ApJ*, 383:554–573, December 1991.

K. C. Chambers, G. K. Miley, and W. van Breugel. Alignment of radio and optical orientations in high-redshift radio galaxies. *Nature*, 329:604–606, October 1987.

K. C. Chambers, G. K. Miley, and W. J. M. van Breugel. 4C 41.17 - A radio galaxy at a redshift of 3.8. *ApJ*, 363:21–39, November 1990.

D. F. Cioffi and J. M. Blondin. The evolution of cocoons surrounding light, extragalactic jets. *ApJ*, 392:458–464, June 1992.

D. A. Clarke. 3-D MHD Simulations of Extragalactic Jets. In *Jets in Extragalactic Radio Sources, Proceedings of a Workshop Held at Ringberg Castle, Tegernsee, FRG, September 22-28, 1991. Edited by H.-J. R&oouml;ser and K. Meisenheimer. Springer-Verlag Berlin Heidelberg New York. Also Lecture Notes in Physics, volume 421, 1993, p.243*, pages 243+, 1993.

D. A. Clarke, D. E. Harris, and C. L. Carilli. Formation of cavities in the X-ray emitting cluster gas of Cygnus A. *MNRAS*, 284:981–993, February 1997.

D. A. Clarke, M. L. Norman, and J. O. Burns. Numerical simulations of a magnetically confined jet. *ApJ Letter*, 311:L63–L67, December 1986.

R. Courant and K. O. Friedrichs. *Supersonic flow and shock waves.* Pure and Applied Mathematics, New York: Interscience, 1948, 1948.

C. I. Cox, S. F. Gull, and P. A. G. Scheuer. Three-dimensional simulations of the jets of extragalactic radio sources. *MNRAS*, 252:558–585, October 1991.

C. De Breuck, H. Röttgering, G. Miley, W. van Breugel, and P. Best. A statistical study of emission lines from high redshift radio galaxies. *A&A*, 362: 519–543, October 2000.

C. De Breuck, W. van Breugel, A. Stanford, H. Rottgering, G. Miley, and D. Stern. Optical and Near-IR Imaging of Ultra Steep Spectrum Radio Sources - The K-z diagram of radio and optically selected galaxies. *AJ*, 123:??, January 2002.

D. S. De Young. Star formation in radio galaxies at large redshift. *ApJ Letter*, 342:L59–L62, July 1989.

D. S. De Young. The “Alignment Effect” and the Evolution of Dust in High-Redshift Radio Galaxies. *ApJ*, 507:161–172, November 1998.

D. S. De Young. The Fate of Dust and the Alignment Effect in HZRGs. In *The Most Distant Radio Galaxies*, pages 149+, 1999.

A. Dey, W. van Breugel, W. D. Vacca, and R. Antonucci. Triggered Star Formation in a Massive Galaxy at Z = 3.8: 4C 41.17. *ApJ*, 490:698+, December 1997.

M. A. Dopita and R. S. Sutherland. *Diffuse Matter in the Universe*. Springer, to appear, 2002.

J. E. Dyson, S. A. E. G. Falle, and J. J. Perry. Intrinsic formation of narrow-line absorption systems in QSOs. I - The piston phase. *MNRAS*, 191:785–819, June 1980.

S. A. E. G. Falle, J. J. Perry, and J. E. Dyson. Intrinsic formation of narrow-line absorption systems in QSOs. II - The radiatively driven phase. *MNRAS*, 195:397–427, May 1981.

B. L. Fanaroff and J. M. Riley. The morphology of extragalactic radio sources of high and low luminosity. *MNRAS*, 167:31P–36P, May 1974.

A. Ferrari. Modeling Extragalactic Jets. *ARAA*, 36:539–598, 1998.

R. Ganguly, N. A. Bond, J. C. Charlton, M. Eracleous, W. N. Brandt, and C. W. Churchill. On the Origin of Intrinsic Narrow Absorption Lines in z<˜1 QSOS. *ApJ*, 549:133–154, March 2001.

P. E. Hardee, D. A. Clarke, and A. Rosen. Dynamics and Structure of Three-dimensional Poloidally Magnetized Supermagnetosonic Jets. *ApJ*, 485:533+, August 1997.

W. E. Harris, G. L. H. Harris, and D. E. McLaughlin. M87, Globular Clusters, and Galactic Winds: Issues in Giant Galaxy Formation. *AJ*, 115:1801–1822, May 1998.

G. J. Hill and S. J. Lilly. A change in the cluster environments of radio galaxies with cosmic epoch. *ApJ*, 367:1–18, January 1991.

G. J. Hill, S. J. Lilly, and M. A. Rigler. Further Evidence for a Change in the Cluster Environments of Radio Galaxies with Cosmic Epoch. In *ASP Conf. Ser. 51: Observational Cosmology*, pages 262+, 1993.

C. R. Kaiser and P. Alexander. Heating of the intergalactic medium by FR II radio sources. *MNRAS*, 305:707–723, May 1999.

U. Klein. The Large-Scale Structure of Virgo A. In *The radio galaxy Messier 87 : proceedings of a workshop held at Ringberg Castle, Tegernsee, Germany, 15-19 September 1997 / Hermann-Josef Röser, Klaus Meisenheimer, eds. Berlin ; New York : Springer, 1999. (Lecture notes in physics, 530, ISSN0075-8450).*, 1999.

S. S. Komissarov. Numerical simulations of relativistic magnetized jets. *MNRAS*, 308:1069–1076, October 1999.

D. Kössl and E. Müller. Numerical simulations of astrophysical jets - The influence of boundary conditions and grid resolution. *A&A*, 206:204–218, November 1988.

D. Kössl, E. Müller, and W. Hillebrandt. Numerical simulations of axially symmetric magnetized jets. I - The influence of equipartition magnetic fields. *A&A*, 229:378–415, March 1990a.

D. Kössl, E. Müller, and W. Hillebrandt. Numerical Simulations of Axially Symmetric Magnetized Jets. III - Collimation of Underexpanded Jets by Magnetic Fields. *A&A*, 229:401+, March 1990b.

T. P. Krichbaum, W. Alef, A. Witzel, J. A. Zensus, R. S. Booth, A. Greve, and A. E. E. Rogers. VLBI observations of CygnusA with sub-milliarcsecond resolution. *A&A*, 329:873–894, January 1998.

J. D. Kurk, L. Pentericci, H. J. A. Röttgering, and G. K. Miley. A protocluster around a radio galaxy at redshift 2.16. *Astrophysics and Space Science Supplement*, 277:543–546, 2001a.

J. D. Kurk, H. J. A. Rottgering, L. Pentericci, and G. K. Miley. Observations of radio galaxy MRC 1138-262: a giant halo of Lya en Ha emitting ionized gas. In *Emission Lines from Jet Flows. Isla Mujeres November 13- 17, 2000*, November 2000.

J. D. Kurk, B. P. Venemans, H. J. A. Roettgering, G. K. Miley, and L. Pentericci. A search for high redshift clusters associated with radio galaxies at $2 < z < 4$. In *Sesto conference proceeding 'Probing cosmic evolution with galaxy clusters'*, page ?, October 2001b.

M. Lacy, G. Miley, S. Rawlings, R. Saunders, M. Dickinson, S. Garrington, S. Maddox, G. Pooley, C. Steidel, M. N. Bremer, G. Cotter, R. van Ojik, H. Röttgering, and P. Warner. 8C 1435+635: a radio galaxy at z=4.25. *MNRAS*, 271:504–512, November 1994.

J. P. Leahy. DRAGNs. In *Jets in Extragalactic Radio Sources, Proceedings of a Workshop Held at Ringberg Castle, Tegernsee, FRG, September 22-28, 1991. Edited by H.-J. R&oouml;ser and K. Meisenheimer. Springer-Verlag Berlin Heidelberg New York. Also Lecture Notes in Physics, volume 421, 1993, p.1*, pages 1+, 1993.

J. P. Leahy. DRAGN Atlas. In *http://www.jb.man.ac.uk/atlas/*, 2000.

H. Lesch and G. T. Birk. On the Origin of Extended Nonthermal Optical Emission in Extragalactic Jets. *ApJ*, 499:167+, May 1998.

S. J. Lilly. Discovery of a radio galaxy at a redshift of 3.395. *ApJ*, 333:161–167, October 1988.

K. R. Lind. Observations and gas dynamics of extragalactic radio jets. *Ph.D. Thesis*, 1987.

K. R. Lind, D. G. Payne, D. L. Meier, and R. D. Blandford. Numerical simulations of magnetized jets. *ApJ*, 344:89–103, September 1989.

C. Loken, J. O. Burns, D. A. Clarke, and M. L. Norman. Ram-pressure confinement of a hypersonic jet. *ApJ*, 392:54–64, June 1992.

H. L. Marshall, B. P. Miller, D. S. Davis, E. S. Perlman, M. Wise, C. R. Canizares, and D. E. Harris. A High-Resolution X-Ray Image of the Jet in M87. *ApJ*, 564:683–687, January 2002.

S. Massaglia, G. Bodo, and A. Ferrari. Dynamical and radiative properties of astrophysical supersonic jets. I. Cocoon morphologies. *A&A*, 307:997–1008, March 1996.

P. J. McCarthy. High redshift radio galaxies. *A&AReview*, 31:639–688, 1993.

R. J. McLure and J. S. Dunlop. The cluster environments of powerful radio-loud and radio-quiet active galactic nuclei. *MNRAS*, 321:515–524, March 2001.

K. Meisenheimer. Particle Acceleration in Extended Radio Sources - a Critical Review. In *Jets from Stars and Galactic Nuclei*, pages 57+, 1996.

K. Meisenheimer and H. Hippelein. The emission-line lobes of 3C 368. *A&A*, 264:455–471, October 1992.

M. Micono, G. Bodo, S. Massaglia, P. Rossi, A. Ferrari, and R. Rosner. Kelvin-Helmholtz instability in three dimensional radiative jets. *A&A*, 360:795–808, August 2000.

R. Minkowski. A New Distant Cluster of Galaxies. *ApJ*, 132:908–910, November 1960.

K. Nishikawa, S. Koide, J. Sakai, D. M. Christodoulou, H. Sol, and R. L. Mutel. Three-Dimensional Magnetohydrodynamic Simulations of Relativistic Jets Injected along a Magnetic Field. *ApJ Letter*, 483:L45–+, July 1997.

K. Nishikawa, S. Koide, J. Sakai, D. M. Christodoulou, H. Sol, and R. L. Mutel. Three-dimensional Magnetohydrodynamic Simulations of Relativistic Jets Injected into an Oblique Magnetic Field. *ApJ*, 498:166+, May 1998.

M. L. Norman and D. S. Balsara. 3-D Hydrodynamical Simulations of Extragalactic Jets. In *Jets in Extragalactic Radio Sources, Proceedings of a Workshop Held at Ringberg Castle, Tegernsee, FRG, September 22-28, 1991. Edited by H.-J. R&oouml;ser and K. Meisenheimer. Springer-Verlag Berlin Heidelberg New York. Also Lecture Notes in Physics, volume 421, 1993, p.229*, pages 229+, 1993.

M. L. Norman, K. H. A. Winkler, and L. Smarr. Propagation and morphology of pressure-confined supersonic jets. In *Astrophysical jets; Proceedings of the International Workshop, Turin, Italy, October 7-9, 1982 (A84-22076 08-90). Dordrecht, D. Reidel Publishing Co., 1983, p. 227-250; Discussion, p. 251.*, pages 227–250, 1983.

M. L. Norman, K.-H. A. Winkler, L. Smarr, and M. D. Smith. Structure and dynamics of supersonic jets. *A&A*, 113:285–302, September 1982.

Michael L. Norman. Numerical Simulations of Astrophysical Jets. In *Space Telescope Science Institute Symposium Series, Proceedings of the Astrophysical Jets Meeting, held in Baltimore 1992 May 12-14, Cambridge, UK: Cambridge University Press, —c1993, edited by Burgarella, Denis; Livio, Mario; O'Dea, Christopher P.*, 1993.

F. Owen. The Structure of the Radio Halo. In *The radio galaxy Messier 87 : proceedings of a workshop held at Ringberg Castle, Tegernsee, Germany, 15-19 September 1997 / Hermann-Josef Röser, Klaus Meisenheimer, eds. Berlin ; New York : Springer, 1999. (Lecture notes in physics, 530, ISSN0075-8450)., p.72*, pages 72+, 1999.

F. N. Owen and R. A. White. Surface photometry of radio galaxies. II - Cluster sources. *MNRAS*, 249:164–171, March 1991.

P. Papadopoulos, R. Ivison, C. Carilli, and G. Lewis. A massive reservoir of low-excitation molecular gas at high redshift. *Nature*, 409:58–60, January 2001.

P. Parma, M. Murgia, R. Morganti, A. Capetti, H. R. de Ruiter, and R. Fanti. Radiative ages in a representative sample of low luminosity radio galaxies. *A&A*, 344:7–16, April 1999.

L. Pentericci, J. D. Kurk, H. J. A. Röttgering, G. K. Miley, W. van Breugel, C. L. Carilli, H. Ford, T. Heckman, P. McCarthy, and A. Moorwood. A search for clusters at high redshift. II. A proto cluster around a radio galaxy at z=2.16. *A&A*, 361:L25–L28, September 2000.

L. Pentericci, P. J. McCarthy, H. J. A. Röttgering, G. K. Miley, W. J. M. van Breugel, and R. Fosbury. NICMOS Observations of High-Redshift Radio Galaxies: Witnessing the Formation of Bright Elliptical Galaxies? *ApJ Supplement*, 135:63–85, July 2001.

L. Pentericci, H. J. A. Roettgering, G. K. Miley, C. L. Carilli, and P. McCarthy. The radio galaxy 1138-262 at z=2.2: a giant elliptical galaxy at the center of a proto-cluster? *A&A*, 326:580–596, October 1997.

L. Pentericci, H. J. A. Roettgering, G. K. Miley, H. Spinrad, P. J. McCarthy, W. J. M. van Breugel, and F. Macchetto. HST Images of the Extremely Clumpy Radio Galaxy 1138-262 at Z =2.2. *ApJ*, 504:139+, September 1998.

E. R. Priest. Magnetohydrodynamics (With 87 figures). In *Saas-Fee Advanced Course 24: Plasma Astrophysics*, pages 1+, 1994.

D. R. Rayburn. A numerical study of the continuous beam model of extragalactic radio sources. *MNRAS*, 179:603–617, June 1977.

A. Rosen, P. E. Hardee, D. A. Clarke, and A. Johnson. Effects of Magnetic Fields on Mass Entrainment of Supermagnetosonic Jets. *ApJ*, 510:136–154, January 1999.

H. Röttgering, G. Miley, and R. van Ojik. Giant gas halos in radio galaxies: a unique probe of the early universe. *The Messenger*, 83:26–29, 1996.

L. Scheck, M. A. Aloy, J. M. Marti, J. L. Gomez, and E. Mueller. Does the plasma composition affect the long term evolution of relativistic jets? *MNRAS*, 2002.

P. A. G. Scheuer. Lobe Asymmetry and the Expansion Speeds of Radio Sources. *MNRAS*, 277:331+, November 1995.

M. J. Seaton. Radiative recombination of hydrogenic ions. *MNRAS*, 119:81+, 1959.

L. I. Sedov. *Similarity and Dimensional Methods in Mechanics*. Similarity and Dimensional Methods in Mechanics, New York: Academic Press, 1959, 1959.

D. A. Smith, A. S. Wilson, K. A. Arnaud, Y. Terashima, and A. J. Young. A Chandra X-ray Study of Cygnus A – III. The Cluster of Galaxies. *ApJ*, 565, January 2002.

C. Solórzano-Iñarrea, C. N. Tadhunter, and D. J. Axon. The evidence for jet-cloud interactions in a sample of high-redshift radio galaxies. *MNRAS*, 323: 965–987, May 2001.

H. Spinrad, J. Stauffer, and H. Butcher. Spectroscopy and photometry of 3C 427.1 and 3C 13 - Distant radio galaxies with Z greater than 1.0. *ApJ*, 244: 382–387, March 1981.

W. Steffen, J. L. Gomez, R. J. R. Williams, A. C. Raga, and A. Pedlar. Jet cocoons and the formation of narrow-line clouds in Seyfert galaxies. *MNRAS*, 286:1032–1040, April 1997.

J. M. Stone and M. L. Norman. ZEUS-2D: A radiation magnetohydrodynamics code for astrophysical flows in two space dimensions. I - The hydrodynamic algorithms and tests. *ApJ Supplement*, 80:753–790, June 1992a.

J. M. Stone and M. L. Norman. ZEUS-2D: A Radiation Magnetohydrodynamics Code for Astrophysical Flows in Two Space Dimensions. II. The Magnetohydrodynamic Algorithms and Tests. *ApJ Supplement*, 80:791+, June 1992b.

J. M. Stone and M. L. Norman. Numerical simulations of protostellar jets with nonequilibrium cooling. I - Method and two-dimensional results. *ApJ*, 413: 198–220, August 1993.

R. S. Sutherland, G. V. Bicknell, and M. A. Dopita. Shock excitation of the emission-line filaments in Centaurus A. *ApJ*, 414:510–526, September 1993.

R. S. Sutherland and M. A. Dopita. Cooling functions for low-density astrophysical plasmas. *ApJ Supplement*, 88:253–327, September 1993.

M. Thiele. Numerische Simulationen protostellarer Jets. *Ph.D. Thesis*, 2000.

I. L. Tregillis, T. W. Jones, and D. Ryu. Simulating Electron Transport and Synchrotron Emission in Radio Galaxies: Shock Acceleration and Synchrotron Aging in Three-dimensional Flows. *ApJ*, 557:475–491, August 2001.

W. van Breugel, C. De Breuck, S. A. Stanford, D. Stern, H. Röttgering, and G. Miley. A Radio Galaxy at Z = 5.19. *ApJ*, 518:L61–L64, June 1999.

R. van Ojik, H. J. A. Röttgering, C. L. Carilli, G. K. Miley, M. N. Bremer, and F. Macchetto. A powerful radio galaxy at z=3.6 in a giant rotating Lyman α halo. *A&A*, 313:25–44, September 1996.

R. van Ojik, H. J. A. Röttgering, G. K. Miley, and R. W. Hunstead. The gaseous environments of radio galaxies in the early Universe: kinematics of the Lyman α emission and spatially resolved H I absorption. *A&A*, 317: 358–384, January 1997.

D. A. Verner and G. J. Ferland. Atomic Data for Astrophysics. I. Radiative Recombination Rates for H-like, He-like, Li-like, and Na-like Ions over a Broad Range of Temperature. *ApJ Supplement*, 103:467+, April 1996.

M. Villar-Martín, D. De Young, A. Alonso-Herrero, M. Allen, and L. Binette. Shocks and dust survival in nearby active galaxies: implications for the alignment effect. *MNRAS*, 328:848–854, December 2001.

M. Villar-Martín, R. Fosbury, J. Vernet, M. Cohen, A. Cimatti, and S. di Serego Alighieri. Gas metallicities and early evolution of distant radio galaxies. *Astrophysics and Space Science*, 277:571–574, 2001.

M. Villar-Martín, C. Tadhunter, R. Morganti, D. Axon, and A. Koekemoer. PKS 2250-41 and the role of jet-cloud interactions in powerful radio galaxies. *MNRAS*, 307:24–40, July 1999.

R. Wünsch and J. Palouš. Gravitational instability of expanding shells. Solution with nonlinear terms. *A&A*, 374:746–755, August 2001.

A. G. Williams and S. F. Gull. Multiple hotspots in extragalactic radio sources. *Nature*, 313:34–36, January 1985.

P. Woodward and P. Colella. . *Journal of Computational Physics*, 54:115, 1984.

A. J. Young, A. S. Wilson, and C. G. Mundell. Chandra Imaging of the X-ray Core of the Virgo Cluster. *to appear in ApJ*, 2002.

U. Ziegler and H. W. Yorke. A nested grid refinement technique for magnetohydrodynamical flows. *Computer Physics Communications*, 101:54, 1997.

Acknowledgements

This work was generously supported by many people. I acknowledge the support of the Deutsche Forschungsgemeinschaft (Sonderforschungsbereich 437), and the Höchstleistungsrechenzentrum (Stuttgart). I am thankful for the valuable scientific advice and help in various aspects of my Doktorvater Max Camenzind, e.g. support in hardware troubles, manuscript reading, inspiring discussions, ... I thank Klaus Meisenheimer for initiating this project together with Max Camenzind and his continued interest. The theory group at the Landessternwarte Heidelberg was always a nice working place. Thanks to all of you! Special thanks goes to my room-mate José Gracia, for patiently listening to the wonders of science ("Did you know that Latex allows only four lines for titles? Can you imagine that the printer does completely different things than it should do?") Furthermore, his computer skills were essential to keep the machines running. I appreciate computer support from Monika Darr and especially Otmar Stahl, who reset the printer with a smile, each time. I am grateful for the support of my parents, my wife, and Jesus.